THE MASSES OF THE W AND Z BOSONS AND A SEARCH FOR THEIR SUPERSYMMETRIC LEPTONIC DECAYS AT THE CERN COLLIDER

Stephen James Haywood

Thesis submitted for the degree of Doctor of Philosophy.

Department of Physics,
Faculty of Science,
The University of Birmingham.

November 1987

Synopsis

The UA1 Experiment at the CERN $p\bar{p}$ Collider has identified 67 candidates for the decay $W \to \mu\nu$ and 21 candidates for the decay $Z \to \mu\mu$. In this thesis we use a subset of these events to determine the masses of the W and Z bosons. Methods to improve the momentum estimates of fast muons are also discussed. We find

$$m_W = 81.8 \; +6.0, -5.3(\text{stat}) \pm 2.6(\text{syst}) \; \text{GeV}/c^2$$

and

$$m_Z = 90.7 \; +5.2, -4.8(\text{stat}) \pm 3.2(\text{syst}) \; \text{GeV}/c^2.$$

The measurements are in good agreement with results from the UA1 and UA2 electron analyses.

Supersymmetry is a theory which may explain some of the puzzles of the Standard Model. If the theory is valid, then we might expect to see the supersymmetric partners of the leptons. We have used UA1 data to search for the supersymmetric decays of the W and Z bosons. In the absence of any clear signal, we have used the agreement between our data and the Standard Model expectations to set limits on the masses of the supersymmetric electron ($\tilde{e}$) and neutrino ($\tilde{\nu}$). For degenerate supersymmetric partners of the left handed electron and neutrino, we find

$$m(\tilde{e_L}) > 32 \; \text{GeV}/c^2 \text{ at } 90\% \text{ confidence, if } m(\tilde{e_L}) = m(\tilde{\nu}).$$

Acknowledgements

I would like to thank the SERC and the tax-payers of the UK for the substantial support which I have received as a postgraduate student. Also, I would like to thank the University of Birmingham and in particular the Department of Physics for support. I am indebted to Professors Derek Colley and John Dowell for their encouragement over the last three years and for giving me the opportunity to spend a considerable period of time at CERN. Thanks to Glenn Cox for directing me while I was at Birmingham. I am very grateful to my supervisor, Martyn Corden, who has been a friend rather than a task master. I greatly appreciate the way Martyn has been prepared to drop everything to lend his considerable expertise to solve my 'impossible' problems, with enthusiasm and selflessness. Martyn and Glenn had the dubious privilege of struggling through this thesis to check it. My thanks to John Wilson and Roger Cashmore for taking the time to examine this work.

Most of my activity in UA1, at least in the beginning, involved muons, and I am very grateful to all my German colleagues for letting me work with them, and for the friendship which they showed me. Much of my time in UA1 was spent working with the W/Z group. I am greatly indebted to Steve Wimpenny for his endless encouragement, friendship and confidence in my work. Without Steve, I would not have been able to do much of the work presented here. It was a lot of fun to work with Evelin Tscheslog and Reinhard Leuchs on the muon analysis, and I would like to thank them for their collaboration. I am very grateful to Elizabeth Locci and Marie-Noelle Minard for helping me to get into the electron analysis and for doing all the nitty-gritty. Thanks to Daniel Denegri, Steve Geer and Felicitas Pauss for many discussions on W/Z physics. I enjoyed working with Joe Kroll, Alan Norton and Ken Long on the CD, and would like to thank Veikko Karimaki and Martti Pimia for answering all my CD questions. I also enjoyed OMFing with Glenn and Martyn. Throughout my UA1 work, I have appreciated the support and collaboration of Alan Norton and Michel Della Negra. I would like to thank the Top group for the effort which they invested in the Monte-Carlo production - despite my criticism at the time. Thanks to John Ellis and Howie Baer for answering my SUSY questions. I am very grateful to Fred James for his statistical advice and to Ashot Chillingarian for introducing me to new concepts.

I owe many thanks to Robert Edgecock for more loyal friendship than I deserve. Without Rob, the last three years would have been miserable. Many thanks to David Charlton who gave me a title for the last chapter, showed me what a computer is, told me all I wanted to know about the Top analysis, and taught me how to use my brain. Thanks to Jonathan Gregory for his love and for trying to teach me the basics of the English language. Jonathan attempted to remove all my mistakes in the final draft. I am grateful to Mike Albrow, Nick Ellis and Pete Watkins for their help while I have been in UA1. Thanks to Bob van Eijk for help with some of the detector pictures. I enjoyed the company of many people in the last three years, in particularly Nav, Mary, Martin, Jon and Roberto. This is a suitable place to thank Mike Bowler and Michael Baker for teaching me lots of physics at Merton.

Many thanks to the members of the Thursday Group for their fellowship and the chance to learn more of the love of Christ. Thanks to Mary-Elizabeth and Sue for 'mothering' me while I was in Geneva. In Birmingham, the McKerracher Clan had the misfortune to have to put up with me. Thanks to David, Doreen, Fiona and Alison for their friendship.

So far I have only thanked people who have had a direct influence on this work. However, work is just one part of life, and I would like to thank all my family and friends who have supported me in the last twenty five years. In particular, I would like to thank Doris and Brian for the part they have played in my life. Finally, my thanks to Mum, Dad and Alan - without their endless love and unquestioning support, I could not have even started this work. This thesis is as much their work as it is mine.

To all of you, thank you.

Stephen - Geneva 1987.

CONTENTS

1. INTRODUCTION

1.1 A Historical Overview

Ever since the discovery of radioactivity by Becquerel in 1896 and the subsequent identification of β rays, physicists have struggled to understand the nature of the weak interaction. However, a complete understanding was not achieved until the 1960's when the work of Glashow [1], Salam [2] and Weinberg [3] (GSW) pointed to a credible theory of the electroweak interaction. This theory, in conjunction with QCD, forms the crux of the Standard Model, which provides an excellent description of the laws of nature, excluding gravitational phenomena. Central to the theory of GSW were the predictions of unobserved particles: W^+, W^- and Z^0 (the intermediate vector bosons, or IVB's) with masses greater than 40, 40 and 80 GeV/c^2 respectively [3].

To observe these new particles demanded energies in excess of those available in the late 1960's. In 1976, Rubbia, McIntyre and Cline [4] proposed a scheme to increase the energy of the CERN Super Proton Synchrotron (SPS) by converting it to a colliding beam machine. In 1978, a proposal [5] for an experiment (to be called UA1) to detect the W and Z bosons was submitted. The following year, Glashow, Salam and Weinberg received the Nobel Prize for Physics. UA1 came into operation in 1981, and the W was discovered in 1982, with the Z in the following year. Finally, in 1984, the Nobel Prize was awarded jointly to Carlo Rubbia for his tremendous role in the discoveries, and to Simon van der Meer for his pioneering work on stochastic cooling.

1.2 The Collider Project

To produce very massive particles requires high centre of mass energies ($\sqrt{s}$) for collisions. When a particle of energy E collides with a stationary particle of mass m (typically about 1 GeV/c^2), the energy available to form new particles is

$$\sqrt{s} \approx \sqrt{(2mc^2E)} \propto \sqrt{E} \qquad (1.1)$$

To be able to reach the energies required for the production of the W and Z bosons (whose masses, at the time of the UA1 proposal, were estimated as 60 to 80 GeV/c^2), necessitated a beam energy which was unobtainable in the 1970's. The alternative was to collide one beam of particles with a second beam with the opposite momentum. In this way, the available energy becomes

$$\sqrt{s} = 2E \tag{1.2}$$

It was anticipated that the W could be produced in proton-antiproton collisions, the creation mechanism proceeding via the interaction of the point-like constituents, namely the quarks. However, since the quarks carry only a fraction of the proton momentum (typically about $^1/_6$), the energy of the beams needs to be several hundred GeV. The proposal of Rubbia et al to utilise the SPS at CERN made use of an existing facility, and by using a counter-rotating beam of antiprotons, it was not necessary to install a new ring for the second beam. What was lacking was a source of large numbers of antiprotons - this is discussed in more detail in the following chapter. Although the SPS routinely operated at beam energies of 450 GeV, it was possible to attain beam energies of only 273 GeV at the initial operation, due to the problems of cooling the magnets during the continuous acceleration. With improvements, this was raised to 315 GeV in 1984.

1.3 The UA1 Experiment

The aim of UA1 was to search for the W and Z bosons. The first evidence for W production and subsequent decay came from the observation of high transverse[1] momentum electrons accompanied by 'missing transverse energy' [6]. This 'missing energy' corresponds to a neutrino, which cannot be detected directly, recoiling against the electron. The Z was identified by its decay to pairs of energetic high p_t electrons [7]. Subsequently, the muonic decay modes were also observed [8], [7]. The total numbers of candidates to date are shown in table 1.

---

[1] perpendicular to the colliding beams

Table 1: Current Numbers of W/Z Candidates

	W	Z
electron	290	35
muon	67	21

As well as discovering the W and the Z, the UA1 Collaboration has contributed substantially to particle physics by exploring a new energy range. Significant work has been done on:

- B-physics: associated with the b quark. In 1986, UA1 reported the first observation of B^0-$\overline{B}^0$ oscillations [9].
- Jet physics: for the first time, jets were unambiguously seen in the collisions of hadrons [10], and extensive tests have been made of QCD.
- Missing Energy: in addition to significant missing energy arising from decays of W's to electrons and muons, the decays into tau leptons have also been seen. Further, the agreement between the data and the theoretical predictions for known contributions has enabled limits to be placed on other sources of missing energy, namely the production of heavy leptons or supersymmetric particles (see chapter 8).
- Top Quark: while it is expected that there should be a sixth quark, there is yet no evidence for it at present, and UA1 has set limits on its mass (see chapter 9).

1.4 The Layout of This Thesis

The contents of this thesis are in three parts:

1. Introductory Material,
2. Estimates of the W and Z Masses from the Muon Channel,
3. A Search for the Supersymmetric Decays of the W and Z Bosons.

1) After a description of the UA1 detector (chapter 2), methods for improving the momentum estimates of fast muons are described (chapter 3). The first of these relies on a more elaborate version of the standard track reconstruction. The second combines information from the muon chambers and central detector in an overall momentum fit (OMF). These procedures are applied to the W and Z candidates. In chapter 4, likelihood methods for statistical analysis are discussed and some of the relevant proofs are given. Heavy use is made of these methods in the subsequent analysis, and an understanding of the statistical methods used is essential to the interpretation of the results derived.

2) The theoretical ideas underlying the electroweak theory of Glashow, Weinberg and Salam are presented in chapter 5. Some of the more important phenomenological consequences for the W and Z are also examined. In chapters 6 and 7, the standard selection of the W and Z candidates in the muon channel is described. Using these events, the masses of the bosons are deduced and the parameters of the Standard Model are derived.

3) In chapter 8, the motivation for 'new physics' beyond the Standard Model is given. The phenomenology of one such model, Supersymmetry, is explained. In chapter 9, we discuss a search that has been made for the supersymmetric decays of the W and Z, and the limits derived for these processes.

Throughout, substantial use is made of the ISAJET Monte-Carlo computer program of Paige and Protopopescu [11]. This has been used consistently by the UA1 collaboration and is found to provide a good description of the physics at the collider [55]. Frequently, reference will be made to 'ISAJET', where the implications are that the events produced by the Monte-Carlo are subjected to a software simulation of the UA1 detector. Further comments are made in appendix F.

The units used in this thesis for energies, momenta and masses are GeV, GeV/c and GeV/c^2 respectively. This will be assumed, unless stated otherwise.

The Author's Contribution.

I was responsible for devising the cosmic ray tests of OMF. After the successful operation of the Iarocci chambers in 1985, I incorporated them into the OMF procedure.

I helped with the final stages of the data selection and processing for the muonic W and Z candidates in 1986. After both the 1984 and 1985 runs, I was responsible for the mass estimates of the IVB's. In 1986, I spent considerable effort trying to improve the muon momentum estimates using the methods of chapter 3.

In 1986-87, I tried independently to extend the previous analysis of UA1 in looking for supersymmetric decays. Initially, I invested a lot of time setting up a simple Monte-Carlo description of some of the SUSY processes which might be seen in the UA1 detector. This provided motivation for how to perform the search and what could be obtained. In the W channels, the standard selections were adequate; but for the Z channels, I selected data from available preselections, using looser cuts. As a cross-check, I tried to put the appropriate supersymmetric decays into the ISAJET Monte-Carlo. I went to great pains to try to understand how to perform the statistical analysis; and since no signal was apparent, I spent a lot of time trying to devise efficient and effective prescriptions for deriving confidence limits.

2. THE UA1 EXPERIMENT

The first section of this chapter contains a brief outline of the accelerators vital for creating the $p\bar{p}$ collisions. This includes details on the accumulation of the $\bar{p}$'s. The rest of the chapter is devoted to a fairly detailed discussion of the UA1 detector.

2.1 The Accelerators

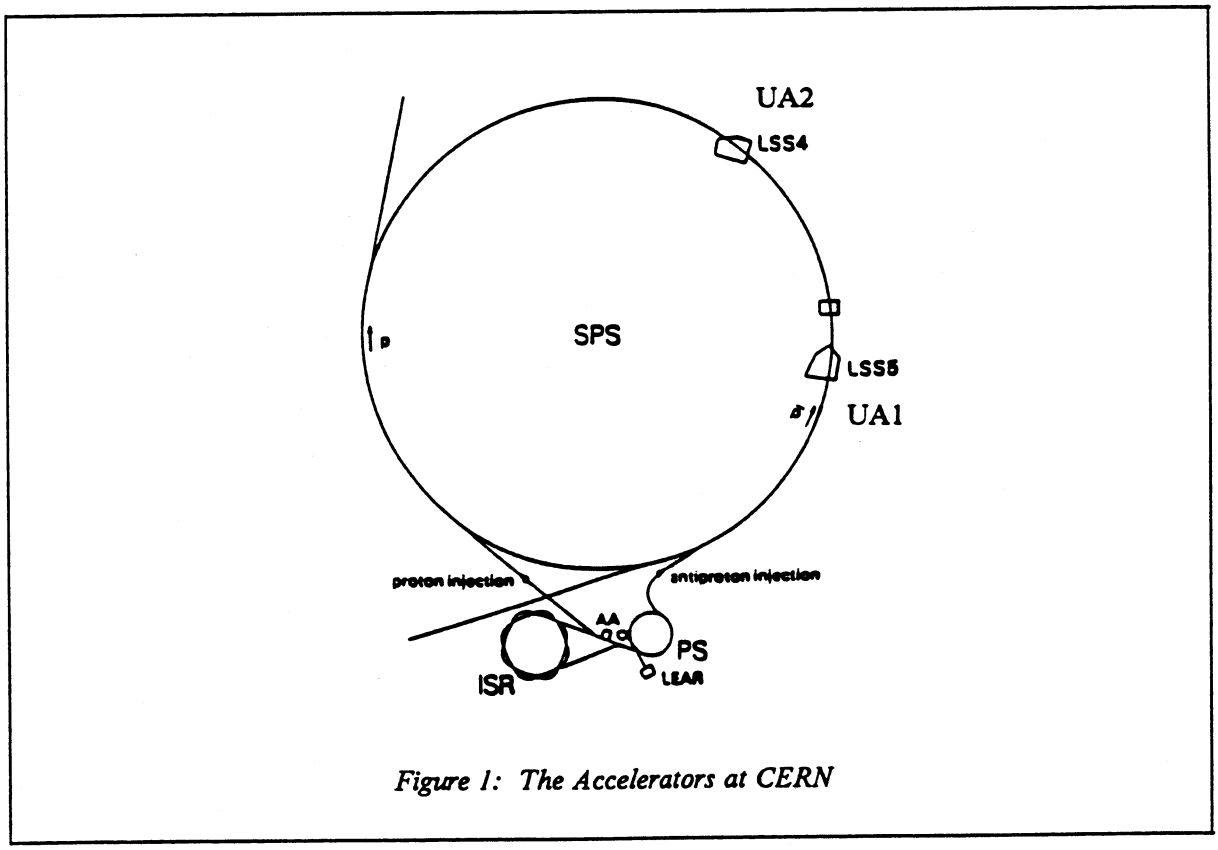

Figure 1: The Accelerators at CERN

The layout of the CERN accelerators [12] is shown in figure 1. Protons are obtained by ionising hydrogen gas with an electrical discharge. They then enter a linac, leaving at 50 MeV, and pass through a booster to enter the Proton Synchrotron (PS) at 800 MeV. Most of the 26 GeV protons leaving the PS are sent to the Antiproton Accumulator (AA) where they strike a copper target, forming

antiprotons. These antiprotons are collected and transferred to the storage ring, where they are kept until sufficient numbers have been collected. Roughly every 24 hours, antiprotons from the AA are returned to the PS, from which three bunches are injected into the SPS. The three bunches of protons are injected just beforehand. These are then ramped up to the maximum energy (273 or now 315 GeV) at which they are kept until the next refill. The bunches are arranged to intersect at the centre of UA1 to within ± 30 cm every 7.6 μs.

The rate at which interactions take place is measured by the luminosity, $\mathscr{L}$:

$$dN/dt = \mathscr{L}\sigma \tag{2.1}$$

where σ is the interaction cross-section for the process. In terms of the machine parameters (see table 2), the luminosity is given by:

$$\mathscr{L} = N_p N_{\bar{p}} f/A \tag{2.2}$$

where $N_{p,\bar{p}}$ are the number of protons,antiprotons per bunch; f is the bunch crossing frequency and A is the effective cross-sectional area of the two beams. This area is reduced in the neighbourhood of UA1 by quadrupole magnets. The beam lifetime is determined by the beam-beam interactions and the scattering of beam particles by gas molecules inside the beam pipe. The integrated luminosity collected by UA1 is shown in table 3.

Table 2: Approximate Values for the Parameters of the SPS

AA stacking rate	7×10^{9} $\bar{p}$ h^{-1}
Transfer efficiency	75 %
N_p	2×10^{11}
$N_{\bar{p}}$	2×10^{10}
Max initial $\mathscr{L}$	5×10^{29} $cm^{-2}s^{-1}$
Lifetime (Luminosity)	24 h
Gas pressure at UA1	10^{-8} Pa

Table 3: Integrated Luminosity Recorded at UA1

Period	Energy (GeV)	$\int \mathcal{L} dt$ (nb^{-1})
1981 Dec	546	0.023
1982 Oct/Dec	546	28
1983 Apr/Jul	546	136
1984 Sep/Dec	630	263
1985 Sep/Dec	630	305

2.1.1 The Accumulation of Antiprotons

The AA must perform two tasks: i) store $\bar{p}$'s and ii) reduce their phase space. The second point is important, since, according to Liouville's theorem, the phase space of a group of particles is conserved, so that as more $\bar{p}$'s are accumulated, so the phase space which they occupy grows. If this space is not reduced the AA would rapidly be filled up, and no more particles could be stored. Further, to attain reasonable luminosity, it is essential to make the bunches as dense as possible, while minimising the spread of the momenta of the particles within the bunch. So how can the AA violate Liouville's theorem? The theorem applies only to a continuum where separations of coordinates and their canonical momenta can be considered infinitesimal. For discrete particles it is possible to apply corrections with kicker magnets to small groups of $\bar{p}$'s in such a way as to reduce the overall phase space - a process known as stochastic cooling. The greater the density of particles, the closer continuity is approached and the slower the rate of cooling.

Every 2.6 seconds, 10^{13} protons from the PS strike a copper target. Magnetic lenses focus $\bar{p}$'s of around 3 to 5 GeV into the AA ring, which has a large acceptance (70 cm wide) - only about 5×10^6 $\bar{p}$'s are collected each time. These undergo precooling for 2.2 seconds, during which their momentum spread is reduced by a factor of 10 to about 0.1 %. Then these antiprotons are moved into the inner part of the ring where a 'stack' grows, separated from the precooling section by ferrite shutters. The stack is continuously compressed by the action of 100 kicker magnets controlled by 32 pick-ups. The pick-ups detect the bunch as it passes and transmit signals at the speed of light across the diameter of

the AA, so that the kickers can correct the bunch as it arrives. After 24 hours, the phase space of the particles has been reduced by a factor of 10^8, and a dense core has formed. From this, roughly 30% of the particles are extracted in three bunches of antiprotons. This operation is summarised in figure 2.

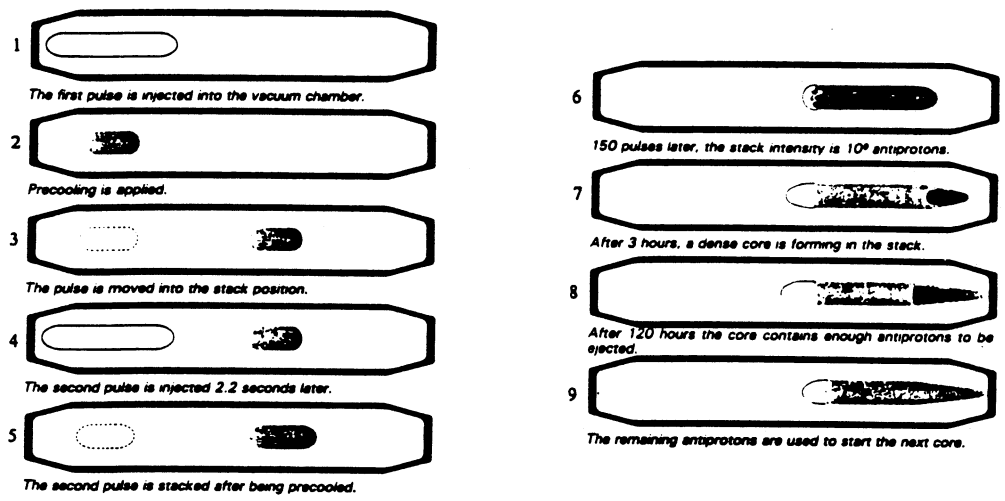

Figure 2: Operation of the Antiproton Accumulator

2.2 The UA1 Detector

The detector is shown in figure 3. The coordinates and angles used are defined in figure 4. The basic setup is a large central detector (CD) surrounded by calorimetry, with large chambers to detect muons outermost. For a general overview of the UA1 detector, the reader is referred to [13].

The CD provides tracking of charged particles and, from the bending caused by the strong magnetic field, measures particle momenta. The magnet produces a homogeneous field of 0.7 T over the central region covering, all of the CD. This field is dipolar and parallel to z (see the coordinates in figure 4). This allows particles from interactions which would otherwise travel down the beam pipe to be deflected into the forward chambers. Further, the dipolar field, in conjunction with the design of the CD, provides easy identification of high momentum particles emitted at low rapidity, without the

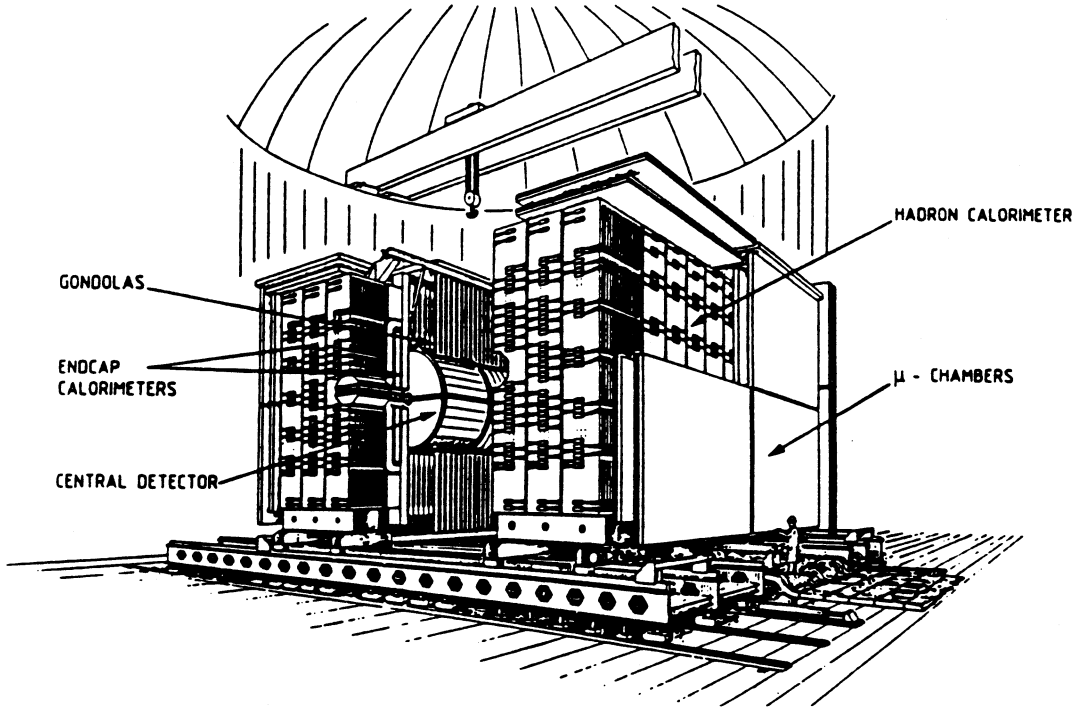

Figure 3: The UA1 Detector

confusion caused by low p_t particles at high rapidity. This situation is to be contrasted with the solenoidal geometry of some experiments.

The calorimeters are designed to absorb all the energy of charged and neutral particles, except for muons and neutrinos. There are two types: firstly the electromagnetic calorimeter, which absorbs electrons and photons; and secondly the hadron calorimeter, which absorbs the hadrons. In addition there is forward calorimetry covering down to an angle of 0.2° from the beam direction.

Surrounding the calorimeters is an iron shield to absorb any remnants of hadronic showers ('leakage') or particles which have failed to interact ('punch through'). This is instrumented by limited streamer tubes and outside these are the muon chambers - both being designed to detect muons.

The aim of the design is to achieve a 4π coverage of the solid angle surrounding the interaction region. This is important, so as to identify neutrinos in W decay, since they can only be inferred by the momentum imbalance in the whole event. This aim is largely achieved, although there are gaps in the calorimetry in the vertical $z = 0$ plane.

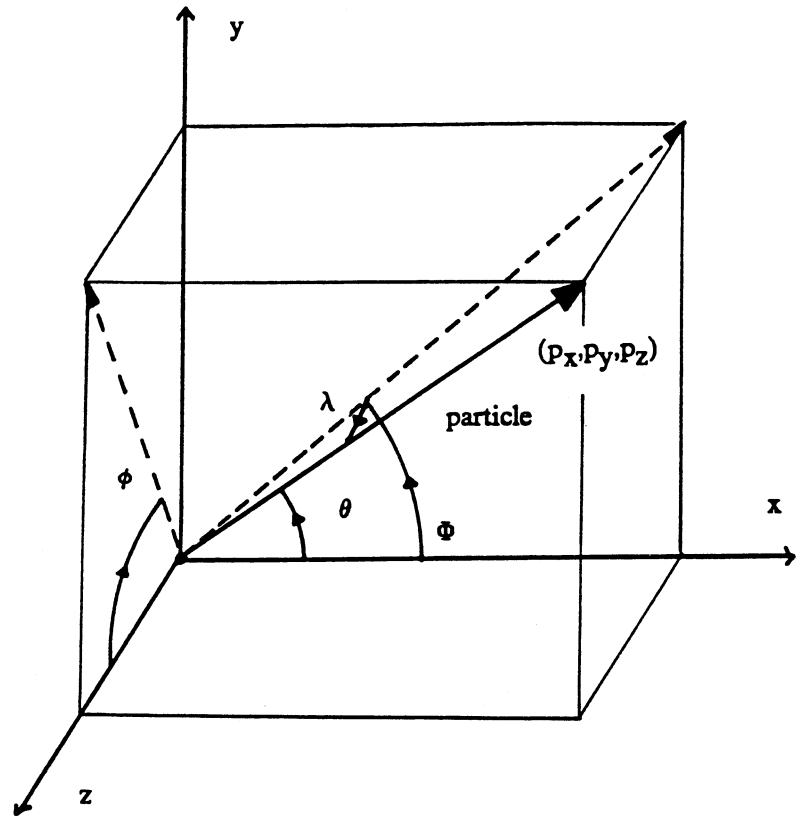

$$\tan\theta = \sqrt{(p_y^2+p_z^2)}/p_x, \qquad \tan\phi = p_y/p_z$$

$$\tan\lambda = p_z/\sqrt{(p_x^2+p_y^2)}, \qquad \tan\Phi = p_y/p_x$$

$$p_t = \sqrt{(p_y^2+p_z^2)}, \qquad \text{rapidity: } y = {}^1/_2\log[(E+p_x)/(E-p_x)]$$

$$\text{pseudorapidity: } \eta = -\log\tan(\theta/2)$$

Figure 4: Coordinate System used in UA1

2.2.1 The Central Detector

The CD [14] is a large cylindrical drift chamber (see figure 5), filled with a mixture of argon and ethane. It consists of alternating anode and cathode wire planes aligned parallel to the z direction. The sense wires in each anode plane are in two layers separated by field shaping wires - this avoids ambiguities in the drift direction (see figure 6). On passing through the CD, charged particles liberate

Table 4: The Magnet Parameters

Field strength	0.7 T
Total Current	2.0×10^6 ampere turns
Material	Aluminium
Thickness (absorption lengths)	$0.34\ \lambda_a$
Volume covered	$80\ m^3$
Power consumption	6 MW

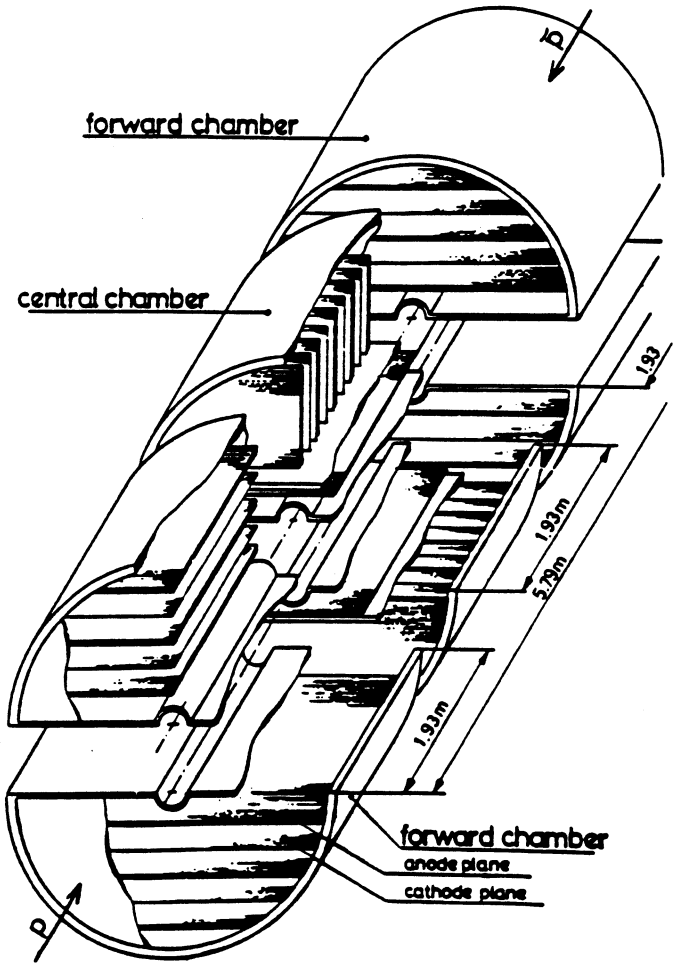

Figure 5: The Central Detector

electrons from the argon, which drift in the electric field towards the sense wires. Close to the wires,

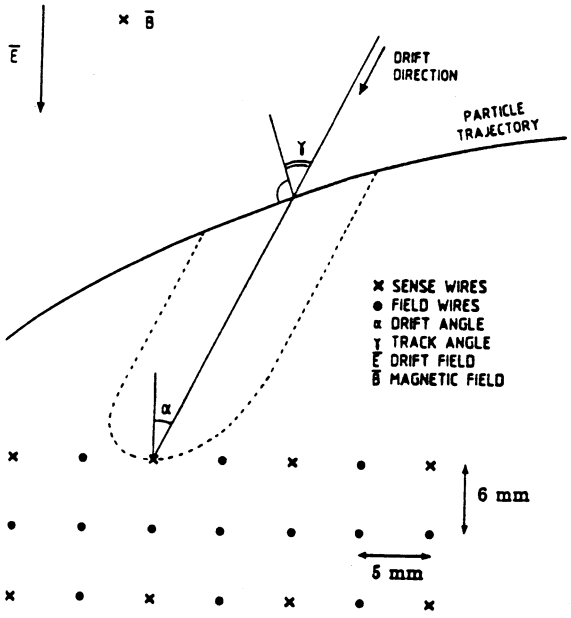

Figure 6: Details of Wire Planes in CD

the strong electric field creates an avalanche which provides a multiplication of the signal. For more details of the mechanisms, the reader is referred to [15]. The leading edges of pulses on the sense wires are measured to 4 ns, and the complete pulse is sampled every 32 ns by fast electronics. The maximum drift time is 3.6 μs, which is less than the originally proposed beam crossing period of 3.8 μs.

The wire planes are orientated to provide a large number of measured points ('digitisings') for all track directions (see figure 7). The $x-y$ coordinates are found by using the drift times measured for each sense wire. The z coordinates are found by charge division: the ratio of charges measured at each end of a sense wire gives the ratio of lengths along the wire. The latter measurement is not very precise and leads to considerable scatter (see figure 7). Energy loss (dE/dx) of particles, which can be used to identify slow particles, is measured by the total charge collected. Each channel produces a huge amount of data, and this condensed by the readout processors (ROP's). These processors reduce the 1.6 Mbytes of raw data to less than 0.1 Mbytes; providing the drift time, charge emerging from the left hand end of the sense wire and the total charge [16].

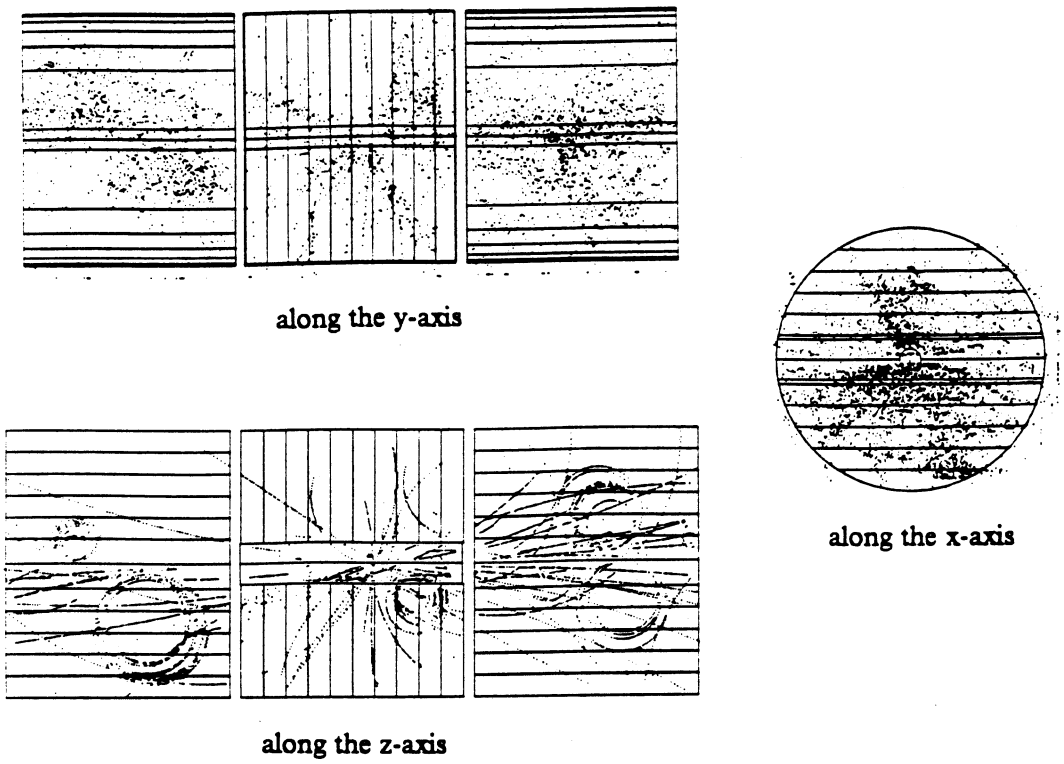

Figure 7: Digitisings in the UA1 Central Detector

The reconstruction of tracks is discussed in the following chapter. The momentum estimation is best for long forward tracks, while there is a vanishing acceptance for particles travelling parallel to the magnetic field. Calibration is performed with physics data and the alignment with cosmic rays.

Table 5: The CD Parameters

Length	6 m
Radius	0.1 m (inner), 1.2 m (outer)
Gas	40% argon + 60% ethane
Wire voltages	−27 kV (field), −1.5 or −2.5 kV (field), 0 kV (sense)
Separation	18 cm (plane), 1 cm (wire)
Drift velocity	5.3 cm/μs
Number of wires	6250 (sense), 23000 (total)
Spatial resolution	290 μm (x−y), 2 cm (z)
Momentum resolution $\delta(1/p)$ (typical)	0.01 to 0.02 (stat. + syst.)

2.2.2 The Electromagnetic Calorimeter

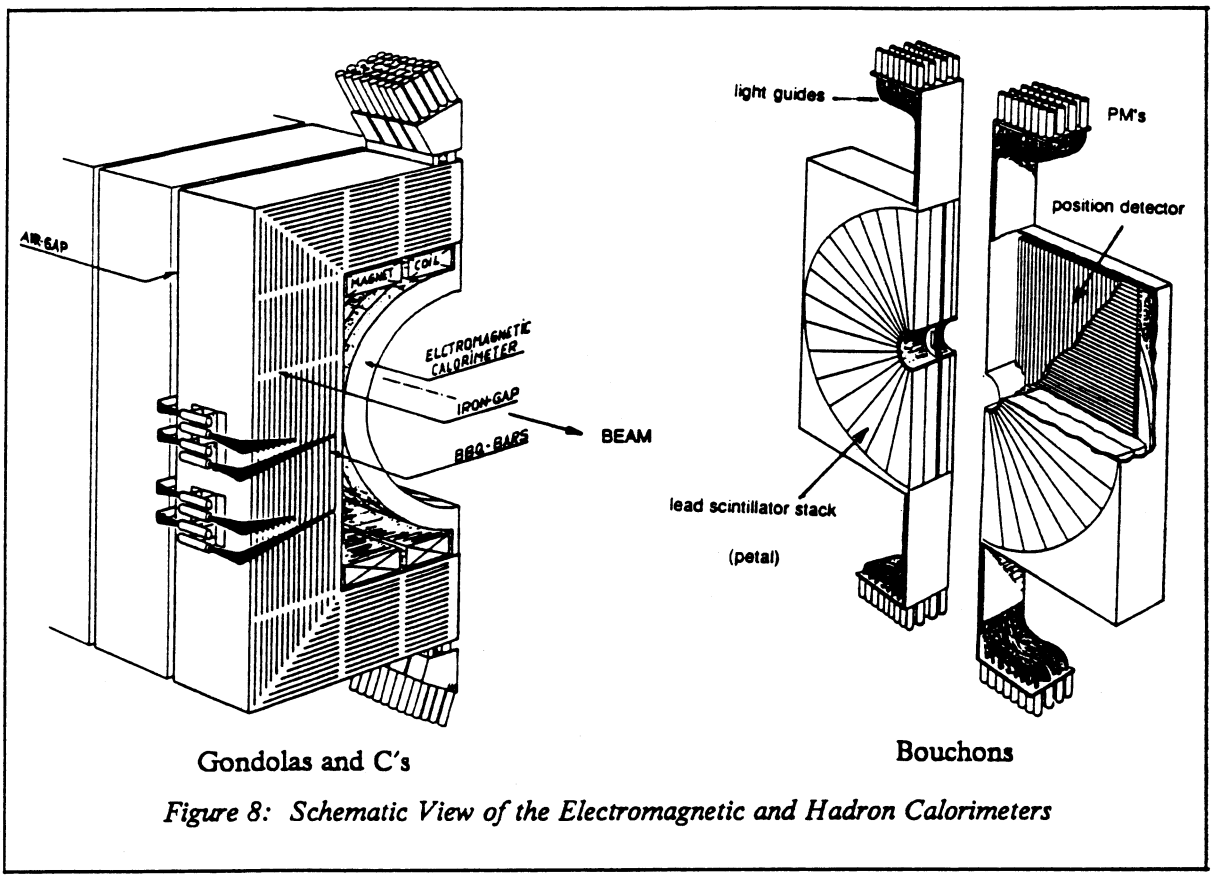

Figure 8: Schematic View of the Electromagnetic and Hadron Calorimeters

This is a sampling calorimeter [17], as is the hadron calorimeter (discussed in the next section). This implies that it consists of alternating layers of absorber and sensitive material. A good review of calorimeters can be found in reference [18]. The calorimeter is in two parts:

1. the Gondolas, which fit around the CD and inside the magnet coil, covering an angular range $25° < \theta < 155°$;
2. the Bouchons, which cover the ends of the CD, covering an angular range $5° < \theta < 25°$ and $155° < \theta < 175°$.

The Gondolas consist of 1.2 mm sheets of lead sandwiched between 1.5 mm sheets of plastic scintillator. These sheets are in the form of long strips, 22.5 cm wide and moulded to cover one side of

the CD (see figure 8). Electrons and photons, entering the calorimeter, readily shower in the lead, repeatedly dissipating energy by bremsstrahlung, pair production and annihilation. The shower excites the scintillator, which radiates in the UV. This light is transmitted through the plastic to wavelength shifting bars, doped with BBQ. The BBQ absorbs the ultraviolet light and isotropically reradiates green light, which is then carried by light guides to photomultipliers (PM's) situated outside the magnetic field.

The Gondolas are segmented in depth at 3.3, 6.6, 9.9, 6.6 radiation lengths,[2] each sampling containing many alternate layers of lead and scintillator. The total depth of 26 radiation lengths at normal incidence allows complete containment of EM showers. Each sampling is read out by four PM's, one at each of the four corners - two at the top, and two at the bottom. The shower profile in the four segments allows a distinction to be made between electrons (or photons) and other energetic particles. The total light collected is a measure of the energy deposited in that segment. The nominal energy resolution measured in a test beam is:

$$\Delta E = 0.15 \times \sqrt{E} \tag{2.3}$$

where the energy is measured in GeV. The $\sqrt{E}$ dependence is due to the statistical nature of shower production: the energy measured is roughly proportional to the number (N) of secondaries produced, and this will have an error like $\sqrt{N}$. Similarly, the number of photons emitted by the scintillator is also described by Poisson statistics. The light travelling to the PM's is attenuated within the plastic, so that by comparing the light collected by the PM's at the top with the light from those at the bottom, the azimuthal angle (ϕ) can measured, with a resolution:

$$\Delta\phi = 0.3 \div \sqrt{E} \text{ radians} \tag{2.4}$$

The Bouchons use the same principles as the Gondolas, but are designed differently. Each Bouchon comprises of 16 'petals' (see figure 8). They consist of 4 mm lead sheets alternating with 6 mm sheets of scintillator, with segmentation at 3.6, 7.2, 8.7, 7.2 radiation lengths. Each sampling is read out by a single PM at the outer edge. To help localise showers, there is a position detector

---

[2] 1 radiation length (X_0) is the distance over which the energy of an electron falls by a factor e. In lead, this is about 0.5 cm.

consisting of proportional tubes. This is located between the second and third samplings. The nominal energy resolution is:

$$\Delta E = 0.12 \times \sqrt{E} \tag{2.5}$$

with a spatial resolution of 2 mm.

The calorimeter is calibrated by lasers and cosmic rays while the experiment is running, and a ^{60}Co source otherwise. In recent years, it has been found that the scintillator has 'aged' due to radiation damage. This has reduced the photon yield from the scintillator and introduced uncertainties in the calibration. Further, the energy resolution has deteriorated, and in 1985 is found to be more like $0.23 \times \sqrt{E}$.

2.2.3 The Hadron Calorimeter

Like the electromagnetic calorimeter, this comes in two parts: the C's in the central region and the I's in the forward region (see figure 8) [19]. Hadrons lose their energy by quite different mechanisms, namely the creations of mesons and the breakup of nuclei. The absorption length[3] is considerably longer than typical radiation lengths, and large amounts of dense material are required to absorb the hadronic showers. The probability for a 10 GeV hadron to punch through the calorimeter is about 1%, depending on angles. Steel is used for reasons of cost, structural strength and to provide a good path for the return flux from the magnet.

The construction is alternating 5 cm sheets of iron and 1 cm sheets of scintillator, in two samplings each of 2.5 (3.5) absorption lengths in the C's (I's). The Gondolas (Bouchons) represent 1.1 (1.1) λ_a and the magnet coil another 0.3 λ_a. The energy resolution is:

$$\Delta E = 0.80 \times \sqrt{E} \tag{2.6}$$

---

[3] 1 absorption length (λ_a) is the distance over which a hadron has a probability of 1/e of surviving without a nuclear interaction. In iron, this is about 17 cm.

where the energy is measured in GeV. The spatial resolution is limited by the cell size, which is 0.9 × 0.8 m^2 for the C's, 0.9 × 0.9 m^2 for the large cells in the I's, and 0.4 × 0.5 m^2 for the small cells in the I's. In addition there is forward and very forward calorimetry (both electromagnetic and hadronic).

2.2.4 The Iarocci System

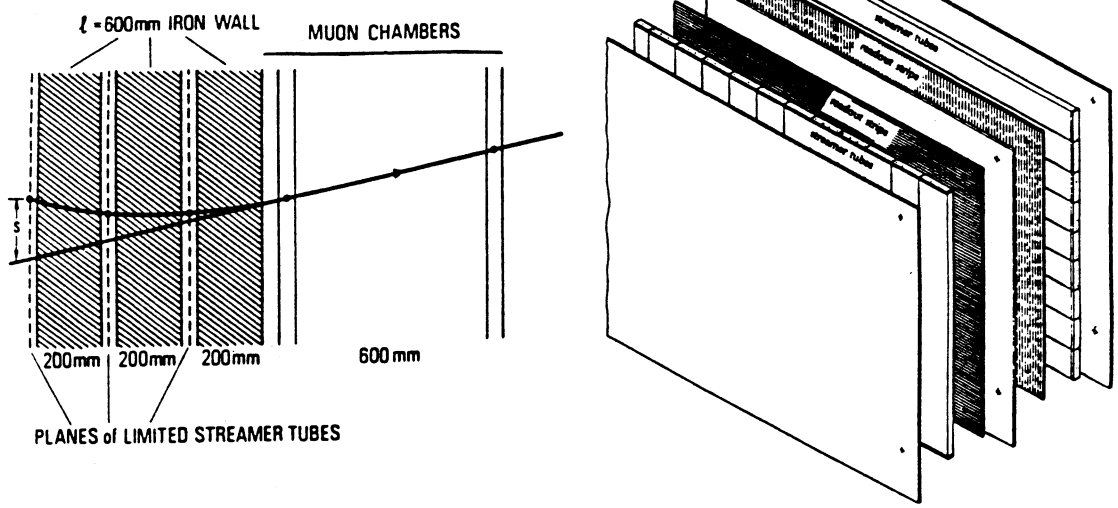

Figure 9: Section of Side Wall with Iarocci Chambers

This consists of iron shielding, complemented by Iarocci chambers [20], and added for the 1984 and 1985 runs. The aim was to improve the momentum determination of muons in the side walls by magnetising the iron to provide additional bending where the dipole field is least effective [21]. With the extra 60 cm of iron, it was anticipated that there would be a reduction in punch through to the side muon chambers, and the trigger rate from mesons decaying in flight to muons would be reduced. Further, the magnetic field would also reduce the muon trigger rate by deflecting slow particles (see section 2.2.6).

The side walls consist of three layers, each of 20 cm iron, interleaved with Iarocci chambers. The

chambers are operated in a limited streamer mode.[4] Each plane consists of parallel gas-filled (25% argon, 75% isobutane) plastic tubes, 1 cm × 1 cm in cross-section. Charged particles ionise the gas, and the liberated electrons accelerate towards the central anode wire in the high electric field (the potential difference is 4.2 kV). Simultaneously, anions move towards the earthed graphite coating of the tubes and a streamer develops. The charge on the tube induces a charge on the readout strips which lie perpendicular to the tubes (see figure 9). Since charge is deposited on several strips, a Gaussian is fitted to the distribution and a resolution of 0.5 mm in the direction of the tubes is obtainable. Each chamber has two crossed planes to allow a complete measurement of position. In addition, there are 2 (1) pairs of crossed planes in the forward (bottom) regions. The Iarocci chambers are simple and inexpensive to construct, and do not require complicated electronic timing.

2.2.5 The Muon Chambers (or Aachen Chambers)

These are large, modular drift chambers constructed from aluminium drift tubes [22]. They cover an area of about 700 m^2, or about 70 % of the solid angle. There are 12, 12 and 4 modules (each consisting of two chambers) in the forward, side and top regions, respectively. Each chamber has tubes in both transverse directions. However, in the bottom region, due to space limitations, there are 8 small and 2 large chambers which have tubes parallel to z only.

Part of a module is shown in figure 10. The chamber separation of 60 cm allows good position and angle measurement, which is important for the triggering (see section 2.2.6) and momentum determination (see chapter 3). The tubes are constructed from extruded aluminium and are glued together. Part of a muon tube, with the associated electric field lines, is shown in figure 11. The offset between tubes in adjacent layers resolves ambiguities associated with the drift times. In all but the bottom tubes, there is readout only at one end of the sense wires. In the bottom, timing is used to get a very rough measurement of the z coordinate.

Muons can be identified offline by:

---

[4] A streamer is like a spark, but less energetic. It is 'propagated' by photons emitted from the argon, and this process gives a gain of about 10^6. The streamer is 'limited' by the isobutane absorbing the photons. The streamer mode is useful because the gas provides the gain, so that amplifiers are not needed. Because they are 'limited', the dead time associated with streamers is avoided.

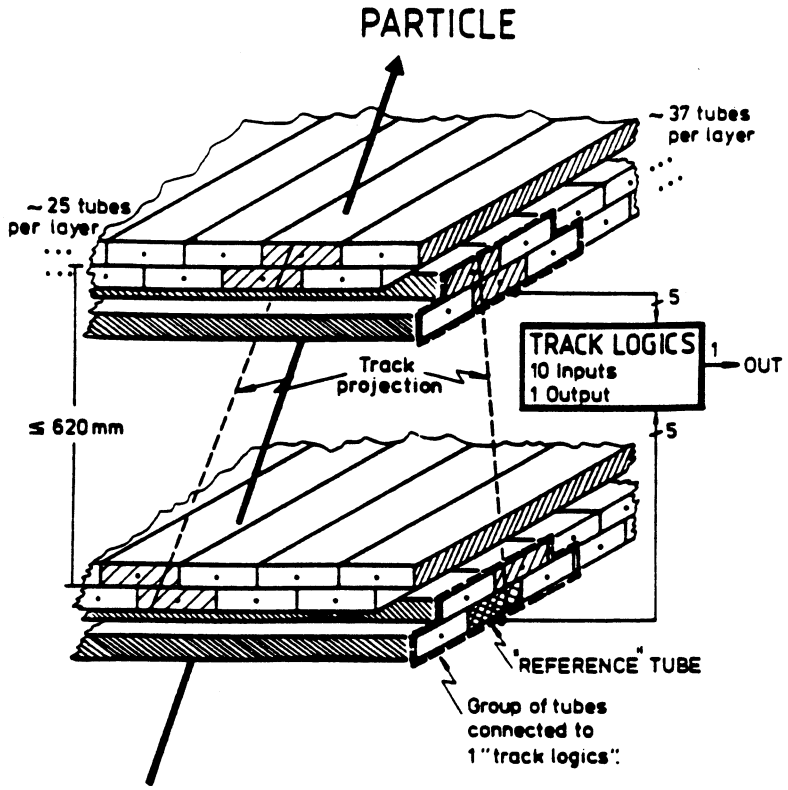

Figure 10: Part of a Muon Chamber Module

1. a charged track in the CD,
2. a minimum ionising deposition in calorimeters (1 to 3 GeV, typically),
3. an Iarocci cross and/or a muon chamber track.

2.2.6 The UA1 Trigger

Beam crossings occur at 1.3 × 10^5 Hz in the UA1 detector, while interactions occur at a rate which is an order of magnitude lower, depending on the actual luminosity. It is essential that the event rate is reduced because i) the tape writing capability is limited to 4 or 5 events per second, and ii) most of the interactions are low energy collisions with soft gluon exchange, and consequently are not of

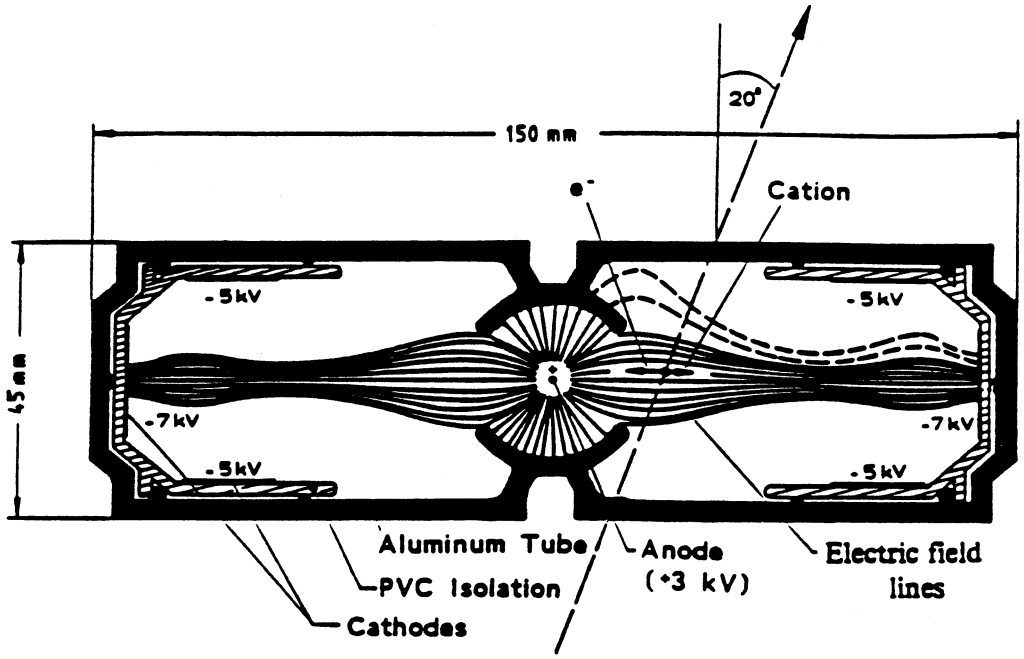

Figure 11: Transverse Section of a Muon Tube

Table 6: The Muon Chamber Parameters

Max chamber size	$4 \times 6\ m^2$
Tube cross-section	$15 \times 4.5\ cm^2$
Gas	40% argon + 60% ethane
Electric field	> 0.5 kV/cm
Drift velocity	5.3 cm/μs
Maximum drift time	1.5 μs
Number of sense wires	5200
Spatial resolution	300 μm

great interest. The trigger must decide which events to keep, while introducing the minimum of dead time.[5] This is done in a number of steps.

[5] time in which new events cannot be considered, and are thus lost, because the trigger or data acquisition system is still processing earlier events

The pretrigger consists of scintillation hodoscopes covering angles extending down to 0.6° from the beam direction [23]. For normal data taking, we demand that the hodoscopes at both ends of the detector give a signal in time with the beam crossing, to a few ns. These are 96 ± 2% efficient at detecting non-diffractive $p\bar{p}$ interactions. There are two first level triggers: one for the calorimeters, and another for the muon chambers. They are both hard wired processors which use look-up tables loaded into RAM.

The Calorimeter Trigger

The calorimeter trigger [23] adds all the individual signals coming from any cell to form a total signal for that cell. The results from neighbouring cells are then combined. These signals are then compared with look-up tables which allow for the pedestal subtraction and the geometric position of the corresponding cells when finding the transverse energy. The various possible trigger conditions are:

- Single electron: E_t > 10 GeV in adjacent electromagnetic cells, about 96% efficient [24].
- Di-electron: two clusters with E_t > 6 GeV in adjacent electromagnetic cells.
- Jet: E_t > 25 GeV in 4 adjacent electromagnetic cells or 4 hadronic cells.
- High scalar E_t: total transverse energy in calorimeters > 80 GeV.
- Missing transverse energy: left-right E_t imbalance > 17 GeV.

The Fast Muon Trigger

The first level muon trigger [25] uses only the information about which tubes have been fired in the muon chambers. In the time required to make a decision, the timing information is not available. For each tube in the first layer of the chambers (a so called 'reference tube'), there is an associated group of 10 tubes in the same projection (see figure 10). For this group, there are several configurations of fired tubes which are recognised as track candidates, corresponding to muons originating at the vertex. All configurations are represented by addresses in RAM, and the contents of these addresses indicate whether a given configuration corresponds to a track candidate or not. Every beam crossing, the pattern of fired tubes is transformed to an address, and the corresponding contents

are checked. All groups in every muon module are checked, and the trigger is fired if two tracks in projection are found in a module (only one projection is required in the bottom). The allowed tracks point back to the nominal vertex to within $\pm 9°$ - this removes most of the cosmic rays, beam halo[6] and low energy muons (less than about 1 GeV after the shielding) which are substantially deviated by multiple scattering. The di-muon trigger is satisfied if two such candidate muon tracks are found in separate modules. In practice, there is an increasing background from penetrating hadrons, as one considers regions closer and closer to the beam direction. Therefore, a large region of the forward chambers is vetoed for the single muon trigger in order that the trigger rate should be manageable. As the luminosity falls, the veto area is reduced in order to increase the acceptance. The di-muon trigger rate is considerably less, and so this trigger uses almost all the sensitive area.

Final Level Trigger and Data Acquisition

The central trigger processor receives signals from the pretrigger and the first level triggers, and makes the decision as to whether to keep the event. Interesting events are then digitised; the data are compressed to 120 kbytes and passed to the emulators. UA1 uses five emulators[7] running in parallel. These execute Fortran code which performs a rapid and simple event reconstruction, and then makes the final event selection. Here we describe the code used for the muon selection [26].

Using the timing information, a track is reconstructed in the muon chambers and this is required to point to the vertex within a certain tolerance which is determined by Monte-Carlo and takes account of i) the spread of the vertex, ii) the magnetic deflection, iii) multiple scattering, and iv) the resolution. If a good track is found, the program searches for a corresponding track in the CD. This is done by searching in a road ± 30 cm in $x-y$ and ± 40 cm in $y-z$ between the muon chamber track and the vertex. In this road, the reconstructed digitisings are histogrammed and a search is made for a concentration of points corresponding to a fast (and thus straight) track. If the corresponding digitisings can be found, a rapid circle fit is made to estimate the momentum, and the event is accepted

---

[6] The halo is a swarm of muons which travel within the accelerator tunnel in time with the particle bunches. The muons originate from interactions caused by stray beam protons colliding with the walls of the beam pipe or with gas molecules.

[7] An emulator is a copy of the central processing unit (CPU) of a mainframe computer but without the peripherals.

as a muon candidate if the p_t exceeds 2 GeV/c.

The input rate to the emulators is 10 Hz, while the code takes about 0.5 seconds per event to execute, with an output rate of about 4 Hz. Events are then passed to the online computer which formats the events and writes them onto magnetic tape.

Special trigger conditions are implemented to collect cosmic ray data, which are used for calibration and alignment. Scintillation hodoscopes are placed at the top and bottom of the side muon chambers. Cosmic rays are required to trigger pairs of diametrically opposite hodoscopes - this ensures that they give long tracks through the CD. The Bouchon hodoscopes are used for triggering on horizontal cosmic rays.

3. IMPROVED MOMENTUM ESTIMATES USING THE CD AND THE MUON CHAMBERS

In this chapter, we discuss the standard reconstruction in the CD. This is followed by discussion of a method to improve the quality of the CD tracks. The remainder of the chapter is occupied by a description of how the muon and Iarocci chambers can be used to improve the momentum estimates of high momentum muons.

3.1 Standard CD Reconstruction

3.1.1 Pattern Recognition

This is discussed in depth in [27]. Here, we summarise the important points. The individual drift volumes[8] of the CD are searched independently for 'chains' of digitisings. Using the wire numbers, the drift times and the z coordinate, one looks for three hits which lie in an approximate line. Then by linear extrapolation, one searches for another hit on the following wire. The search is repeated using the last three hits each time, until the chain is broken by a gap greater than one missing hit, or a wire plane is reached. This is repeated for all chains that can be found in each drift volume. The chains are then broken down into segments of typically 5 to 10 hits. A parabola is fitted to these points, and the point lying at the centre of the parabolic arc (the 'master point') is found. For each chain, the master points are used to obtain a parameterisation of the chain using an improved approximation to a circle. Finally, chains from different drift volumes are linked up, to form the track candidates.

3.1.2 Track Reconstruction

After the digitisings comprising a given track have been identified, the coordinates of these points have to be obtained [28]. The $x-y$ coordinates are found from the drift time and the known wire position. The drift time is corrected for:

---

[8] the regions separated by the wire planes

i. time of flight for the ionising particle to travel at the speed of light from the vertex;

ii. propagation time for the signal to travel to the ends of the wire;

iii. time for the pulse to exceed the hit threshold in the electronics - depends on the pulse height - time slewing;

iv. angular correction to allow for tracks which are not perpendicular to the drift direction - the point of the trajectory immediately 'upstream' of the wire is not the source of the first charge to reach the wire;

v. effect of diffusion on the pulse recorded on the wires.

The last two depend on $\tan\gamma$, where γ is the angle between the track in question and the normal to the drift at any point (see figure 6). The wire positions are determined by surveying the detector and are corrected for:

a. sag of the CD and twists;

b. displacements of the six chambers which make up the CD;

c. electrostatic displacement of the wires.

The z coordinate is calculated offline using the principle of charge division. The charge collected on a wire, as a result of a passing particle, flows to the left and right hand ends. The ROP's sum the charges collected, $Q_L{}^i$ and $Q_R{}^i$, for each hit on each wire in 32 ns bins, up to a maximum of 8 bins:

$$Q_L = \Sigma\, Q_L{}^i \quad \text{and} \quad Q_T = \Sigma\, (Q_L{}^i + Q_R{}^i) \tag{3.1}$$

Q_L and Q_T are saved on tape, and their ratio (found offline) gives an estimate of the z coordinate of that hit, as a fraction of the wire length. Corrections are made to allow for the effective electrical wire length, the difference in gains of the amplifiers at the ends of the wire and their biases and resistances.

Many of the required calibration constants can be determined using real data, and demanding that the reconstructed tracks have sensible behaviour: that the distributions of tracks are left-right symmetric and that the digitisings lie in continuous curves.

3.1.3 Parameter Estimation

Tracks are fitted in the $x-y$ plane using parabolic approximations to circles [29]. The digitisings are weighted according to their pulse height. For each track, the digitising which has the worst fit is removed if it fails certain criteria and the track is refitted. This procedure is repeated until a satisfactory fit is obtained. From this, the curvature can be estimated for each track, and this is proportional to the reciprocal of the component of the momentum in the bending plane, $p_\perp^{-1}$. The measure of the fit quality is given by the so called 'Sadoulet chi-squared'. This is the well known normalised variable defined in [30]. The distribution of this variable (the label 'chi-squared' is a misnomer) is approximately Gaussian, with unit width and zero mean.

To determine the fit in the z direction, the arc length (s) is calculated, where $ds^2 = dx^2 + dy^2$. Subsequently, a straight line fit is made in the $s-z$ plane. This leads to an estimate of the angle (λ) between the track and the bending plane ($z=0$). The quality of this fit is usually expressed in terms of the chi-squared per degree of freedom.

The reciprocal momentum is determined from:

$$p^{-1} = \cos\lambda \, p_\perp^{-1} \tag{3.2}$$

The main source of error for high momentum tracks comes from the estimate of the curvature:

$$\kappa \approx 8s/l^2 \tag{3.3}$$

where s is the sagitta of the track and l is the track length. The largest fractional uncertainty is on s, and this will vary roughly like the reciprocal root of the number of digitisings on the track, and thus the uncertainty behaves like $1/\sqrt{l}$. Thus the error on p^{-1} is a function of geometry and not momentum.

Finally, the interaction vertex is found by using the well measured tracks and then the track fitting is repeated including the vertex as a high weight point on the track.

3.2 The Automatic Fixup Procedure

Using the standard reconstruction procedures, once the digitisings are assigned to the track candidates by the pattern recognition, that is it! The track fitting methods do not allow for the use of digitisings not assigned to a given track. With hindsight, it is possible to make more intelligent decisions. Sometimes, it is easy to see why a certain digitising may be dubious or why another digitising has been overlooked by the chaining. This is realised by scanning events on a 'high resolution graphics display facility' - otherwise known as a Megatek. A physicist is well suited to pattern recognition, and the tracks are readily identified in the $x-y$ plane (see figure 7). Using an interactive method known as 'hand fixup', the scanner can chose to add or remove digitisings from a track. Unfortunately, this is both time consuming and subjective. Therefore, an automatic procedure, Autofixup, has been established.

At the heart of Autofixup is a routine which uses the fitted track parameters for a given track to predict the expected drift times on every wire which the track passes. These hits are compared with the real hits on the wires. This allows additional hits to be identified. Further, hits which are questionable for some well defined reason are rejected. Examples of problems are: overlapping pulses from nearby tracks, large $\tan\gamma$'s, large drift times, large z coordinates, large errors, bad drift angle, hits close to wire planes. Finally, using the parameterisation of the track, an improved estimate of $\tan\gamma$ can be made - normally this is estimated early in the chaining process for a cluster of four digitisings.

3.2.1 Results from Autofixup

We have tested the program on the 1985 $W\rightarrow e\nu$ events (110 events) [31]. We find that the number of hits per track is reduced by about 10%, while the Sadoulet chi-squared falls on average by about 1 unit. Not surprisingly, the inverse momenta estimates are highly correlated before and after Autofixup is applied (see figure 12). Looking at the quantities $Q/p|_{old}-Q/p|_{new}$, we find a mean of -0.0008 with an rms for the distribution of 0.0122. We also consider $Q/p|_{old}-Q/E$ and $Q/p|_{new}-Q/E$, where E is measured by the calorimetry. These distributions are symmetric with widths of 2.2×10^{-2} and 2.0×10^{-2} $GeV^{-1}c^2$ respectively. This suggests that the improvement on the value of p^{-1} is

about 10%. The errors before and after are shown in figure 13. The mean value of the ratio $\rho \equiv <\sigma_{new}/\sigma_{old}>$ is 0.84 - suggesting a slightly greater improvement.

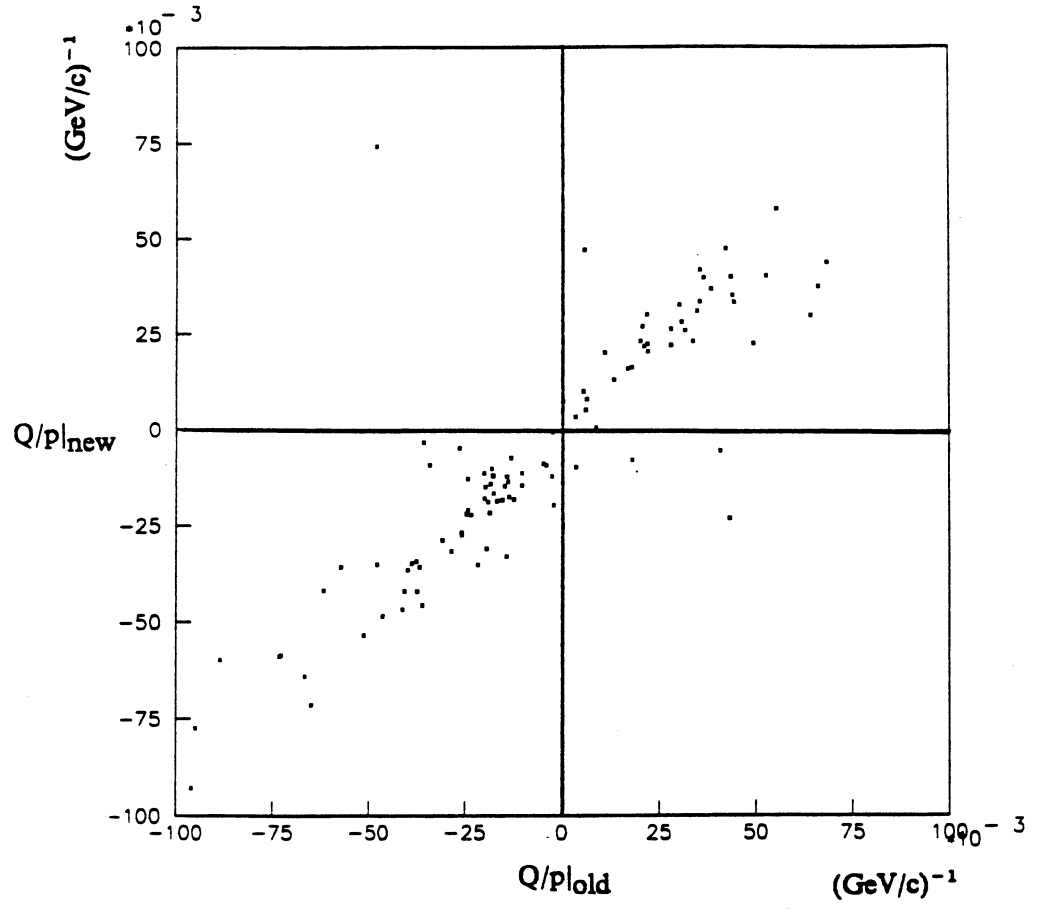

Figure 12: Q/p Before and After Autofixup

When we apply the method to the W→$\mu\nu$ candidates, we find that the changes in p^{-1} are smaller than for the electrons. Also, the reduction in error is smaller, with ρ = 0.96. The reason for this is the tight selection criteria applied to the muon candidates in the CD (see chapter 6). In particular, there is the isolation of the tracks and the checks to remove background events coming from the decay of pions and kaons. While it has been demonstrated that this method is generally useful, we conclude that it is not of great benefit when used on events which have very strict track requirements. For this reason, we have not used it for the muonic Z candidates.

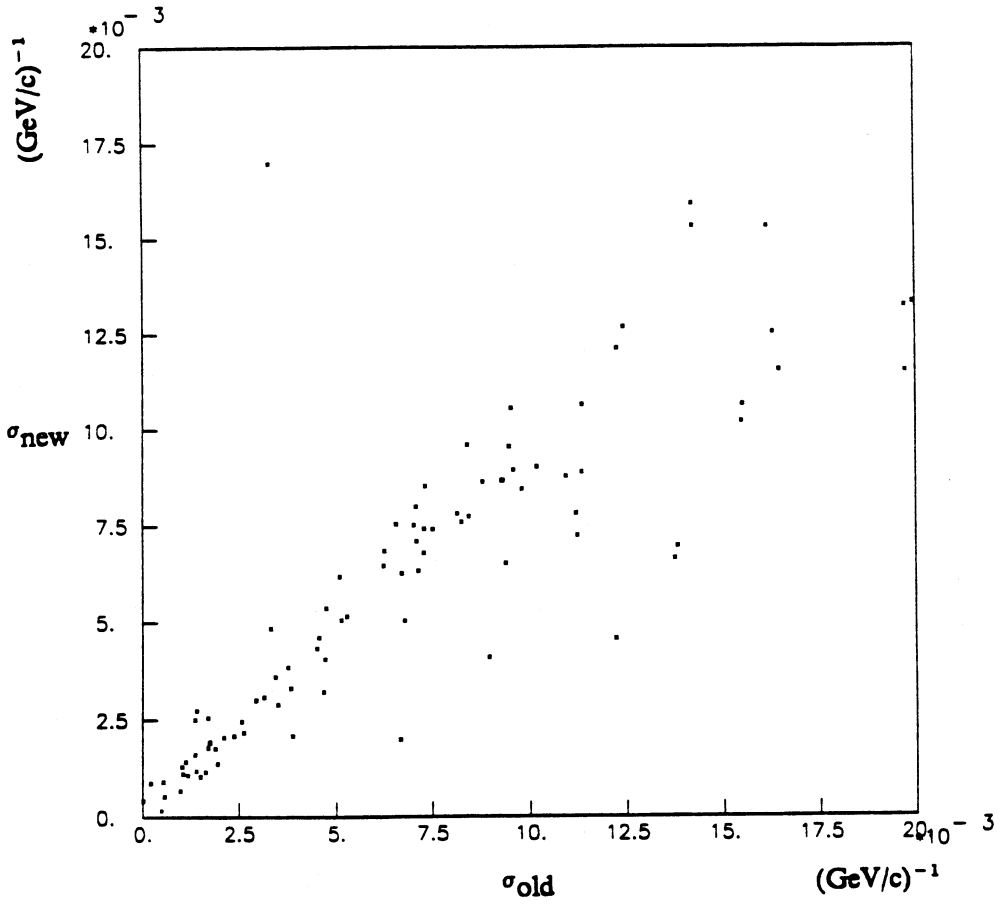

Figure 13: σ(1/p) Before and After Autofixup

3.3 An Overall Momentum Fit with the Muon Chambers

High p_t muons are identified by tracks in the muon chambers (or Aachen chambers) and the Iarocci chambers, which we will collectively refer to as the muon chambers. The hits in these chambers can be used in conjunction with the known magnetic fields inside UA1 to estimate the momentum of the muons. The magnetic field causes a muon to bend so that the hits in the muon chambers do not point exactly to the interaction vertex. In practice, using this information alone leads to problems, since the long lever arm of the muon chambers can introduce large fluctuations in the estimated momentum, and the estimate is very sensitive to any reconstruction problems in the outer chambers. A better approach is to use, in addition, the direction of the muon at the vertex, as determined by the

CD. This estimate of momentum is independent of the estimate derived from the curvature of a track in the CD - at least, to first order. In practice, there is some correlation between the angle Φ and p^{-1}, measured in the CD.

The error on $r \equiv p^{-1}$ is dominated by the error on the sagitta (see equation 3.3). In the CD, $\sigma(s)$ is independent of the momentum for a track in a given direction. However, $\sigma(s)$ using external points is dominated by multiple scattering (although, see later) and this falls like p^{-1}. So a determination of r from the muon chambers has an error which varies like r. Therefore, at higher momentum (smaller r) the muon chambers become increasingly more useful in estimating the momentum.

Having obtained an estimate of r from the muon chambers alone, r_μ, this can be combined with the measurement from the CD, r_C, to obtain the overall momentum fit (OMF) estimate. In practice, this is done in a single coherent manner, as described below, and it is not necessary to calculate r_μ separately. For the purposes of understanding the procedure, we should test i) the computer code to perform the fitting - which is non-trivial, and ii) our description of the detector. To achieve this, we study the estimate from the muon chambers alone (with the track direction from the CD). This is done by setting the weights for the CD momentum equal to zero.

3.3.1 Method for Obtaining the Fitted Momentum

Here, we present an outline of the method used to obtain the momentum estimate from the muon chambers - more details are given in reference [32]. The important quantities are illustrated in figure 14. We envisage a set of parameters, a (implicitly a vector), which describe the track in the CD at the vertex. These parameters consist of two positions, two angles and the reciprocal momentum. The hits in the muon chambers are denoted by x (again, implicitly a vector). There are up to 6 hits in the Iarocci chambers for each muon, while the hits in the Aachen chambers (of which there are up to 8) are replaced by 2 hits in each of the 2 planes of the chambers, corresponding to the intersection of the fitted track with these planes. The crux of the method is that the $\{x_i\}$ are functions of the $\{a_j\}$, and in particular the reciprocal momentum, r. So we write that $x = x(a)$. If the covariance matrix for a is A, and for x is X, we can form a chi-squared for the track:

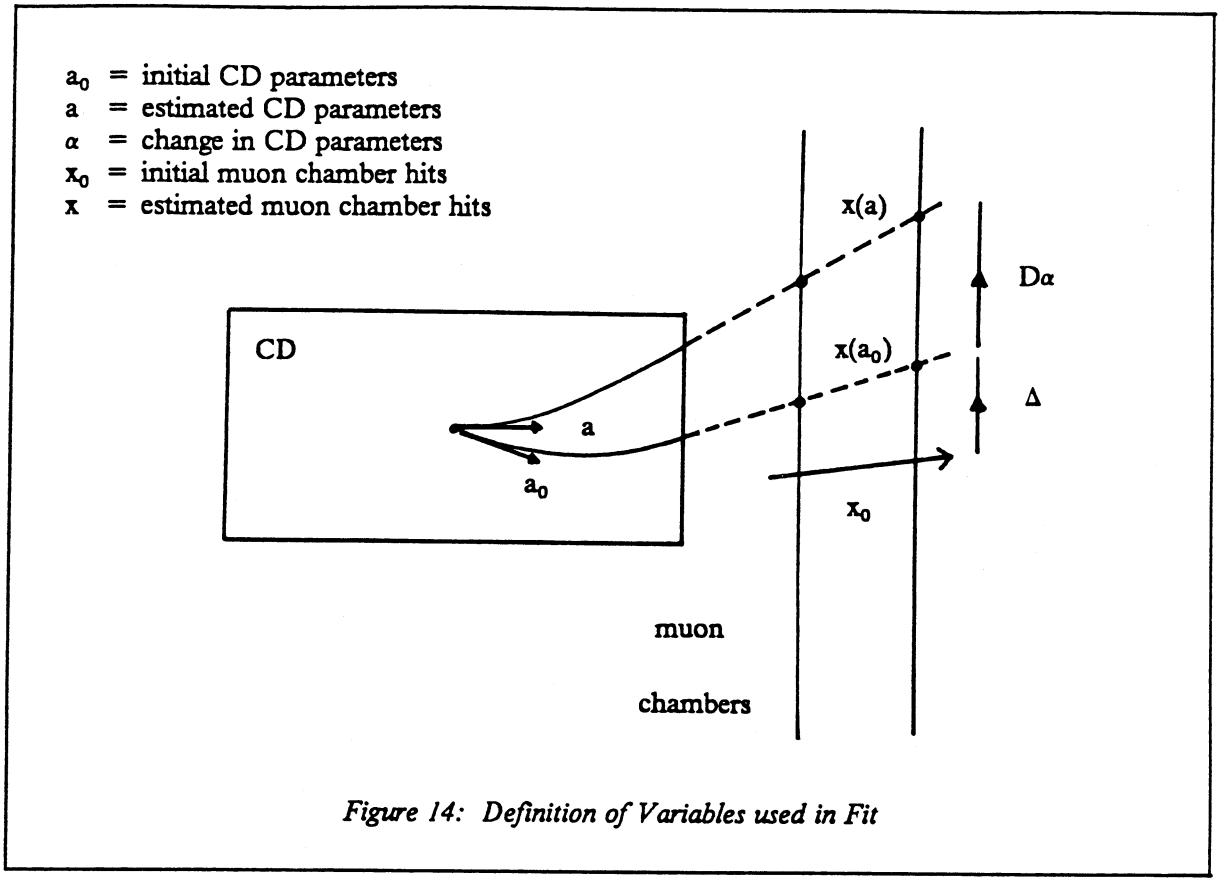

Figure 14: Definition of Variables used in Fit

$$\chi^2 = (a-a_0)^T A^{-1}(a-a_0) + (x-x_0)^T X^{-1}(x-x_0) \tag{3.4}$$

where the subscript '0' denotes the actual measurements. We measure the departure from the measured parameters in the CD by $\alpha \equiv a-a_0$. We anticipate that the changes in a will be such as to produce linear changes in the coordinates x(a). In other words, we assume that the derivative $D \equiv dx/da^T$ is constant (note: D is a matrix, which is not square, in general). The difference in the x values becomes:

$$x(a)-x_0 = [x(a)-x(a_0)] + [x(a_0)-x_0] = D\alpha + \Delta \tag{3.5}$$

where Δ is the difference between the measured hits in the muon chambers and the hits found on extrapolation from the CD using the measured parameters. Minimising χ^2 with respect to α gives the estimate for α:

$$\hat{\alpha} = - GD^T X^{-1}\Delta \tag{3.6}$$

where

$$G^{-1} = A^{-1} + D^T X^{-1} D \tag{3.7}$$

The covariance matrix for a is given by $^1/_2\partial^2\chi^2/\partial a\partial a^T$ and is found to be G. The resulting value of the chi-squared is found by substitution into (3.4). After a considerable amount of algebra, one finds that

$$\chi^2 = \Delta^T(X + DAD^T)^{-1}\Delta \tag{3.8}$$

It is useful to consider the quantity $\hat{\alpha} = \hat{a} - a_0$ - in particular, the momentum term $\hat{r} - r_c$. After even more algebra, it is possible to show that covariance of the of $\hat{\alpha}$ is $A - G$. Thus the variance of $\hat{r} - r_c$ is $\sigma_c^2 - \sigma^2$ (where σ is the estimated error on r), and the quantity $(\hat{r} - r_c)/\sqrt{(\sigma_c^2 - \sigma^2)}$, known as the 'stretch' or 'pull', has a normalised Gaussian distribution.

The equation for $\hat{\alpha}$ is readily suited for our application. Δ is trivially calculated. X contains two components: the intrinsic resolution in the muon chambers and the multiple scattering - these are combined in quadrature. In practice, it is found that the matching between the CD and the muon chambers cannot be explained by just these resolution effects, and there is some unknown source of systematic problem in performing extrapolations. For this reason, error floors are added to the intrinsic chamber resolution to describe the discrepancies in the matching. The multiple scattering is very complicated since it introduces correlations between hits in different planes. The form of these correlations is given in appendix A. D is calculated explicitly, by making small changes in each of the parameters a_j and finding the change in the extrapolated points x_i. This is done by using extrapolation routines and the known geometry and magnetic fields. A is found during the CD reconstruction.

Some Appropriate Comments

1) Using the muon chamber information only (that is, not using the CD estimate), at very high momentum, the floor on the hits dominates the error on the momentum. At lower momentum, the multiple scattering, which is a function of momentum, dominates. The error on the hits in the muon chambers is therefore a function of momentum, and so the estimated error is a function of the estimated momentum.

2) In deciding whether the estimate $\hat{r}$ is an unbiassed estimate of the true reciprocal momentum, r_{true}, one should consider the variations of the measured hits x_0, which lead to a spread in the estimated values $\hat{r}$. The key point to note is that the distributions of x_0 are Gaussian, centred on the points corresponding to r_{true} and with a width also determined by r_{true}. Therefore, the distribution of $\hat{r}$ is also Gaussian with a width given by $\sigma(r)$ - where r is evaluated at r_{true}, not $\hat{r}$. Thus the estimate $\hat{r}$ is unbiassed, in the sense that its expectation value is r_{true}.

3) Using the CD measurement, it is easy to convince oneself that the overall solution presented here is effectively a weighted mean of the CD estimate of r and the estimate from the muon chambers (to see this: remove all D's and replace the vector quantities by simple scalars). Explicitly, we have:

$$\hat{r} \approx (r_c/\sigma_c^2 + r_\mu/\sigma_\mu^2) \div (1/\sigma_c^2 + 1/\sigma_\mu^2) \qquad (3.9)$$

We wish to evaluate the multiple scattering term in σ_μ at the true value of the momentum - this is not possible, and so we must use our best estimate. Thus, equation (3.9) is used iteratively, feeding in the current estimate in to the multiple scattering term. It can be shown (see appendix B) that this expression for the momentum leads to an unbiassed estimate of the true value.

To show that OMF is working properly, we must demonstrate:

1. r_μ really is unbiassed,
2. σ_μ provides a correct description of the spread on the estimates r_μ,
3. using both the muon chambers and the CD, $\sigma < \sigma_c$ - if we cannot reduce the error below that coming from the CD, we are wasting our time !

3.3.2 Tests with Cosmic Rays

To test OMF, the program was modified to use cosmic rays, which provide a high statistics sample of pure muons of fairly large momenta (of the order of 20 GeV/c) (see also [33]). Loose cuts were made on the cosmic rays:

1. We require that there should be a CD track with $p > 5$ GeV/c.
2. At either entry or departure, there should be a track in the muon chambers matched to the CD track with a mean matching chi-squared in the bending plane < 9.
3. The OMF fit is rejected if the OMF chi-squared[9] is > 15. High chi-squares are indicative of reconstruction problems rather than simple Gaussian fluctuations - these can be seen on the Megatek.

In order to test the situations encountered in $p\bar{p}$ data more realistically, each cosmic ray was split into an incoming and an outgoing track, with a dummy vertex located near the centre of the CD. For the incoming track, its momentum vector was reversed in the CD, and care was taken to reverse the energy loss when tracking the muon from the CD back to the muon chambers. Using the momentum estimates from the muon chambers only gives two independent estimates of the same momentum.[10] We distinguish between cosmic rays travelling in different directions, and thus passing through different sets of muon chambers. The three categories are:

- horizontal: $+x$ and $-x$; we distinguish cosmic rays passing through the large or small muon chambers,
- vertical: $+y$ (top) or $-y$ (bottom),
- side: $+z$ or $-z$.

The results presented here correspond to the 1984 cosmic ray data, for which there was no reliable Iarocci information, and so only the Aachen chambers were used.

It was found that the scatter plots of the reciprocal momentum estimates from the muon chambers versus the CD measurements showed strong correlations (see figure 15), indicative that it is possible to measure 1/p using the muon chambers. To check this more carefully, we studied the

---

[9] The number of degrees of freedom is equal to the number of hits used in the muon chambers, when the CD momentum is used, and one less otherwise.

[10] Note that if we were to use the fit including the CD, the two estimates would not be independent because of the common CD momentum. With more effort, the two halves of the CD track can be fitted separately to allow independent estimates to be made. This was done: however the results are not so important for the discussion of this chapter, and are not presented.

quantity $(Q_\mu r_\mu - Q_c r_c)$, where Q is the estimated charge, which is related to the sign of the curvature. All the distributions were found to be approximately Gaussian in appearance, and were well centred. The parameters are given in table 7 (the units are $GeV^{-1}c^2$). The mean momentum of the sample of cosmic rays is given - the momentum spectrum was approximately exponential. The size of the rms for each category is readily explained by the geometry. In using the charged quantities, we are sensitive to systematics which might arise due to the misalignment of the muon chambers with respect to the CD.

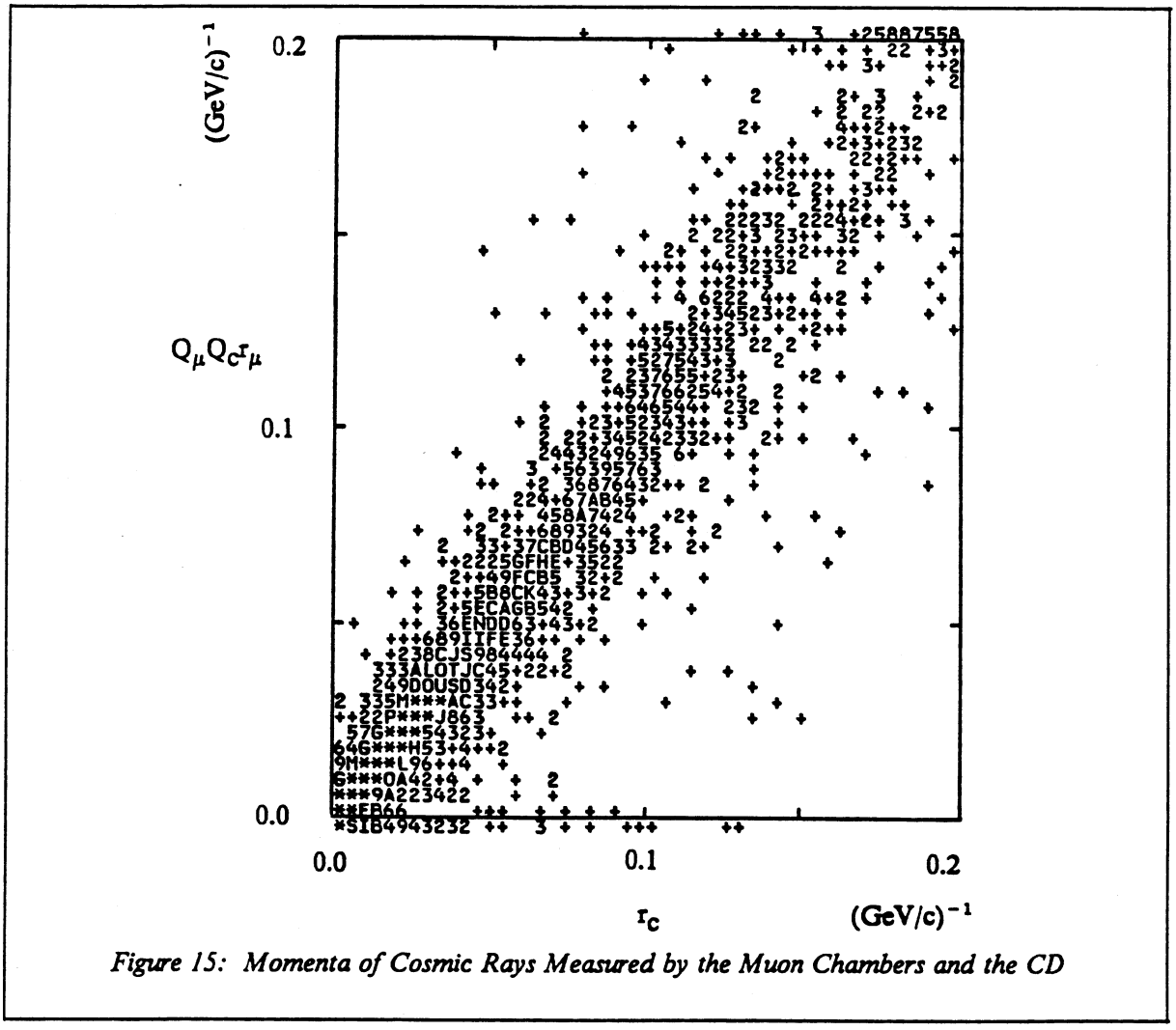

Figure 15: Momenta of Cosmic Rays Measured by the Muon Chambers and the CD

Table 7: Difference in Momentum Estimates from the Muon Chambers and the CD

	N	<p>	mean (m)	rms (s)	$m \div s/\sqrt{N}$
horizontal − large	3774	37	-0.21×10^{-3}	1.1×10^{-2}	−1.14
horizontal − small	4278		$+0.58\times10^{-3}$	1.0×10^{-2}	+3.87
vertical − +y	2558	19	-0.88×10^{-3}	2.8×10^{-2}	−1.58
vertical − −y	1665		$+2.57\times10^{-3}$	4.8×10^{-2}	+2.19
side − +z	2712	26	-0.36×10^{-3}	4.7×10^{-2}	+0.40
side − −z	2197		$+2.05\times10^{-3}$	4.7×10^{-2}	+2.06

The errors on r are dominated by the floors on the resolution and the multiple scattering. For muons produced in the decay of a W or Z, the momenta will tend to be higher (of the order of 50 GeV/c) and, consequently, the errors due to the multiple scattering will be lower. On the other hand, the CD errors on the track directions, which feed in to the error, will tend to be lower for the cosmic rays, which tend to have better defined tracks in the CD. Nevertheless, we can make some useful comparisons for the horizontal (or forward) cosmic rays: $\sigma_\mu \approx 1\times10^{-2}$, with a systematic uncertainty (estimated from the mean of the distribution) less than about 2×10^{-4}, while σ_c evaluated for $W\rightarrow\mu\nu$ candidates is about 0.5×10^{-2}. Therefore, we can see that the error from the muon chamber estimate is of the same order of magnitude as the error from the CD, and it makes sense to use the combined estimate. If we consider the combined estimate as being effectively a weighted mean, then the error on the OMF value is $\sigma = 1/\sqrt{(\sigma_c^{-2}+\sigma_\mu^{-2})}$, and if σ_μ is approximately $2\sigma_c$, then this gives a σ of roughly 90% of σ_c, so we could expect a reduction in error of the order of 10%.

To test the reasonableness of the estimated errors on the momentum estimate from the muon chambers, we could consider the quantity $(r_\mu - r_c)/\sqrt{(\sigma_c^2+\sigma_\mu^2)}$. On the face of it, this quantity ought to be Gaussian, with a mean of zero and a width of one. In practice, because σ_μ is a function of the estimated quantity, r_μ (and for significant multiple scattering, $\sigma_\mu \propto r_\mu$), the distribution turns out to be significantly skew. To some extent, this can be alleviated by multiplying σ_μ by r_c/r_μ. However, at high momentum, the floors dominate, and the skewness returns in the opposite sense.

A good alternative is to obtain separate and independent estimates of r from the incoming and outgoing tracks. (Note: the momentum estimate is evaluated so as to be consistent with the estimate from the CD. So for $p\bar{p}$ interactions, it represents the momentum of muons at the point of creation - not after they have traversed the calorimeters.) If the incoming and outgoing muon tracks pass through muon chambers with similar geometry, then to first order the skewness encountered above is removed by the symmetry. Therefore, we limit our study to horizontal and side cosmic rays. We consider the quantity $(r_{in} - r_{out})/\sqrt{(\sigma_{in}^2 + \sigma_{out}^2)}$. The results are shown in table 8. The closeness to unity of the rms's is an indication that the error estimates from OMF are satisfactory.

Table 8: Difference in Momentum Estimates from In/Out Going Tracks

	N	mean (m)	rms (s)	$m \div s/\sqrt{N}$
horizontal	1980	−0.046	1.04	−2.0
side	1461	−0.084	0.95	−3.2

3.3.3 The Application of OMF to the W and Z events

OMF, incorporating the CD momentum estimate, has been applied where possible to the W and Z candidates (muonic decays) - these events will be discussed in chapters 6 and 7. The matching between the muon chambers and CD has been studied carefully only for the $\sqrt{s}$ = 630 GeV data, and so we use only these events. 53 out of the 57 muons in the W candidates have good chi-squareds (< 15). As will be seen in chapter 7, we require only one of the muons in a candidate Z event to have a muon track. In 1985, unfortunate statistical fluctuations resulted in only 1 out of 10 events with two good muon tracks; and, out of a total of 16 events, OMF was successfully applied to 24 muons. The mean and rms's of the stretches are shown in table 9. The most important are the stretches in the bending plane (r,Φ), since they relate to the momentum determination.

Table 9: Stretches for W and Z Events

		mean	rms
W	x	−0.20	0.97
	y	+0.02	1.02
	r	−0.07	0.98
	λ	−0.58	1.01
	Φ	+0.21	0.98
Z	x	−0.23	0.96
	y	−0.31	0.83
	r	+0.09	0.80
	λ	−0.44	1.05
	Φ	−0.10	0.95

The scatter plot of the OMF errors versus the CD errors on momentum for the W candidates is shown in figure 16. The mean of the ratio of OMF error to CD error is 0.76. Thus we conclude that OMF is successfully reducing the errors on the momentum estimation, and the studies with cosmic rays verifies that the procedure is fairly well understood.

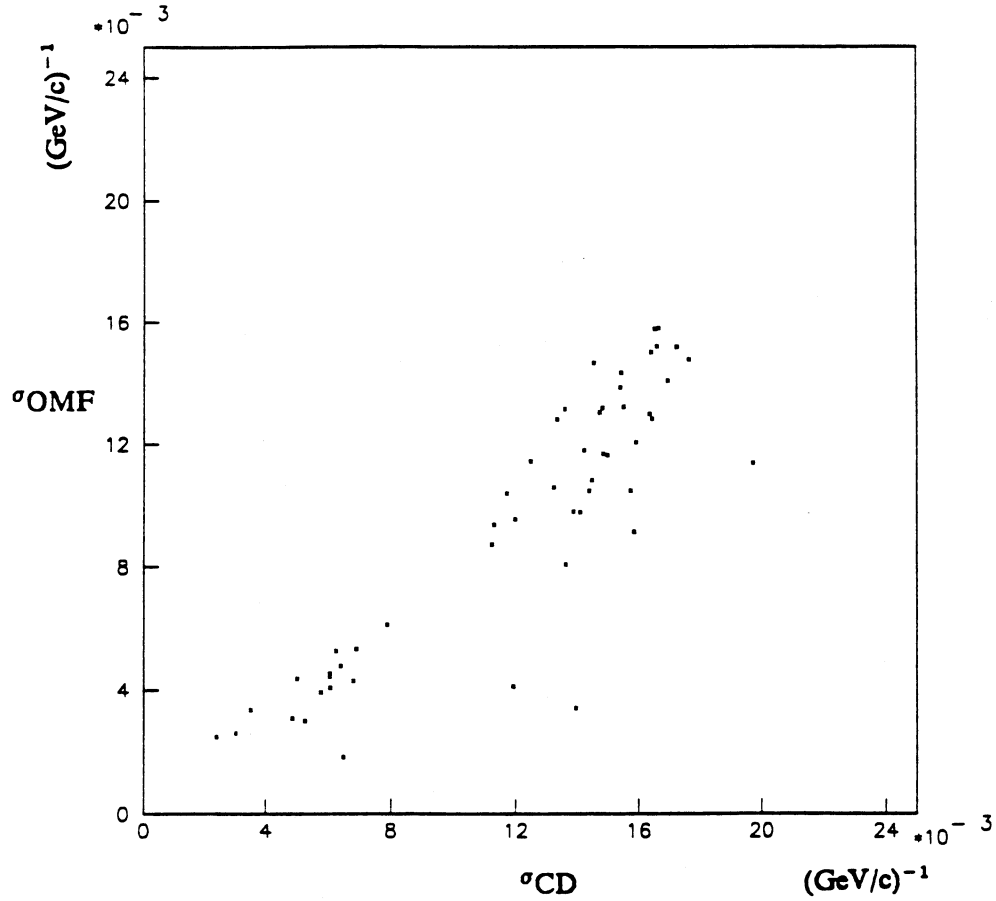

Figure 16: OMF Errors versus CD Errors for W→μν Events

4. LIKELIHOOD METHODS

Often with statistical methods there is no right or wrong way of presenting results. The only unambiguous procedure is to present all measurements and to let the reader derive the quantities in which he is interested. However, this is neither feasible nor useful. Therefore the experimentalist must choose some scheme for deriving meaningful quantities. Generally, the problems encountered are less significant where the statistics are high, but with low statistics, different procedures (namely, classical or Bayesian approaches with different prior densities) may lead to very different numerical conclusions (see, for example, reference [34]). Thus, the best one can hope to do is to utilise a simple method which leads to robust[11] conclusions, while clearly explaining the method and the assumptions. Further, any results should be interpreted with a measure of care, since even exact methods do not always lead to the conclusions one would imagine.[12]

In the analysis described in this thesis, we have relied heavily on likelihood methods. These methods are good because:

- They can incorporate as much information as is available and test the complete shape of a distribution.
- They can be used in a bin free way and need not depend on the position of cuts.
- They provide simple methods for estimating variances and confidence limits.
- In testing distributions for new signals, they are not very sensitive to fluctuations or systematic deviations outside the signal region, whereas naive chi-squared tests may be.

With respect to the last comment, we note that chi-squared methods should be reserved for tests of goodness of fit; and that parameter estimation and the derivation of confidence limits are the domain of likelihood methods. In what follows, we prove some of the important results which are used later in this thesis. We will consider simple cases, where a single quantity is estimated and there is only one

---

[11] i.e. with minimal sensitivity to small changes

[12] In reference [34], James points out that exact methods for calculating confidence levels for low statistics Poisson problems often lead to an over-satisfaction of the required confidence level. That is, in trying to calculate a 90% C.L., the actual level represented by the limit (which is a function of the true, yet unknown, mean of the distribution) is greater than 90%.

parameter to be measured - the appropriate generalisations are readily made.

4.1 Estimation of central value

We envisage a problem where we have N measurements of the quantity x: $\{x_i; i = 1,N\}$. We know that the measurements are distributed according to a probability density function (pdf) f(x|a) where a is an unknown parameter which we wish to estimate. Here, we consider the asymptotic situation where $N \to \infty$, although the case of finite N is considered later. If the true value of a is α, then the distribution of measurements is $dN/dx = Nf(x|\alpha)$.

The log likelihood[13] is defined by

$$\mathcal{L}(a) \equiv \Sigma \log f(x_i|a) \tag{4.1}$$

In the asymptotic limit, the sum gets replaced by an integral: $\Sigma \to \int dx\, Nf(x|\alpha)$. So the likelihood becomes:

$$\mathcal{L}(a) = N\int dx\, f(x|\alpha) \log f(x|a) \tag{4.2}$$

$$\Rightarrow \quad d\mathcal{L}/da = N\int dx\, f(x|\alpha)/f(x|a)\, \partial f/\partial a|_a \tag{4.3}$$

Evaluating this at $a = \alpha$ gives

$$d\mathcal{L}/da|_{a=\alpha} = N\int dx\, \partial f/\partial a|_\alpha \tag{4.4}$$

and since $\int dx\, f(x|a) \equiv 1$ by the normalisation condition of the pdf, the integral of the derivative with respect to a vanishes. Thus, (4.4) leads to $d\mathcal{L}/da|_{a=\alpha} = 0$. So we see that the likelihood has a turning point (a maximum) at $a = \alpha$. Therefore, the location of the maximum is an estimator of the true value of the parameter a.

---

[13] usually the word 'log' will be omitted

Note that in practice, a minus sign is often slipped into the definition of the likelihood (4.1). This is done simply because it is easier to handle with standard computer software (minimisation routines and histogram packages). This has little significance, other than inverting the likelihood curves so that maxima become minima.

4.1.1 The Discrete Regime

If the likelihood attains its maximum at $a = \alpha + \delta a$, then

$$0 = d\mathcal{L}/da|_{a=\alpha+\delta a} = d\mathcal{L}/da|_{a=\alpha} + d^2\mathcal{L}/da^2|_{a=\alpha}\delta a \tag{4.5}$$

$$\Rightarrow \qquad \delta a \propto d\mathcal{L}/da|_{\alpha} \tag{4.6}$$

The quantity in which we are interested is the expectation value of δa with respect to variations in the measurements $\{x_i\}$. Since the behaviour of the second derivative of the likelihood is fairly insensitive to the variations in the measurements,

$$E[\delta a] \propto E[d\mathcal{L}/da|_{\alpha}] \tag{4.7}$$

The expectation value is obtained by the integral of the probability of a set of measurements $\{x_i\}$ over all values. For independent measurements, this probability is the product of the individual pdf's. So the expectation of the first derivative is

$$E[d\mathcal{L}/da|_{\alpha}] = \int\prod_i dx_i\, f(x_i|\alpha)\, \{ \sum_j 1/f(x_j|\alpha)\, \partial f/\partial a \} \tag{4.8}$$

where the term in { } is the derivative of the likelihood. On rearrangement, this becomes:

$$E[d\mathcal{L}/da|_{\alpha}] = \sum_j \{ \int\prod_{i\neq j} dx_i\, f(x_i|\alpha) \}\{ \int dx_j\, \partial f/\partial a \} \tag{4.9}$$

As in the asymptotic regime, the second bracket vanishes, and so the expectation of the derivative is zero, and consequently the expectation of δa is also zero. Thus we find that the expectation value of the estimate of the parameter obtained at the maximum of the likelihood is equal to the true value of the parameter. Alternatives to this proof can be found in reference [35].

4.2 Estimating the Variance

Using the asymptotic methods, we consider statistical fluctuations of the measured distribution. Suppose the measured distribution is $N\{f(x|\alpha)+\delta f(x)\}$, then the likelihood becomes

$$\mathcal{L}(a) = N\int dx\ \{f(x|\alpha)+\delta f(x)\}\ \log f(x|a) \tag{4.10}$$

We expand $d\mathcal{L}/da$ at $a = \alpha+\delta a$, equating it to zero:

$$d\mathcal{L}/da|_a = d\mathcal{L}/da|_\alpha + d^2\mathcal{L}/da^2|_\alpha \delta a = 0 \tag{4.11}$$

The first term in (4.11) can be expanded in terms of δf, and in this expansion, the zeroth order term vanishes, as in (4.2)−(4.4). This gives

$$\delta a = -N\int \delta f/f\ \partial f/\partial a \div d^2\mathcal{L}/da^2 \tag{4.12}$$

We now seek the variance of a (or δa) due to variations from δf.

If we have a quantity $B = N\int dx\ f(x)b(x)$ where $f(x)$ is the distribution of x, then the discrete form of this quantity is Σb_i, where the sum is over all the measurements (this is the reverse of the step (4.1)→(4.2)). The variation of B due to statistical fluctuations of the measurements $\{x_i\}$ is $N\int dx\ \delta f\ b$. Using the discrete form, we know that the variance of B is

$$V(B) = NV(b) = N\{\ E[b^2]-E[b]^2\ \} \tag{4.13}$$

which becomes $N\{\ \int dx\ f\ b^2 - (\int dx\ f\ b)^2\ \}$. Identifying b with $(1/f\ \partial f/\partial a)$, we find that the variance of δa becomes

$$V(\delta a) = N\{\ \int dx\ f\ (1/f\ \partial f/\partial a)^2 - [\int dx\ f\ (1/f\ \partial f/\partial a)]^2\ \} \div (\partial^2\mathcal{L}/\partial a^2)^2 \tag{4.14}$$

The second term of the numerator of (4.14) vanishes, and the first term is readily shown to be equal to the negative of the second derivative of the likelihood. Thus we end up with our final result that the variance of δa, or equally of our estimate $\hat{\alpha}$, is

$$V(\hat{\alpha}) = -1\ /\ \partial^2\mathcal{L}/\partial a^2 \tag{4.15}$$

If the likelihood is parabolic, centred on the estimate $\hat{\alpha}$, with a curvature κ, then

$$\mathcal{L} = \mathcal{L}_0 - {}^1/_2\kappa(a-\hat{\alpha})^2 \tag{4.16}$$

and the variance is the reciprocal of the curvature, namely κ^{-1}. We note that at the 'one sigma' positions, i.e. $a = \hat{\alpha}\pm\sqrt{\kappa^{-1}}$, the likelihood falls by half a unit (see figure 17).

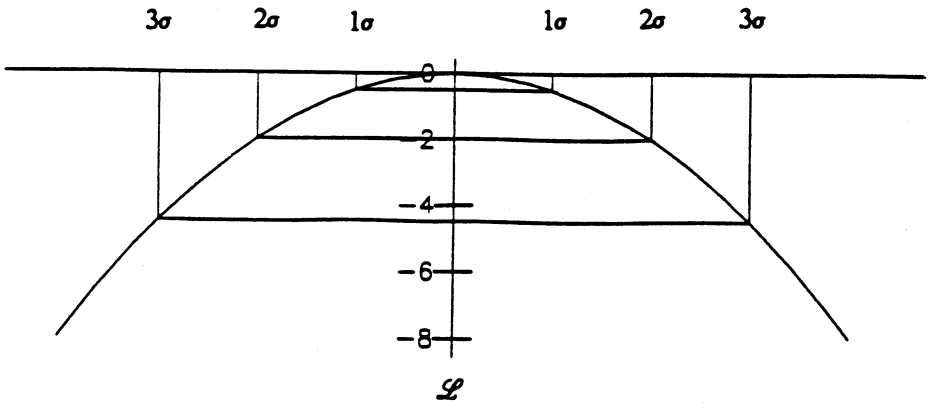

Figure 17: Parabolic Likelihood Curve

4.3 Changing Variables

4.3.1 ... for the Measured Quantities

We consider a change of variables from the measurements $\{x_i\}$ to $\{y_i \equiv Y(x_i)\}$. The pdf for y is given by $f_y(y) = f_x(x)J(y)$ where J is the Jacobian dx/dy. In the y representation, the likelihood becomes

$$\mathcal{L}_y(a) = \Sigma \log f_y(y_i|a) = \Sigma \log f_x(x_i|a) + \Sigma \log J(y_i)$$

$$= \mathcal{L}_x(a) + \Sigma \log J(y_i) \tag{4.17}$$

Seen as a function of a, the last term is a constant, and has no effect on the estimation of statistics from the likelihood, which depend only on derivatives of the likelihood. So we can use whatever functions of the measured quantities we find convenient.

4.3.2 ... for the Parameter to be Estimated

Next we consider the effects of a change of variable for the parameter which we are trying to estimate. If the parameter $a' \equiv \chi(a)$, then the probability of a measurement x is identical, regardless of whether it is viewed as a function of a or of a'. Thus the operational definition of the likelihood (4.1) is unchanged by a change of parameter variable, although the functional form is changed.

This means, in principle, we can transform parameter variables so as to obtain a parabolic likelihood. The interpretation of such a likelihood is straightforward, since it is essentially the logarithm of the pdf of a Gaussian distribution representing the distribution of possible values of the parameter to be estimated. (If the distribution of the possible values of the parameter a varies like $\exp(-{}^1/_2\kappa(a-\hat{\alpha})^2)$, then the likelihood varies like $-{}^1/_2\kappa(a-\hat{\alpha})^2$.) When the likelihood is parabolic, it was shown that it falls by ${}^1/_2$ from the maximum, one sigma above and below the central estimate. Since the likelihood is invariant, then the likelihood will also fall by ${}^1/_2$ at the values of the original parameter which would be transformed onto the plus or minus one sigma values. It is these values which we think of as the one sigma values of the original parameter. These 'errors' will not in general be symmetric, but they correspond to the (reverse) transformation of the symmetric errors on the Gaussian variable, or alternatively, the bounds defining the symmetric interval with a 68% probability of containing the true value of the parameter.

Since we need only note the change in the likelihood to estimate the errors, it is not necessary actually to derive or perform the change of variables - however, implicitly, such a transformation is required to exist. To obtain any confidence limit, the limit must be expressed in terms of the corresponding number of standard deviations for a Gaussian distribution, N_σ. The appropriate limit in the parameter is found where the likelihood falls by $\Delta\mathscr{L} = {}^1/_2\, N_\sigma{}^2$. So to evaluate 90% confidence limits, corresponding to 1.28σ, the shift is $\Delta\mathscr{L} = 0.83$. Further discussion of non-parabolic likelihoods is found in chapter 9 of reference [35].

4.4 The Effect of Finite Monte-Carlo Statistics

In the first section, it was assumed that we knew the pdf f(x|a) exactly. In practice, f(x|a) is often non-parametric[14] and must be generated by a Monte-Carlo, with finite statistics. This has two consequences:

i. The Monte-Carlo data must be binned, leading to a loss of resolution.

ii. The finite statistics mean that f(x|a) is not precisely determined, but has statistical fluctuations.

One way to overcome these problems is to use explicit non-parametric methods, instead of likelihood methods, as advocated in reference [36]. Here, we consider the second point, since it leads to additional fluctuations of the central estimate, which are not accounted for in the error estimate derived from the curvature of the likelihood.

If we generate a Monte-Carlo distribution $f_m(x|a)$ which is an approximation to the distribution f(x|a), and the data is described by a distribution $f_d(x)$, then we consider fluctuations in both f_d and f_m. The likelihood which we use is

$$\mathcal{L} = N_d \int dx\, f_d \log f_m \tag{4.18}$$

$$\Rightarrow \qquad \delta\mathcal{L} = N_d \int dx \{ \delta f_d \log f(x|a) + f(x|\alpha)/f(x|a)\, \delta f_m \} \tag{4.19}$$

The important term is $d\mathcal{L}/da$, since this leads to the estimates of the statistics. Differentiating (4.19), we find:

$$d\delta\mathcal{L}/da = N_d \int dx \{ \delta f_d/f(x|a)\, \partial f/\partial a - f(x|\alpha)/f(x|a)^2\, \partial f/\partial a\, \delta f_m + f(x|\alpha)/f(x|a)\, \partial(\delta f_m)/\partial a \} \tag{4.20}$$

When this expression is evaluated at $a = \alpha$, the last term vanishes and we are left with

$$d\delta\mathcal{L}/da = N_d \int dx\, (\delta f_d - \delta f_m)/f\, \partial f/\partial a \tag{4.21}$$

---

[14] i.e. cannot be expressed in terms of simple functions

Comparing this equation with the expression for the variation of $d\mathcal{L}/da$ in (4.12), we see that δf is replaced by $(\delta f_d - \delta f_m)$. The fluctuations $\delta f_{d,m}$ result in statistical variations proportional to $1/\sqrt{N_{d,m}}$, and these combine in quadrature, so that the error should behave like $1/\sqrt{N_{eff}}$ rather than $1/\sqrt{N_d}$, where

$$1/\sqrt{N_{eff}} = 1/\sqrt{N_d} \oplus 1/\sqrt{N_m} = \sqrt{R} \times 1/\sqrt{N_d} \text{ where } R = 1 + N_d/N_m \qquad (4.22)$$

We use $\oplus$ to denote addition in quadrature. We see that the error derived from the curvature of the likelihood is increased by $\sqrt{R}$ to allow for the statistical errors on the Monte-Carlo pdf. A more natural way of incorporating this term is to reduce the likelihood by R itself, since the variance is inversely proportional to the (second derivative of the) likelihood.

4.5 Setting Confidence Limits in the presence of Poisson Processes

Likelihood methods work well when used to estimate parameters from distributions where the parameters do not explicitly or implicitly relate to Poisson variables, for example the estimation of the W mass from the transverse mass distribution. However, some care is required when the parameters do relate to Poisson variables, for example the mass of some new particles deduced from the excess of events in some kinematic region.

While, in the latter case, the likelihood can be formed in a manner precisely as in (4.1), it is important to recognise the distinction between the two problems. When we have a single class of events (for example, every event is a $W \rightarrow \mu\nu$ decay) and we use a set of measurements $\{x_i;\ i = 1,N\}$ to estimate a parameter a, then every measurement has 'knowledge' of a, and it is meaningful to write the pdf as f(x|a). However, where there are two classes of events - background and signal - and only the distribution of signal events and their absolute rate depend on the unknown parameter a, while the background events have no 'knowledge' of a, then not all measurements of x have 'knowledge' of a. The pdf can be written as f(x|a), but it is also important to identify this as $f(x)_{back} + f(x|a)_{sig}$.

In cases where backgrounds and numbers of events are low, and it is possible to identify a kinematic region where one is sensitive to a potential signal, while being fairly insensitive to the cuts, then one can use more explicit Poisson (or binomial) methods. One such method is described in an appendix of reference [37]. However, in situations where:

1. there is considerable background and no readily identified region to search for a signal;
2. results would be very sensitive to cuts made to isolate some kinematic region;
3. the shapes as well as the number of events depend on the parameter to be investigated, and it is not possible to express the problem simply in terms of 'numbers of events' in a conventional Poisson formulation;

then it is worthwhile to exploit the full power of the likelihood method and to use continuous density functions. Poisson distributions are no more than a limit of binomial distributions, which in turn are a special case of the multinomial distribution. The likelihood expressed in (4.1) is no more than the logarithm of the multinomial probability in the continuum limit.

It is useful to examine the method of likelihoods from a probabilistic view point. Ideally, we have a set of measurements $X = \{x_i\}$, and wish to infer the probability distribution of some unknown parameter a - this distribution is p(a|X). Usually, we know the distribution expected for X for a given a - this is p(X|a). Using Bayes theorem we can write:

$$p(a|X) = p(X|a)p(a)/p(X) = p(X|a)p(a) \div \int da\, p(X|a)p(a) \qquad (4.23)$$

Unfortunately, the 'prior distribution', p(a), is not usually known, and frequently one assumes that it is uniform in the physical region. This results in the 'likelihood', defined as:

$$L(a) \equiv p(a|X) = p(X|a) \div \int da\, p(X|a) \qquad (4.24)$$

Frequently, we take the logarithm, and the numerator becomes identical to (4.1). In estimating the most likely value of the parameter, the denominator in (4.24) is merely a normalisation. Further, the denominator has no significant effect in the derivation of the variance, or of confidence limits when the

distribution of some function of the parameter is Gaussian, and the likelihood peaks at a value far from any bounds on the range of a. However, in situations with implicit Poisson statistics, the formulation of the likelihood L(a) is more useful. The normalisation allows for the fact that the number of events expected is never negative, and leads to the same behaviour as the formulation of reference [37]. Since L(a) is the pdf for a, confidence intervals may be defined as desired, such that the bounded interval contains the appropriate integrated probability.

There are two major problems with this approach. Firstly, one has to assume some prior density. Secondly, implicit (but not at all apparent) in the probabilistic formulation is the assumption that the signal is potentially observable. This is unfortunate, since it means that the pdf for the parameter of interest is always normalised to unity, and one can always find confidence intervals. This is rigorously correct, although may it not be physically very sensible. It results in the possibility of setting limits in cases where:

i. there is no sensitivity to the signal, even though there may be plenty of signal events in the sample;
ii. there are too few events expected from the signal to make it possible to set a limit using simple Poisson arguments for the number of events expected.

In the second case, if one were to use Poisson statistics to find the number of events required to form a limit, it might turn out that it would never be possible to obtain this mean number of events, for physical values of the parameter a. However, by formulating the likelihood as a function of a, the existence of the model under investigation is imposed on the statistical analysis.

4.6 Final Remarks

The limits derived from a given set of data naturally depend on the events used, and hence are subject to statistical fluctuations. In some cases, the limits derived will be more optimistic than would be expected in the absence of statistical fluctuations. While this may be useful when comparing with a

set of limits derived under similar circumstances - as is the case with limits deduced from searches for anomalous single photons (see chapter 8) - when there are no comparable results, it may be more useful to quote the sensitivity[15] expected, in cases of optimistic fluctuations. This is the approach which has been adopted in the subsequent analysis.

To conclude, likelihood methods may not be perfect, but they do have many good features which were expounded at the start of this chapter. Further, most other statistical methods assume asymptotic behaviour for their validity and suffer from the same problems as likelihood methods, plus more serious problems. Parameters estimated with likelihood methods can generally be considered as being fairly robust. However, there is some uncertainty in the derivations of confidence limits, which is an inescapable feature of statistical problems. It is with these caveats that we will use the methods outlined in this chapter.

[15] We define 'sensitivity' as the limit which would be expected with an equivalent number of events, but in the absence of statistical fluctuations.

5. THEORETICAL BACKGROUND TO W/Z PHYSICS

5.1 A Brief History

The birth of the weak interaction occured in 1896 with Becquerel's discovery of radioactivity, and the subsequent observation of the emission of β rays (electrons) from some decaying nuclei. In 1914, Chadwick observed that the spectrum of these electrons was continuous. However, it was not until 1930 that Pauli [38] was able to explain this puzzle in terms of a new particle, the neutrino.

Soon afterwards, in 1934, Fermi [39] developed a quantitative theory of β decay along the lines of the theory of QED, pioneered by Dirac, Heisenberg and Pauli. In QED, the interaction of two charged particles can be envisaged as the exchange of a photon between two charged currents. The propagation of the photon is described by a 'propagator' which varies like q^{-2}, where q is the four-momentum transfer of the process. According to Fermi's theory, the weak interaction was, unlike the long range electromagnetic interaction, a four fermion interaction, where the propagator was proportional to the constant G (Fermi's constant).

After a suggestion by Lee and Yang [40] in 1957, experimental work by Wu [41] showed that the charged current weak interactions only involved 'left handed' ('right handed') fermion (antifermions) - where the particle spin is antiparallel (parallel) to the momentum vector.

However, the early models were far from satisfactory. They predicted that for neutrino-electron scattering, the cross-section would rise like s (the square of the centre of mass energy). This was undesirable, since this rise would violate the unitarity principle, which is derived from the conservation of probability. Since the interaction is point-like, it is all S-wave scattering, and unitarity imposes a bound, which falls like 1/s, on each partial-wave term. Therefore it was proposed to introduce exchange particles in analogy to the photons exchanged in QED; but, in the weak interaction, the exchange bosons were given a mass, m, in order to describe the low energy results. The propagator became $-Gm^2/(q^2-m^2)$. So now, at small q^2, the propagator behaves like G, agreeing with the observations. At large q^2, for the s-channel (i.e. $\bar{\nu}e$ scattering), the cross-section falls like s^{-1}, and unitarity is not violated; however, for the t-channel (i.e. νe scattering), the cross-section is constant, and

the partial-wave amplitudes rise logarithmically, eventually leading to the violation of unitarity at some very high energy. The violation of unitarity is even worse for $\nu\bar{\nu} \rightarrow W^+W^-$.

One method for introducing the exchange particles into a quantum field theoretical description is to invoke the gauge principle, which is discussed in the next section. The gauge symmetry requires a neutral exchange particle, and it can be shown that this controls the behaviour of the $\nu\bar{\nu}$ scattering. Further, 't Hooft [42] demonstrated that theories possessing gauge symmetry avoid uncontrollable divergences.

5.2 A Gauge Theory of the Electroweak Interaction

The theoretical ideas presented here are motivated in many textbooks [43], [44] by series of heuristic arguments which correspond to the historical developments. Instead, in this section and the next, we will try to summarise directly how the W and Z bosons fit into current theories and what predictions are made. We proceed by assembling the components of the Lagrangian describing the electroweak model of Weinberg and Salam.

The starting point is to construct a Lagrangian for the fermions. The particles are classified according to a new quantum number, weak isospin. This is analogous to isospin used in the description of hadronic processes. In the case of isospin, the proton and neutron are seen as manifestations of the two states of a 'nucleon', where the third component of isospin is $^{+1}/_2$ or $^{-1}/_2$ respectively. Similarly the neutrino and electron are seen as members of a weak isospin doublet, as are the up and down quarks. Further, each particle except the neutrino belongs in its own singlet. The particles in the doublets are in the left handed state (eigenstates of $1-\gamma_5$), while the particles in the singlets are in the right handed state (eigenstates of $1+\gamma_5$) (for the definition of the γ matrices and γ_5, see reference [44]). Ignoring the mass terms, and symbolically labelling the doublets and singlets as L and R respectively, the Lagrangian looks like:

$$\mathcal{L} \sim \bar{L}\gamma_\mu\partial^\mu L + \bar{R}\gamma_\mu\partial^\mu R \qquad (5.1)$$

The assignment of the third component of weak isospin (T_Z) within the isospin multiplets is arbitrary, and so the physics (and hence the Lagrangian) ought to be invariant to local transformations from one representation to another. This is the gauge principle. The particular class of transformations we wish to consider are those of SU(2). The second term of our Lagrangian (5.1) is a singlet and thus is trivially invariant. However the invariance of the first term can only be maintained by replacing the first derivative ∂^μ by the so called covariant derivative:

$$D^\mu \equiv \partial^\mu + {}^1/_2 ig\sigma_i W_i^\mu \tag{5.2}$$

where g is a coupling strength, $\{\sigma_i;\ i=1,3\}$ are the Pauli matrices (which are the generators of the SU(2) transformations), and there are three gauge fields $\{W_i;\ i=1,3\}$ - which are W^+, W^- and W^0 in an alternative basis. Under an SU(2) transformation, the gauge fields transform in such a way as to compensate for the operation of the derivative on the local transformation. In addition a kinetic energy term for the gauge fields can be added.

Further, we can consider the invariance of the matter fields under a local phase transformation - this is a special type of gauge transformation, under the group U(1), which is associated with the quantity weak hypercharge. This motivates the introduction of an additional single vector field, B, which interacts with both left and right handed particles, with a coupling g′. (U(1) invariance applied to the Lagrangian for a single charged fermion yields the electromagnetic interactions.)

At this point we note that the W^+, W^- interact with the left handed fermions, but not the right handed ones. It is tempting to identify these fields with the IVB's, however this is a little premature, since our Lagrangian contains no mass term like m^2W^2 for these particles. Unfortunately, an explicit mass term violates gauge invariance. Further, the B couples to the left handed neutrino and so cannot be considered as a candidate for the photon. The answers are to be found in the model of Glashow [1], Salam [2] and Weinberg [3] (GSW).

5.3 The Glashow-Salam-Weinberg Model

The first step to generating IVB masses is the Goldstone model [45]. To the Lagrangian constructed so far, we introduce terms describing an elementary complex scalar field, ϕ, which is a doublet of weak isospin (the field has four real components).

The Lagrangian for ϕ contains a potential term $-\mu^2\phi^\dagger\phi + \lambda(\phi^\dagger\phi)^2$, where μ^2 and λ are both positive. Considered classically, this potential has an unstable maximum at $\phi = 0$, and stable minima on the hypersurface $\phi^\dagger\phi = \mu^2/(2\lambda) \equiv v^2$. Although the Lagrangian shows rotational symmetry (in the space of the four component fields), the solution chosen by nature will be a unique point on the hypersurface. This causes the symmetry to be spontaneously broken, and the field acquires a non-zero vacuum expectation value (vev) at this point: $|<0|\phi|0>| = v$. Perturbation calculations are performed about this stable vacuum solution, and as a consequence, we are left with a real massive scalar (the Higgs boson) and, in accordance with Goldstone's theorem, three massless scalars.

The kinetic energy term for the scalar, $\partial_\mu\phi^\dagger\partial^\mu\phi$, is modified by the requirement of gauge invariance, which leads to the Higgs model [46]. Again the derivative is replaced by the covariant derivative: $\partial \rightarrow D$. This leads to an expression like:

$$\partial\phi^\dagger\partial\phi \rightarrow D\phi^\dagger D\phi \sim \partial\phi^\dagger\partial\phi + 2gW\,\mathrm{Im}(\phi^\dagger\partial\phi) + g^2WW\phi^\dagger\phi \qquad (5.3)$$

The important term is the third one. Since we expand ϕ about its non-vanishing vev, v, to first order it becomes $g^2v^2W^2$ - which looks like a mass term $m_W{}^2W^2$. Therefore the W particles obtain a mass of the order of gv. Thus we see the role played by the new scalar field is to provide the IVB masses. Further, this can be achieved only by a scalar, since, as the vev is in principle an observable, it should satisfy Poincaré invariance (space-time invariance). This is only possible for a spinless field. The presence of the second term like $W\partial\phi$ (the first ϕ is constant to first order) represents the interference between the Goldstone bosons and the gauge fields. This interaction (indicative that our fields are not the normal modes of the Lagrangian) is trivially removed by a gauge transformation. This is fortuitous since i) it removes the unobserved massless particles, and ii) it removes three degrees of freedom which have manifested themselves as the longitudinal polarisation of the three massive gauge fields.

So far, the role of the U(1) gauge field has been neglected. It too interacts with the scalar field and, in addition, mixes with the neutral W^0. With an appropriate choice for the location of the vev of the ϕ field on the hypersurface, W^0 and B mix in such a way that there emerge particles corresponding to the normal modes: one which is massless, identified as the photon, and a second massive particle, identified as the Z boson. The observation of neutral currents in 1973 in the Gargamelle bubble chamber [47] provided the first confirmation of the GSW theory. A key ingredient of the theory was the proof by 't Hooft in 1971 that such gauge theories were indeed renormalisable.[16]

We note that, in addition, the Higgs mechanism may be used to generate the fermion masses in a gauge invariant way. Unfortunately, this requires the introduction of one new parameter (the coupling to the Higgs field) for each fermion type - and so provides no constraints on the fermion masses.

The physical fields, the photon and Z, are identified as rotations of the gauge fields, B and W^0, through an angle θ_W. This is the key parameter of the model. The principal predictions of the model, in addition to the above, are:

i. the Higgs mass: $m_H = \sqrt{(2\lambda)}v$

ii. the IVB masses: $m_W = {}^1/_2 gv$ and $m_Z = {}^1/_2\sqrt{(g^2+g'^2)}v$

iii. the couplings: $g = e/\sin\theta_W$ and $g' = e/\cos\theta_W$

The first is of no use since λ is unknown. Eliminating v from ii) and substituting from iii) gives:

$$m_W/m_Z = \cos\theta_W \tag{5.4}$$

The constant g relates to the couplings of the charged current, and this can be measured as the Fermi constant, G. At the tree level, this is given by:

$$G = \sqrt{2}\, g^2/(8m_W^2) = \sqrt{2}\, e^2/(8m_W^2 \sin^2\theta_W) \tag{5.5}$$

Finally, the Z couples to matter with an effective current

---

[16] Calculations in perturbation theory inevitably lead to divergences which must be controlled by the introduction of additional terms. A theory is renormalisable if measurable quantities can be calculated without the need to introduce new parameters at each level of perturbation.

$$J(Z) = J_3 - \sin^2\theta_W J(em) \qquad (5.6)$$

where the current J_3 is associated with the third component of isospin. By measuring the form of the neutral current interactions, $\sin^2\theta_W$ can be determined.

5.4 W/Z Phenomenology

Much of the phenomenology of the W and Z bosons is well known and discussed in the literature, for example [48]. Here, we consider some of the features of relevance to later discussions.

5.4.1 Production Mechanism

The W couples to the left handed doublet $(u,d)_L$ and thus can be produced in high energy collisions of protons with antiprotons:

$$u\,\bar{d} \rightarrow W^+ \text{ and } d\,\bar{u} \rightarrow W^-$$

The Z couples to the doublet and the singlets u_R and d_R:

$$u\,\bar{u} \rightarrow Z \text{ and } d\,\bar{d} \rightarrow Z$$

At collider energies, the principal contribution to W and Z production comes from the fusion of valence quarks, while the sea contribution[17] is between 2 and 4%. Also, there is a contribution - about 6% - from the Compton process:

$$q\,g \rightarrow q'\,W \text{ or } q\,g \rightarrow q\,Z$$

The lowest order process is where two quarks collide, the so called two-to-two process[18] (analogous to simple Drell-Yan production), and the p_t of the IVB results from the small intrinsic motions of the colliding quarks. The main process leading to IVB's with a significant p_t is the first

[17] evaluated with the ISAJET Monte-Carlo using several parameterisations for the structure functions

[18] there being two incoming quarks, and two leptons from the subsequent decay of the IVB

order process (in α_s) in which one of the colliding quarks radiates an external bremsstrahlung gluon, the so called two-to-three process [49]. The Compton process, which is first order in α_s, inevitably gives rise to an IVB with a non-zero p_t. The longitudinal motion of the IVB arises from the difference in momenta of the colliding quarks.

5.4.2 Decay Process

Once formed, the W and Z can decay to left handed lepton pairs, and left and right handed lepton pairs respectively. Because of the left handed couplings of the W to the quarks, the quarks (antiquarks) forming the W are polarised with their spins aligned antiparallel (parallel) to their momentum vectors, as illustrated in figure 18. The decay leptons (electron and neutrino, or whatever) are similarly polarised. Therefore the decay can be described by an initial state with $J=1$, $J_Z=1$ and a final state also with $J=1$, $J_Z=1$, rotated by an angle θ^* (in the rest frame of the W). (Note that the angle is measured between the momentum vectors of the antiproton and positron or proton and electron. Alternatively, the charge may be explicitly included.) The amplitude for this decay is proportional to the rotation matrix

$$d_1{}^1{}_1(\theta^*) = {}^1/_2(1+\cos\theta^*) \tag{5.7}$$

Therefore, the decay of W's produced in valence quark interactions will show a significant asymmetry in the (charged) angular distribution of the decay leptons in the W rest frame (the V−A distribution):

$$d\sigma/d\Omega \propto (1+\cos\theta^*)^2 \tag{5.8}$$

The Z, since it couples to the right handed fermions with almost the same strength as the left handed couplings, has a decay angular distribution which is almost symmetric (and, in fact, if $\sin^2\theta_W$ were ${}^1/_4$, it would be symmetric).

The p_t distribution of the leptons is readily calculated if we ignore the p_t of the W or Z.

$$d\sigma/dp_t = d\sigma/d\Omega \div dp_t/d\Omega \tag{5.9}$$

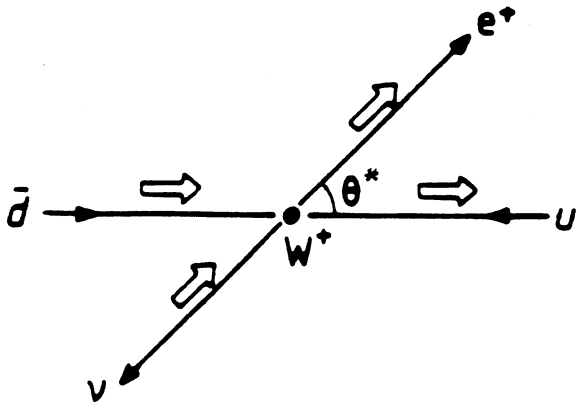

Figure 18: The Angular Distribution in W Decay

Since $p_t = p_0 \sin\theta^*$, where p_0 is the momentum of the lepton in the rest frame of the IVB ($m_W/2$ or $m_Z/2$), and $d\Omega = 2\pi\, d\cos\theta^*$

$$dp_t/d\Omega \propto \cot\theta^* = \sqrt{(p_0^2 - p_t^2)} / p_t \tag{5.10}$$

$dp_t/d\Omega$ has a zero at p_0, and so $d\sigma/dp_t$ has a singularity at p_0, falling to zero beyond this. This is the so called Jacobian peak. This distribution is useful for the W's since we are able to reconstruct only the transverse energy of the neutrinos, whereas for the Z's, the mass can be reconstructed from the di-lepton 4-momenta. In practice we use the transverse mass, which is defined by

$$m_t^2 = 2p_t \not{E}_t(1 - \cos\Delta\phi) \tag{5.11}$$

where $\not{E}_t$ is the transverse energy of the neutrino, and $\Delta\phi$ is the angle between the lepton and the neutrino in the transverse plane. Where the p_t of the W is zero, the transverse mass reduces to $2p_t$. To first order, the expression (5.11) for the transverse mass is invariant to transverse boosts to the system arising from the p_t of the W; and by using the transverse quantity, the sensitivity to the longitudinal motion of the system is removed. In practice the finite width of the W smears p_0, so that the m_t distribution has a rapid fall to zero in the region of $m_W \pm \Gamma_W$. Of course, experimental resolution further smears the distribution.

6. ESTIMATING THE MASS OF THE W FROM THE MUONIC DECAY

6.1 Data Selection

The detection of events is described in chapter 1. During the runs of 1984 and 1985, of the order of 10^7 events were written to tape. Of these, roughly 40% contained muon triggers. The details of the data reduction are slightly different for the two data sets, but the cuts are essentially the same. The data reduction for 1985 is described below; that for 1984 was similar. The aim was to select candidate events for the decay $W \rightarrow \mu\nu$ with a low background. The background was reduced by cuts on the kinematic variables and quality cuts to select events with well measured parameters consistent with the decay $W \rightarrow \mu\nu$.

An initial selection was made of the good muon candidates with $p_t > 4.5$ GeV/c. This led to 22×10^3 events. This cut was then tightened to a p_t cut of 10 GeV/c, giving 1764 events. Finally the cut was raised to its final value of 15 GeV/c and the following cuts were made to improve the muon quality:

1. Basic CD quality cuts:
    a. average matching χ^2 between the CD and the muon chambers < 15 (2 degrees of freedom);
    b. CD track length in bending plane > 40 cm, with ≥ 30 points on the track;
    c. Sadoulet $\chi^2 < 3$ and the χ^2 per degree of freedom for the z coordinate < 9 (see chapter 3).
2. Cosmic rays identified by software were removed.
3. π and K decays identified by software were removed.
4. Events where the muon candidates were identified as passing through gaps in the calorimeter were rejected.

These cuts ensured a reasonable quality of the muon candidates, leading to 411 events. Further cuts were made to select W candidates:

5. We required the missing energy > 15 GeV.

6. It is expected that leptons from W decays should not be strongly correlated with other particles, and in particular jets. Therefore the following isolation criteria were required:
    a. in a cone of $\Delta R \equiv \sqrt{(\Delta\eta^2 + \Delta\phi^2)}$ (see chapter 2) of 0.4 around the muon, the net transverse energy seen in the calorimetry, ΣE_t, < 3 GeV; while the net transverse momentum of charged tracks seen in the CD, Σp_t, < 1 GeV/c;
    b. no calorimeter jet, E_t > 10 GeV, within a cone of ΔR of 0.7 around the muon;
    c. within 30° back to back with the muon in the transverse plane, no CD jet with p_t > 5 GeV/c and no calorimeter jet with E_t > 10 GeV.

This led to 97 events, which were then scanned on the Megatek. Of these, there were:

- 1 $Z \rightarrow \mu\mu$,
- 1 cosmic ray,
- 2 clear double interactions which have total reconstructed energy in the calorimetry > 630 GeV and two reconstructed vertices - double interactions are usually not used due to the increased problems of reconstruction in the CD,
- 43 events considered to have CD tracks incompatible with high momentum muons, being either π/K decay candidates or tracks suffering from reconstruction problems,
- 50 good candidates.

Finally, further cuts were made to reduce the decay background and facilitate the acceptance calculations:

7. We required that the matching between CD and muon chamber tracks in each of the two spatial coordinates and each of the two angular coordinates should be < 4 standard deviations.
8. Each event was required to have a muon trigger.
9. Suspected double interactions were removed by a requirement that the total energy reconstructed in the calorimetry should be less than 480 GeV.

10. Following the application of the automatic CD Fixup (see chapter 3), the events were passed through all the quality cuts again.
11. A final scan was made to remove all dubious CD tracks.

This gave a final data set containing 34 events for the cross-section calculations. A similar procedure was applied to the 1984 data, yielding 23 events.

6.2 Backgrounds and Cross-section

Using ISAJET, it is anticipated that the background from $W \rightarrow \tau\nu$ with $\tau \rightarrow \mu\nu\nu$ is of the order of 4 or 5%. In addition there are decays of longer lived mesons, namely pions and kaons. If a fast meson decays before the calorimeter ($c\tau$ is 8 and 4 metres, respectively), sometimes the meson and daughter muon are reconstructed as a single track. The combined track can sometimes be recognised by the change of curvature and the poorer CD-muon chamber matching. In addition, there is background from tracks which have been distorted by systematic effects in the CD, and subsequently reconstructed with high momentum. The background from these two sources is greatly reduced by the strict quality cuts in the CD and in the matching to the muon chambers. It is estimated that the background is less than one event.

The acceptance of the trigger (39% at the first level, and 94% at the final level) and the efficiency of the software cuts have been evaluated as 15 ± 1%. The integrated luminosity collected over the two running periods was 551 nb^{-1}. This leads to a measurement of the cross-section times branching ratio of 0.66 ± 0.12 ± 0.14 nb at $\sqrt{s}$ = 630 GeV. This work is discussed in greater detail in [50], [51]. The cross-section is in good agreement with the UA1 electron result, which is 0.63 ± 0.04 ± 0.10 nb [55].

To improve the quality of the events used for the mass fitting, all events which showed any evidence of distortions of the CD track were removed by software. This left 46 events for the mass fitting. To improve the determination of the momentum of the muon tracks, the OMF procedure was applied, as described in chapter 3.

6.3 Methods for Obtaining the W Mass

To estimate the W mass for the $W \rightarrow \mu\nu$ events, the transverse mass (see chapter 5 for definition) distribution was compared with Monte-Carlo expectations using a likelihood method (see chapter 4).

Monte-Carlo transverse mass distributions were generated for a series of different W masses. For each mass, m, the log likelihood[19] was found. If the probability density function (pdf) for M_t is $f(M_t|m)$, then the likelihood is defined as

$$\mathcal{L}(m) = -\Sigma \log f(M_t(i)|m) \tag{6.1}$$

where the sum is over the events i = 1 to N.

In practice, it is more convenient to use the inverse transverse mass distribution, M_t^{-1} (it is shown in chapter 4 that the likelihood result is invariant to a change of variable). This is useful, since the muon momentum, which is directly reflected in M_t, is measured in the CD, and the measurement is Gaussian in 1/p (rather than p) to a good approximation. Thus it is more natural to use quantities related to 1/p. In addition, because the smearing (in 1/p) of high energy muons can give rise to very high estimates of the momentum, it is difficult to establish a reliable shape for the pdf at large M_t.

There was some uncertainty as to the parameterisation of the CD errors on the momentum. The momentum has two components of error: a statistical error (σ_{sta}) due to the scatter of the digitisings, and a systematic component (σ_{sys}) of unknown origin. The systematic error was seen in studies with cosmic rays, by looking at the reconstructed momenta of the two halves of the cosmic track. It is systematic in any given region of the CD; however, it varies irregularly between different regions. There is some small overlap between the two types of error, and the total error on a measurement of 1/p is defined as

$$\sigma_{tot} = \sqrt{\{(0.83\sigma_{sta})^2 + (\sigma_{sys})^2\}} \tag{6.2}$$

---

[19] often the word 'log' will be left implicit

However, it is not obvious that this is the most appropriate parameterisation of the total statistical error to use for $p\bar{p}$ data. Thus, in order to understand the nature of this error, we have made (6.2) more general, and we parameterise the total statistical error as

$$\sigma(\varepsilon) = \sqrt{\{(0.83\sigma_{sta})^2 + (\varepsilon \times \sigma_{sys})^2\}} \tag{6.3}$$

where ε is an unknown which can be estimated with the likelihood expressed as a function of m and ε: $\mathcal{L}(m,\varepsilon)$. The approximate behaviour of the pdf, $f(M_t|m,\varepsilon)$, is that m controls the centering of the M_t distribution, while ε feeds into the width.

6.3.1 Generating the M_t Distribution

It is necessary to have access to Monte-Carlo distributions of M_t for different values of m and ε. For maximum efficiency, it is desirable to have a fast Monte-Carlo generator within the mass fitting program. While it is desirable that such a generator should provide a reasonable description of the M_t distribution, it is not essential, as the method can be calibrated using a more detailed Monte-Carlo, such as ISAJET with UA1 detector simulation. To perform this calibration, Monte-Carlo events were selected in precisely the same way as the real events. The selection was made from the inclusive W production, described in appendix F.

The principal features of this internal Monte-Carlo used to generate W's are the same as those of the generator described in detail in chapter 9. W's are generated using theoretical parameterisations of the longitudinal and transverse momentum, and are decayed according to the V−A distribution. The reciprocal momentum of the muon is then smeared with the error $\sigma(\varepsilon)$ (defined above), where the values of σ_{sta} and σ_{sys} are taken from the data event which is nearest in $\cos\theta$ and ϕ. The simulated neutrino is smeared according to the resolution. This resolution is a function of the scalar sum of the transverse energy, although for simplicity, we have evaluated it at a value typical for W events, namely $\Sigma|E_t| = 80$ GeV. The simulated muon is then extrapolated rectilinearly to the muon chambers, and the probability for firing the muon trigger is evaluated from look-up tables. Finally, the inverse transverse mass is calculated from the smeared momenta.

6.4 Systematic Errors and Calibration

There are two important points to establish:

1. Is the muon momentum being correctly estimated ?
2. Given a good measurement of momentum, is this being used to make an unbiassed estimate of the W mass ?

6.4.1 Systematics on the Momentum Determination

There are two basic stages with the estimation of momentum.

i. Digitisings have to be obtained from the raw data.

ii. The muon momentum has to be estimated from the track curvature.

The algorithm used to perform the second task was explicitly tested. Digitisings were generated which lay exactly on a circle, and from these the corresponding momentum was estimated. For tracks with momenta around 50 GeV/c, it was found that the mismeasurement of the momenta was less than 0.1 GeV/c. Therefore, it was concluded that there were no serious systematics in the reconstruction, and the precision was not a problem. This allowed us to use the reconstructed momentum as an unbiassed tool with which to investigate possible systematics in the formation of the digitisings for real data.

The original studies performed on the CD momentum estimation using cosmic rays were insensitive to global systematics which tend to move the momenta of all tracks in the same direction. (These cosmic ray tests were sensitive to systematics in the variable Q/p, since the two halves of a cosmic ray curve in the opposite sense with respect to the nominal event vertex in the median plane, and so it appears that they have the opposite charge.) Generally, it is not necessary to provide absolute calibrations of multi-wire drift chambers since the calibration coefficients can be determined from internal consistency, unlike in the case of a calorimeter. The only parameter which must be measured

is the magnetic field, and the accuracy with which the J/psi mass is reconstructed [52] in the CD means that the field is measured to better than $^1/_2$%.[20] However, due to the ease with which problems can manifest themselves as systematic effects on the measurement of the sagitta, even for simulated data (see below), it was considered desirable to obtain some check on the absolute calibration. Using electron tracks in $W \rightarrow e\nu$ events, the calorimetric energy was compared with the CD momentum. Explicitly, the quantity

$$\Delta \equiv [p^{-1} - E^{-1}] \div \sqrt{[\sigma(p^{-1})^2 + \sigma(E^{-1})^2]} \tag{6.4}$$

was compared with Monte-Carlo predictions, allowing for the bremsstrahlung spectrum of the electrons. The expression of equation (6.4) is a better approximation to a normal variable than $[p - E] \div \sqrt{[\sigma(p)^2 + \sigma(E)^2]}$. With and without some of the muon cuts (to give the tracks the same topology as the muon tracks), it was found that the agreement between the calorimetric and CD measurements was very good (see figure 19). Therefore, the limit on global systematics for the CD is of the same order as that of the electromagnetic calorimeter, namely 3%.

---

[20] Although the J/psi mass can be used as a check on the magnetic field, it cannot provide useful limits on the sagitta errors because of the low momenta of the tracks.

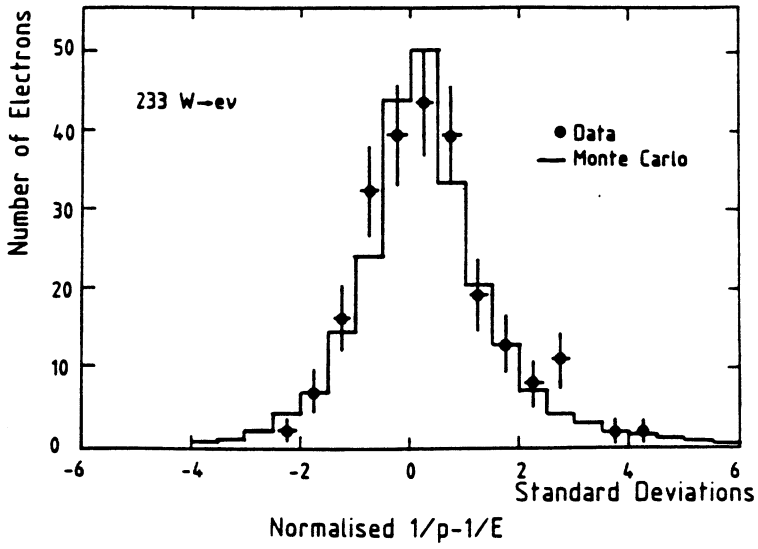

Figure 19: Comparison of CD Momentum (p) and Calorimetric Energy (E)

6.4.2 Systematic Errors on the Method

The internal consistency of the mass fitting program was tested directly. Event parameters were generated with the internal Monte-Carlo and fed into the program. In all cases, the input mass was recovered. It was anticipated that systematic shifts arising from imperfections in the internal Monte-Carlo could be removed by calibrating the procedure with ISAJET events.

Before applying the mass fitting procedure to simulated $W \rightarrow \mu\nu$ events, the Z mass fitting was tested with simulated $Z \rightarrow \mu\mu$ events (see chapter 7). It was found that there was a significant offset of the fitted mass from the input mass - the former was 4 GeV/c^2 larger. While it is desirable to allow for genuine offsets coming from any bias of the program, it is important to avoid problems which are a feature of the simulation alone. In this case, the discrepancy was found to be due to a systematic overestimation of the CD momentum of the simulated muons. The origin of this was the simulation of digitisings in the CD. The algorithm used to simulate the location of the digitisings was stepping from one CD wire to the next, however, the approximations used were not sufficiently accurate at high momentum, and there was a systematic loss of precision which increased along the track. Further,

there were severe discontinuities which occurred at the boundaries between wire planes. It should be emphasised that these systematics are of the order of 10^{-3} $GeV^{-1}c$, which should be compared to a typical statistical error, which is of the order of 10^{-2} $GeV^{-1}c$. These effects were extensively studied using a dedicated single track Monte-Carlo generator, and in reference [53] an improved algorithm was proposed, although it was not implemented for this analysis.

In order to be able to calibrate the W mass fitting, without introducing erroneous shifts, ISAJET events passing the selection were used, but their momenta were adjusted. The generated reciprocal momentum for each muon CD track was smeared by the total error (equation (6.3) with $\epsilon = 1$), and this value of momentum was used rather than the reconstructed quantity. This caused the low transverse mass tail to be a extended a little; however, precisely the same procedure was used for the internal Monte-Carlo, when applied to ISAJET events.

6.5 Results

6.5.1 Results for Data

It is found that the internal Monte-Carlo provides a good description of the data with $\epsilon = 1$ (see figure 20). The likelihood, $\mathcal{L}(m)$, attained its maximum at a mass of 78.2 GeV/c^2, with a fit probability (evaluated from the chi-squared) of 98%. The statistical errors evaluated from the likelihood are $+6.0$ and -5.3 GeV/c^2. Allowing the error coefficient (ϵ) to vary leads to a mass estimate of 78.2 GeV/c^2, with $\epsilon = 0.97 \pm 0.24$. These values are before corrections.

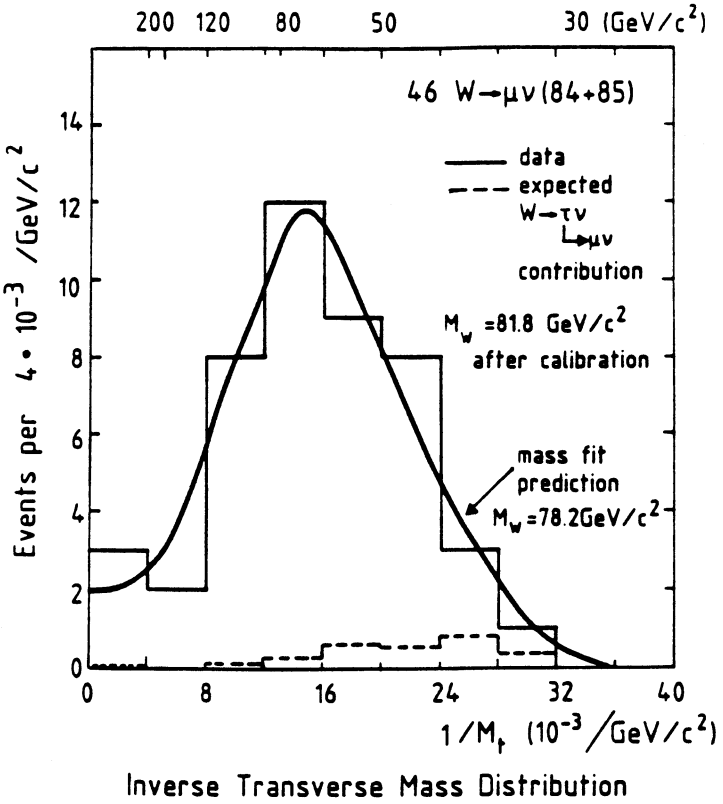

Figure 20: Inverse Transverse Mass Distribution for the Data

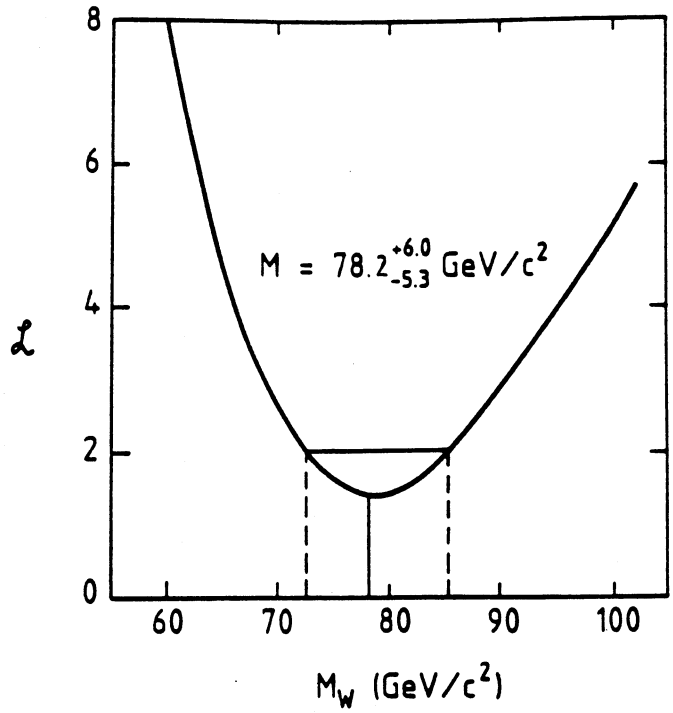

Figure 21: Likelihood for Data

The breakdown of the results for 1984/1985 and the effect of OMF in 1985 is shown in table 10. OMF has not succeeded in significantly reducing the errors, and the Iarocci chamber information has not added to the precision. These results are a little disappointing in view of the conclusions of chapter 3, where it was shown that OMF can produce a significant reduction in the error on the momentum. Several comments can be made which may offer some explanation for this. Firstly, the OMF procedure is statistical: so even though the error is reduced on an event by event basis, the momentum estimate will not necessarily be closer to the true value for every event (however, on average, one expects that the estimate will be an improvement). Secondly, the statistical errors on the individual event parameters are only one contribution to the statistical error deduced on the W mass estimate. There is a second significant contribution: this comes from spread of the unsmeared M_t^{-1} distribution. Thirdly, the requirement that the extrapolated CD track should match the muon chamber track is quite strict, and tends to introduce some correlations between the two parts of the muon track. While

the estimated error on the momentum may be reduced, since the implicit correlations are not allowed for, the true uncertainty on the momentum may be a little larger than the error would suggest.

Table 10: Breakdown of W Masses Before Corrections

1984	81.7	±9.2
1985	75.4	±8.0
All	78.2	±5.9
1985		
CD only	69.3	±7.9
OMF (without Iarocci's)	74.2	±7.6
OMF (with Iarocci's)	75.4	±8.0

To test our understanding of the event sample, we studied the W^+ and W^- candidates separately. The number of events and masses for the two charges are shown in table 11. In the table, results are given for no additional cuts, and with a cut to remove events whose momenta are within 2σ from infinity ($p^{-1} < 2\sigma$). From the table, two things are apparent: firstly, the mass reconstructed for the W^+ candidates is higher than that of the W^- candidates. Secondly, we have more W^+ candidates than W^-. It is important to ask whether either of these observations is indicative of systematic problems. On further study, we find that these effects do not seem to be related to OMF, the cuts applied or the later stages of the CD reconstruction - Monte-Carlo data shows no charge asymmetry. We have looked at the $W \rightarrow e\nu$ candidates, imposing the muon chamber geometry and our CD quality cuts. The electron events show no significant asymmetry in the p_t distributions for W^+ and W^-, although there is a large asymmetry in the number of events of different charges. For the 98 electron events passing our muon-type cuts, 37 are positive and 61 are negative - an asymmetry which is in the opposite sense to the asymmetry in the muon channel. One might anticipate systematics in the CD for the quantity charge/momentum, however, it is not clear that these could explain these observations consistently. If there were a shift in charge/momentum so that some W^- events were measured as being positive, then we would expect the mass for the W^- events to be higher - this is not the case. Of course, there may be some more complicated explanation.

Table 11: Masses for W^+ and W^- Events Before Corrections

	no cut			2σ cut		
	events	masses		events	masses	
W^+	27	85.2	±8.9	16	73.0	±7.6
W^-	19	65.7	±10.1	15	68.6	±8.6

To conclude, although the differences between W^+ and W^- are curious, they are not inconsistent with statistical fluctuations. Further, we are unable to identify a systematic effect which could account for these differences.

6.5.2 Results for ISAJET

Using four similar ISAJET samples, we obtain the masses shown in table 12, with the corresponding fit probabilities. The value of the W mass used by ISAJET is 83.4 GeV/c^2. The four individual samples have a mean of 79.6 GeV/c^2, with an error estimated from the spread of ±0.34 GeV/c^2. Using the combined samples, we estimate a correction of +3.6 ±1.1 GeV/c^2, where we believe that the shift is due to biases contained solely in the mass fitting program.

Table 12: Masses from ISAJET Samples

sample	events	mass		probability
1	390	79.2	±2.2	6%
2	411	79.6	±2.2	53%
3	387	79.8	±2.3	11%
4	387	80.0	±2.3	49%
Combined	1587	79.8	±1.1	7%

The combined sample does not correspond identically to the four individual samples due to the random manner in which muon trigger decisions are made for Monte-Carlo events.

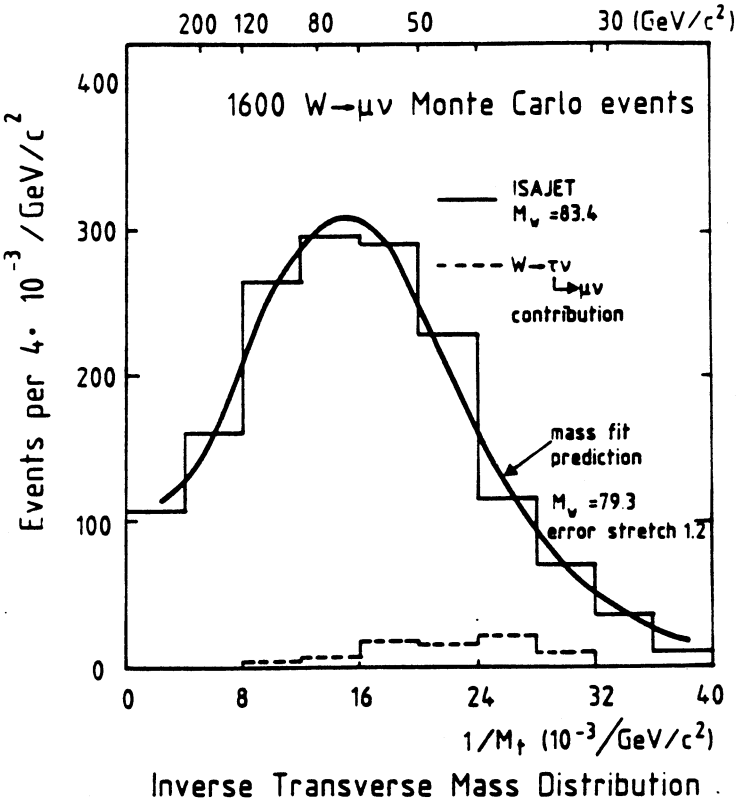

Figure 22: Inverse Transverse Mass Distribution for ISAJET

If we allow ε to vary for the ISAJET data, we obtain 79.3 $\pm$1.2 GeV/c^2 with ε = 1.18 $\pm$0.05, with a fit probability of 44%. A certain amount of care is needed in interpreting the effect of varying ε. The ISAJET events are smeared corresponding to $\varepsilon = 1$. The fact that we do not recover $\varepsilon = 1$ possibly indicates that the distributions generated by the internal MC are too narrow and that some additional smearing is required to make up the width of the M_t distribution. So although the total errors ($\varepsilon = 1$) seem to describe the data, it may be the result of a balance between the smearing and the description of the W production/decay. It should be noted, however, that the motivation for the 'total' errors comes from cosmic rays, and may not be totally appropriate to describe real data. We conclude that, although we now have a far better understanding of the nature of ε, there remains some small uncertainty, which we estimate corresponds to an error of $\pm$0.5 GeV/c^2 on the W mass.

6.5.3 Results for the Corrected Data

We use the ISAJET result, with $\varepsilon = 1$ (as is favoured by the data), as an indication that there is a calibration shift in the method used for the mass fitting . This shift is 3.6 GeV/c^2, with an error of ± 1.1 due to the statistics of the Monte-Carlo, and ± 0.5 due to a residual uncertainty in the nature of the smearing. This leads to a mass of 81.8 GeV/c^2. The statistical errors are obtained from the likelihood curve, and the asymmetric errors are $+6.0$, -5.3 GeV/c^2. The systematic errors are those from the calibration, with a 3% error included to cover scale systematics in the CD. It is found that the effect of systematics on the calorimetry tend to cancel out giving a negligible net effect.

6.6 Conclusions on the W Mass

Using a sample of the current UA1 $W \rightarrow \mu\nu$ candidates, we have obtained an estimate of the W mass:

$$81.8 \; +6.0, -5.3(\text{stat}) \pm 2.6(\text{syst}) \text{ GeV}/c^2.$$

This result is to be compared with our result of 82.7 $\pm$ 1.0 $\pm$ 2.7 GeV/c^2 from the electron channel [55]. Also, it is in good agreement with the results from the UA2 Collaboration of 80.2 $\pm$ 0.6 $\pm$ 0.5(sys_1) $\pm$ 1.3(sys_2) GeV/c^2 (the first systematic comes from uncertainty in the evaluation of p_t^{ν}; the second is from the uncertainty in the absolute energy scale calibration of the calorimetry) [56].

7. ESTIMATING THE MASS OF THE Z FROM THE MUONIC DECAY

7.1 Data Selection and Cross-Section

The starting point for the $Z \rightarrow \mu^+\mu^-$ search was the initial selection used for the W search. Events were considered if they had a muon trigger: either a single muon trigger or a di-muon trigger. The latter was not a subset of the former due to the larger area covered by the di-muon trigger. We required that there should be a muon candidate with $p_t > 15$ GeV/c, identified by the muon chambers. Further, we required that there should be a second muon candidate with $p_t > 10$ GeV/c, which was seen in the CD and had a deposit in the calorimeters compatible with a minimum ionising particle. However, this second muon was not required to have a track in the muon chambers provided that it lay outside the acceptance of the chambers. In addition, the following software cuts were applied (in 1985):

1. Basic quality cuts were applied to the first muon candidate (precisely as for the W selection):
    a. average matching χ^2 between the CD and the muon chambers < 15 (2 degrees of freedom);
    b. CD track length in bending plane > 40 cm, with ≥ 30 points on the track;
    c. Sadoulet $\chi^2 < 3$ and the χ^2 per degree of freedom for the z coordinate < 9.
2. Looser cuts were applied to the second muon candidate:
    a. CD track length in bending plane > 30 cm, with ≥ 25 points on the track;
    b. Sadoulet $\chi^2 < 6$ and the χ^2 per degree of freedom for the z coordinate < 9.
3. Finally a mass cut of 40 GeV/c^2 was applied to the di-muon pair.

A similar procedure was followed in 1983 and 1984. In 1985, 21 events passed the above cuts. These events were then scanned on the Megatek. It was found that:

- 2 of the events were cosmic rays,
- 10 events had a second track belonging to a clear jet,

- 1 event had a track distorted in the CD by the proximity of another track. After hand fixup, the muon candidates were found to have the same sign, and a mass of 15 GeV/c^2. In addition there was considerable hadronic activity.
- 8 events were good $Z \rightarrow \mu^+\mu^-$ candidates.

An additional candidate was found in the data taken with reversed magnetic field (which was generally not used in UA1 analysis). A second event was recovered from the W selection. One of the muons in this event was not associated to the vertex due to a distortion of the track. This effect was removed by the fixup procedure; however, the event was not used for the cross-section calculations. This gave a total of ten candidates, while in 1983 and 1984, similar analysis yielded five[21] and six events respectively, giving a complete sample of 21 events. These events were then subjected to the OMF procedure.

As for the W's, detailed studies were made of the acceptance, and are discussed fully in [57], [58]. The acceptance for Z's is complicated by the overlapping trigger conditions and the multitude of active areas used by the muon fast trigger. For 1985, the total acceptance for the events firing the di-muon trigger was 19 ± 3%, and 23 ± 1% for those firing the single muon trigger. The effective integrated luminosities for 1984, 1985 running periods were 256 and 296 nb^{-1}, yielding estimates of the cross-section at $\sqrt{s}$ = 630 GeV of 66 ± 11 ±17 pb.

7.2 Methods for Obtaining the Z Mass

In principle, the best way to obtain an estimate of the Z mass is a likelihood method using the individual muon momenta and the recorded energy flow in the event. Although this method provides a natural way of incorporating energy balance (see later), it requires a multidimensional Monte-Carlo probability density function (pdf), and this is difficult to obtain reliably. Instead we make use of the fact that, unlike for the W events, for the Z candidates it is possible to form the mass on an event by event basis. The methods which are described here are discussed in more detail in [59].

---

[21] One of these five events fails the track cuts which are applied in the 1985 analysis, and so is not used for the cross-section calculations.

In practice, it is more natural to use the quantity R, defined as the square of the reciprocal of the event mass. This is proportional to the product of the muon reciprocal momenta, r_1 and r_2:

$$R(M) \equiv 1/M^2 = K(\Theta)r_1r_2 \text{ where } K(\Theta) = -{}^1/_2Q_1Q_2/(1-\cos\Theta) \tag{7.1}$$

where Θ is the angle between the muons. Since the values of r are measured with Gaussian errors which are independent for r_1 and r_2, the value R will be an unbiassed estimate of $1/m_Z^2$. (Strictly, it is the charged reciprocal momenta which are Gaussian, hence the inclusion of the muon charges Q_1 and Q_2.) So if we have several estimates of R (each coming from one of our measured events) $\{R_i; i=1,N\}$, with weights $\{w_i; i=1,N\}$, we can combine these estimates to form a weighted mean:

$$\hat{R} = \Sigma w_iR_i / \Sigma w_i \tag{7.2}$$

This will be an unbiassed estimator of $1/m_Z^2$ provided that the weights do not depend on the measurements of r_1, r_2 and Θ.[22] Usually one sets weights equal to the reciprocal variances to minimise the variance on the result. The variance of R is given by:

$$v(R) = K^2(\rho_1^2\sigma_2^2+\rho_2^2\sigma_1^2) \tag{7.3}$$

to first order, where ρ_1,ρ_2 are the true values of r_1,r_2. Unfortunately, the true quantities are not known, and if the measured values are used instead, a bias is introduced. It is easy to show that if r fluctuates upwards, the weight decreases, and higher mass events get a larger weight, causing a bias to higher masses. Instead, we replace ρ_1,ρ_2 in expression (7.3) by the mean value of r taken over all measurements (so that ρ_1,ρ_2 are effectively replaced by a constant).

The pdf $f(R_i|m)$ which describes the probability of an event with $R = R_i$, given that the mass of the Z is m, is essentially the resolution function:

$$f(R_i|m) \sim \exp[-{}^1/_2w_i(R_i-R(m))^2] \tag{7.4}$$

---

[22] To be more explicit, this means that the weights $\{w_i\}$ must not depend on the deviations of the event parameters from their true values. However, the weights may depend on the true values of the parameters, which may be related to the topology of the event and to where the tracks lie in the detector. So the weights may depend on the 'configuration', but not on 'fluctuations'.

Further, this can be convolved with the probability function $B(m|\mu)$, where B is the Breit-Wigner function, and μ is the mass at the Z pole. From this we can form a likelihood, whose minimum gives an estimate of the Z mass with its error. Due to the symmetry of the Breit-Wigner function and its relative sharpness compared to the di-muon mass resolution, our likelihood effectively reduces to a simple χ^2, whose minimum corresponds to the weighted mean of (7.2).

Explicitly, the likelihood used is

$$\mathcal{L}(\mu) = -\Sigma \log\{ \int B(m|\mu) f(R_i|m) dm \}$$

$$= -\Sigma \log\{ \int \frac{mA}{(m^2-\mu^2)^2+\mu^2\Gamma^2} \exp[-{}^1/_2 w_i (R_i - 1/m^2)^2] dm \} \qquad (7.5)$$

where the constant A is irrelevant to the nature of the minimum of the log likelihood. The decay width is taken as 2.9 GeV [60].

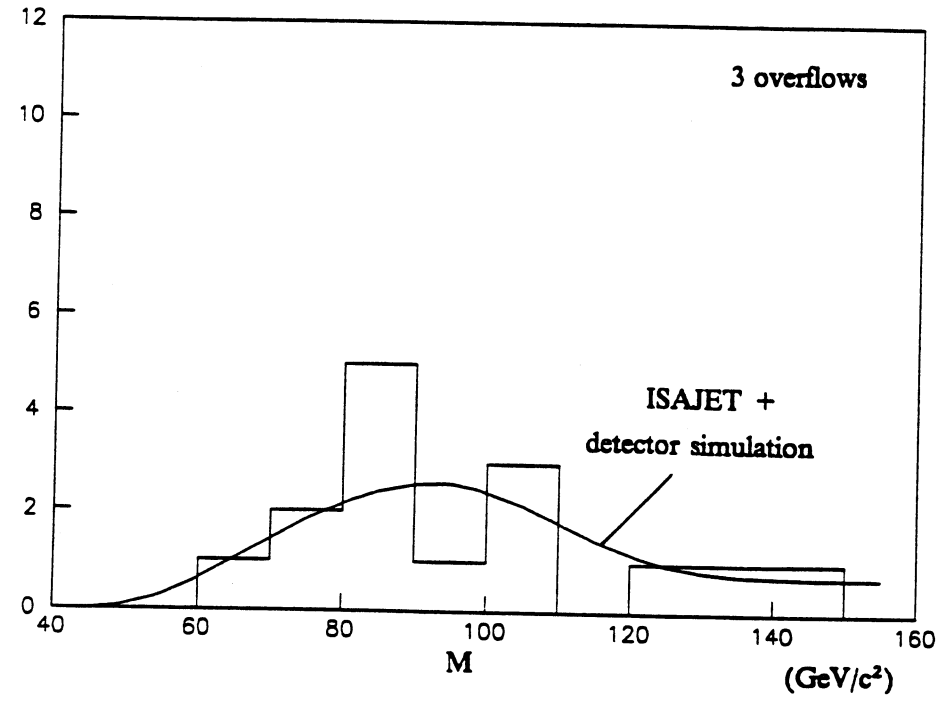

Figure 23: Data Before Energy Balance

7.3 The Energy Balance Method

In an event containing a Z, the missing energy vector can be defined by

$$\text{missing energy} = -(\text{di-muon momenta} + \text{energy flow}) \tag{7.6}$$

where the 'energy flow' is the sum of the vector energies of particles (excluding the muons) detected by the calorimeter. As usual, we restrict ourselves to the transverse quantity, as the measurement of longitudinal energy flow is made difficult by the losses in the forward region of the detector. In an event containing a decay $Z \rightarrow \mu\mu$, we anticipate that there should be no high p_t neutrinos, or other sources of genuine 'missing energy', for example photinos. Thus, in the 'energy balance' method, we impose the constraint that the missing energy vector is zero. In reality there may be some low p_t neutrinos from the decays of low energy particles (π,K,n etc.), and these are best included in the effective resolution of the energy flow of the 'rest of the event'. Indeed, this resolution is parameterised from studies of minimum bias events,[23] which may include low energy decay neutrinos. However one does not expect minimum bias events events to contain the production of high p_t neutrinos, which are usually associated with W and heavy quark decays.

In the method, a chi-squared is formed from the measured muon momenta and the energy flow on an event by event basis. The estimated energy flow is set equal to the negative of the estimated di-muon momenta.

$$\chi^2 = (r_1 - r_{10})^2/\sigma(r_1)^2 + (r_2 - r_{20})^2/\sigma(r_2)^2 + (c_{1y}/r_1 + c_{2y}/r_2 + E_{y0})^2/\sigma(E_y)^2 + (c_{1z}/r_1 + c_{2z}/r_2 + E_{z0})^2/\sigma(E_z)^2 \tag{7.7}$$

where subscript '0' denotes the measured quantities and c_y,c_z are the y and z direction cosines. As usual, the best estimates are obtained by minimising the chi-squared with respect to r_1 and r_2, for each event. These estimates are then used to calculate R_i and w_i for use in the likelihood method described above.

---

[23] events collected with only a pretrigger requirement

7.3.1 Applying Energy Balance

There are several ways in which the chi-squared of equation (7.7) can be used. The classical way to treat a chi-squared minimisation with constraints is to employ the matrix formalism as discussed by several authors, for example [35]. Because of the non-linear functions of r, namely the reciprocals, which appear in the constraints of energy balance, the matrix solutions for r_1 and r_2 must be expressed as functions of the unknown estimates. Therefore, it is necessary to use iteration to estimate the parameters r_1 and r_2. Unfortunately, because the matrix solution overlooks some of the derivatives which vanish when the constraints are linear, the estimates converge to values which do not minimise the chi-squared of (7.7). This was verified by using an internal Monte-Carlo.

An alternative is explicitly to minimise the chi-squared by differentiation. This yields quartic equations which are not readily solved. As a further alternative, we were able to obtain a simple representation of the solution which was amenable to iterative approximations. However, using the internal Monte-Carlo, it was found that often the solutions failed to converge.

The most robust solution of the problem is numerically to minimise the chi-squared. To find the weights $\{w_i\}$, we use a more complete first order expression for the variance of r_1r_2, which allows for the correlations introduced by the energy balance method:

$$v(r_1r_2) = r_1^2\sigma_2^2 + r_2^2\sigma_1^2 + 2r_1r_2\mathrm{cov}(r_1,r_2) \tag{7.8}$$

where in practice r_1,r_2 are replaced by their mean values (evaluated from the complete data set). The variances and covariance are extracted from the covariance matrix $({}^1/_2\partial^2\chi^2/\partial r_i\partial r_j)^{-1}$, evaluated at the best estimates. Also, since r_1 and r_2 are correlated by the energy balance, we use the unbiassed estimate of the product, namely $r_1r_2 - \mathrm{cov}(r_1,r_2)$.

Some Simple Remarks on Energy Balance

Before considering some technical details of the energy balance technique, it is worth looking at some simple aspects of the method. Firstly, if the energy flow of the event is determined very precisely and the muons are not back to back, then by resolving the energy-momentum vectors orthogonal to

each of the muon momentum vectors in turn, it is possible to determine the momentum of the other muon very precisely. Secondly, if the muons are back to back, and the energy flow is determined very precisely to be close to zero while the muon momenta are measured with comparable errors, then the estimates of r_1 and r_2 will both be the average of the two measured quantities, namely $(r_{10}+r_{20})/2$. This is nice because it reduces the variances on the reciprocal momenta by a factor of 2. However, because the estimates, r_1 and r_2, are now highly correlated, we see from the expression (7.8) that the variance on the product, and hence on R, is unchanged. Therefore, in this situation, energy balance has not helped. In practice, the actual situation lies somewhere between these two examples.

Refinements on Energy Balance

1. It is to be anticipated that minimising the χ^2 of equation (7.7) will lead to expressions for r_1 and r_2 which are non-linear functions of the measured Gaussian variables. Therefore, we must expect that our simple estimates of r_1 and r_2 will be biassed. These biases are proportional to the product of the second derivatives of the estimated parameters with respect to the measured quantities, and the variances of the measured quantities. Evaluating second derivatives is numerically unpleasant, and so we have obtained an expression for the biases in terms of first derivatives, which can be evaluated with greater ease. Although this bias could be eliminated by calibration, we apply an analytic correction. The effect of this is to raise the final mass estimate by about 0.5 GeV/c^2. The form of this correction is discussed in appendix C.

2. Using the Monte-Carlos (the internal Monte-Carlo and ISAJET), it was found that a few high mass events received exceptionally high weights. This situation arose when the muons were very close to being back to back, and the energy flow, while having a true value close to zero, was measured as having a large component perpendicular to the line of the muons (which nevertheless was compatible with statistical fluctuations). In these situations, when the energy flow term of the chi-squared dominates the determination of the muon momentum (i.e. small errors on energy flow), then the application of energy balance results in equal muon reciprocal momenta, r. The energy flow contribution to the chi-squared then becomes

$$\chi_E^2 \sim [(E - 2\sin\alpha/r) \div \sigma(E)]^2 \qquad (7.9)$$

where the quantities are illustrated in figure 24.

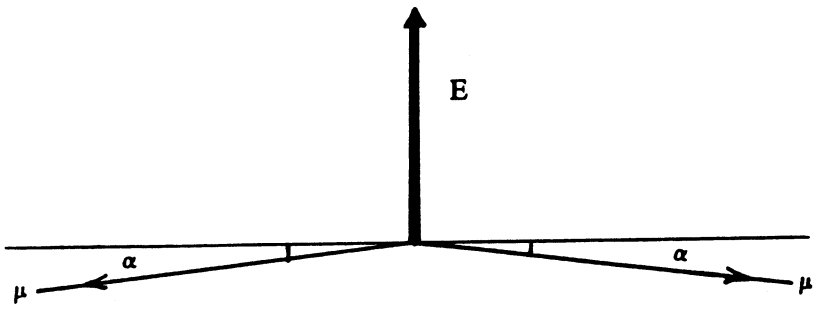

α is small and $E \sim O(\sigma(E))$

Figure 24: Energy Balance - definition of χ_E^2

Minimisation yields an estimate $\hat{r} \approx 2\sin\alpha/E$, with $\sigma(r) \approx (\sigma(E)/E)\hat{r}$. Since α is very small, $\hat{r}$ is very small and so is $\sigma(r)$. It is the latter which is the problem, since it leads to an event with a very high weight.

The origin of the problem lies in the interpretation of the 'error', and hence the event weight. The 'error' usually provides an estimate of the range in which the true value of a parameter lies. In this sense, it is most meaningfully represented by the rms of a distribution. The chi-squared is little more than the logarithm of the pdf. However, the interpretation of the error (or variance) in terms of the curvature of the chi-squared is only appropriate when the pdf is Gaussian, and hence the chi-squared is quadratic. In the situation described here, the chi-squared (7.9) has a very sharp minimum and consequently a very high curvature, leading to an apparently very small error on the reciprocal momentum estimate. Therefore, the event is assigned an unrealistically high weight which does not reflect its statistical significance; and further, this weight is a function of the fluctuations - see the footnote to section 7.2.

In most cases, the Gaussian approximation is not too bad. Where events gain anomalously high weights, the energy balance solution for the momenta is rejected; although, for the real data, only one

of the events showed serious problems. This problem can never be fully overcome, due to the inherent non-Gaussian nature of the chi-squared, but after the removal of severe problems, the effects can be allowed for by calibration.

3. In principle, the use of energy balance allows a reasonable attempt to be made to restore the sign of the charge (Q) of a fast muon whose charge has been incorrectly determined. Viewed as a function of the variable Q/p = Qr, the chi-squared has two minima either side of Qr = 0. Where one of the charges is mismeasured, the absolute minimum will be associated with the wrong charge determination. Thus, by choosing the second minimum, the sign can be restored and the momentum estimated accordingly. A guess can be made as to which track is mismeasured by using the quantity $r/\sigma(r)$ - its proximity to 0 indicating a poorer charge determination. In practice, after OMF, only one data event had muons measured with like signs, and since this event received a large correction (see point 1. above), the energy balance for the event was suspect and was not used.

7.4 A More Detailed Look at the Data

The events were scanned on the Megatek to check for particles belonging to jets which were identified in the CD and appeared to escape through gaps in the calorimetry. Three events were found in this category, and since it was considered that the calorimetric energy flow was unreliable for these events, the mass estimates before energy balance were used. The same was true for one event where the muon passed through a light guide, causing an anomalous energy flow.

One event had a mass of 53 ± 16 GeV/c^2 and was fairly well measured. After energy balance, the mass became 91 ± 10 GeV/c^2. The event was compatible with $Z \rightarrow \tau\tau$ with $\tau \rightarrow \mu\nu\nu$, or a mismeasured pair from $Z \rightarrow \mu\mu$. For the mass fitting, we only want to use the well measured events which we are fairly sure have come from the decay $Z \rightarrow \mu\mu$. Therefore, in order to remove this event, two mass cuts were made in $1/M^2$. These cuts were approximately symmetric about the mass peak, and studies with ISAJET events suggested that they would remove about 1% of the weighted distribution, see figure 26. The cuts removed events with $1/M^2 > (60\ \text{GeV}/c^2)^{-2}$ and $1/M^2 < -(180\ \text{GeV}/c^2)^{-2}$. (Out of 435

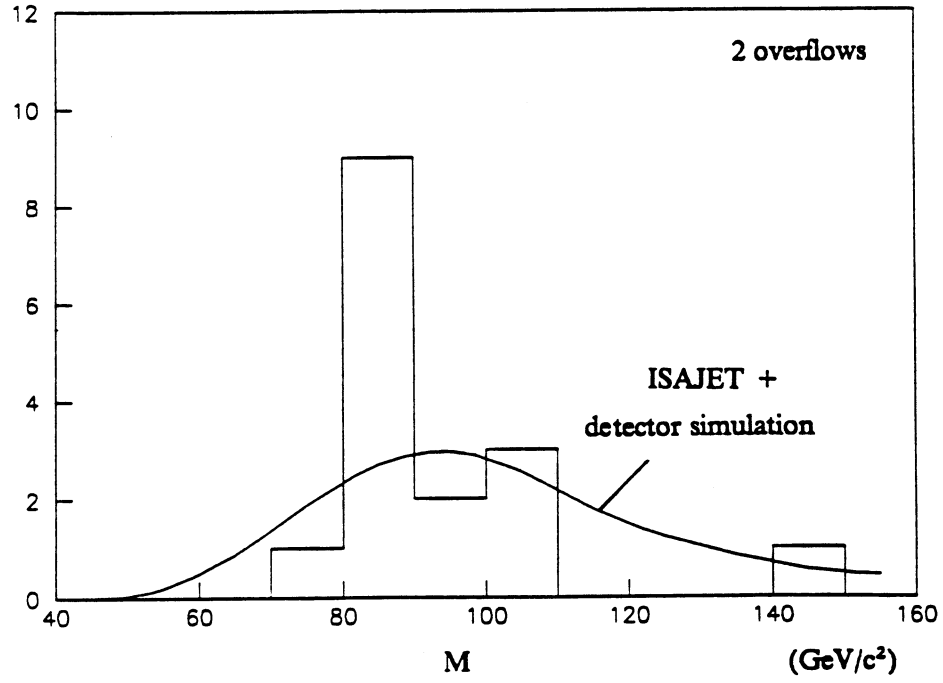

Figure 25: Data After Energy Balance

$\mu\mu$ events selected from ISAJET data, 3 events came from $Z \rightarrow \tau\tau$. The di-muon masses of these were between 50 and 60 GeV/c^2.) Making this cut caused a small bias, for which a correction was made.

7.5 Calibration and Errors

It had been intended to calibrate the mass fitting procedure with ISAJET events[24] however, as was discussed in the previous chapter, there were problems with the simulation of CD tracks. It was found for a Z mass of 94.1 GeV/c^2, the reconstructed mass was 97.8 GeV/c^2 - where this discrepancy arose solely from the biases in the simulation. Since the methods of section 7.2 are not expected to suffer from any significant biases, there should be no biases arising from the mass fitting program, and

[24] Again, these Monte-Carlo events were selected, in precisely the same way as the real events, from the inclusive Z production, described in appendix F.

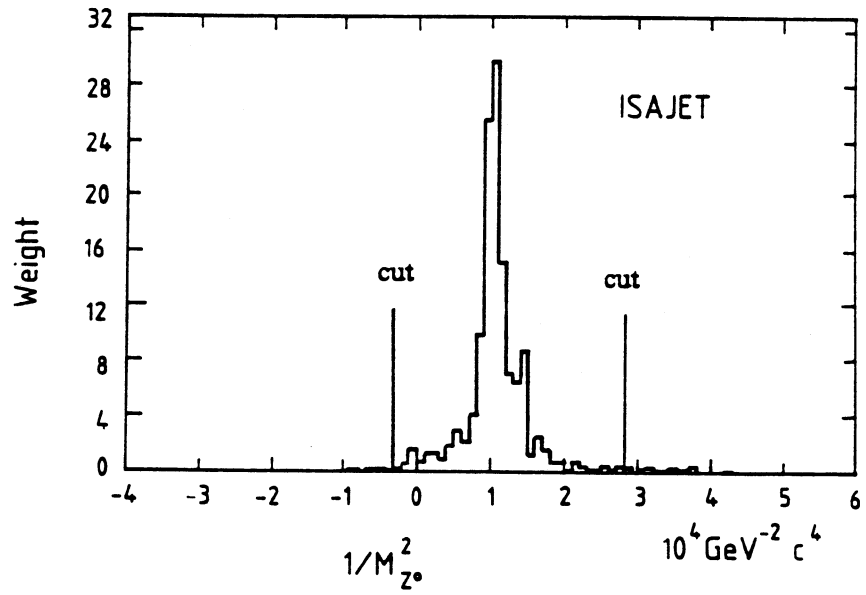

Figure 26: $1/M^2$ for ISAJET Events

thus no attempt was made to calibrate the program for use without energy balance. However, there could be some biases on the muon momenta after energy balance. Therefore the effect of using the energy balance was assessed by comparing the results on ISAJET data with and without energy balance. A limit on the systematics from the CD momentum measurement was estimated, as for the W's.

The statistical errors on the Z mass were estimated by fluctuating the reciprocal momenta for each event, as prescribed by the covariance matrix. This was done for a number of 'experiments', each with the same number of events as in our data set; and for each, an estimate was made of the Z mass. The confidence limits corresponding to one standard deviation were found from the distribution of these different estimates. This is a little better than relying on the curvature of the likelihood, since expression (7.8) which was used for the variances is only a first order approximation, and is inevitably an underestimate.

7.6 Results

The masses of the individual events are given in table 13 (the errors are simple parabolic errors derived from those on $1/M^2$). Because of their questionable nature, the 'radiative' events[25] are not used.

Table 13: Masses for Z Candidates

	mass before energy balance	mass after energy balance
1983	74 ±20	89 ±25
	209 ±336	not used
	radiative event	
	130 ±215	104 ±90
	83 ±31	83 ±28
1984	101 ±49	87 ±18
	94 ±35	81 ±11
	84 ±15	89 ±15
	53 ±15	91 ±14
	106 ±22	95 ±11
	142 ±60	not used
1985	163 ±70	109 ±17
	277 ±518	like sign
	85 ±24	not used
	135 ±88	91 ±14
	85 ±36	86 ±35
	87 ±47	not used
	67 ±11	83 ±11
	radiative event	
	106 ±26	103 ±21
	80 ±24	76 ±20

Using these events, we obtain the uncorrected masses shown in table 14. The table shows, that in spite of increased data in 1985, the quality of the data was disappointing - mainly due to the muons populating all the 'bad' regions of the detector: only one of the events had two good muon chamber tracks. Before the final corrections, the masses obtained are $94.7\ +8.4, -6.6\ \mathrm{GeV/c^2}$, before energy

[25] There are two events where there is an energetic photon candidate and the muon-muon-photon mass is close to the Z mass. It is not clear whether the photons in these events are radiated from the muons, or whether they are indicative of some new process.

balance; and 93.1 $+5.2, -4.8$ GeV/c^2, after energy balance.

Table 14: Masses Before Correction for Individual Years

year	mass before energy balance	mass after energy balance
1983	$89.7 \; {}^{+31.6}_{-15.8}$	$97.2 \; {}^{+32.9}_{-16.4}$
1984	$99.2 \; {}^{+14.1}_{-10.2}$	$90.6 \; {}^{+7.2}_{-6.2}$
1985	$92.9 \; {}^{+12.5}_{-8.7}$	$96.1 \; {}^{+8.7}_{-6.8}$
All	$94.7 \; {}^{+8.4}_{-6.6}$	$93.1 \; {}^{+5.2}_{-4.8}$

Finally, for interest the results of OMF on the 1985 data are shown in table 15. It can be seen that quite an improvement is made by using Iarocci information. This arises because in the 1985 data there are several muons which do not have good muon chamber tracks but do have Iarocci hits. Further, due to the looser CD track requirements for Z candidates, the CD momentum determination is less dominating in the OMF procedure. Also, the errors on the momentum dominate the uncertainty arising from the intrinsic width of the Z; so the reduction of the momentum errors has a more direct effect.

Table 15: Masses Before Corrections for 1985

	before energy balance	after energy balance
CD only	108.3 ± 22.0	100.9 ± 11.0
OMF (without Iarocci's)	103.9 ± 15.8	101.3 ± 8.8
OMF (with Iarocci's)	92.9 ± 10.1	96.1 ± 7.5

Correction factors of -0.6 ± 0.4 GeV/c^2 (no energy balance) and -0.9 ± 0.2 GeV/c^2 (energy balance) were applied, to correct for the effects of the $1/M^2$ cuts. Using the ISAJET events, we estimated that a calibration shift of -1.5 ± 0.5 GeV/c^2 was required to correct for small biases in the energy balance method. Looking at the effects of various systematics in the calorimetry led to an estimate of an error of a further ± 1.4 GeV on the energy balance mass estimate. Finally, there is a 3% limit on systematics on the CD momentum measurement.

These lead to results: $94.1\ +8.4,-6.6(\text{stat})\ \pm 2.8(\text{syst})\ \text{GeV}/c^2$ and $90.7\ +5.2,-4.8(\text{stat})\ \pm 3.2(\text{syst})\ \text{GeV}/c^2$ for the two methods.

The statistical errors above are calculated as described in the previous section. If we use the likelihood to estimate simple parabolic statistical errors,[26] we obtain ± 7.2 and $\pm 4.9\ \text{GeV}/c^2$ respectively. A third way of obtaining the statistical errors is to use the spread of the values of $1/M^2$ (which is non-trivial in the presence of weighted events, if one requires an unbiassed estimate of the variance). The distribution of events before and after energy balance is shown in figures 23 and 25 respectively, and from the weighted distributions, errors of ± 7.6 and $\pm 3.0\ \text{GeV}/c^2$ are obtained. The errors derived before the application of energy balance are in good agreement, suggesting that the total CD errors do indeed provide a good description of the statistical errors. The errors for the energy balance result are slightly curious since the spread of the measurements seems to have been reduced more than would be anticipated from the nominal errors on the event parameters. Looking at the ISAJET data, we obtained a statistical error of $\pm 1.43\ \text{GeV}/c^2$ before energy balance,[27] to be compared with an error of ± 1.03 after. The reduction in error is compatible with that obtained on the real data using the fluctuation estimate. This confirms that the energy balance method has reduced the spread of masses for the data more than one would expect, and that the error estimate derived with our first method is reasonable.

---

[26] Errors are approximately symmetric in $1/M^2$ – this means they will not be symmetric in M – however, for small errors, a simple estimate of the errors is given by $\sigma(M) = 0.5M^3\sigma(1/M^2)$.

[27] The size of the error estimated with the Monte-Carlo events will depend on the number of events used. 341 events went into the fit, compared with 18 from the actual data. Therefore, the error should be reduced by a factor $\sqrt{(341/18)} = 4.4$, which is in good agreement with observations.

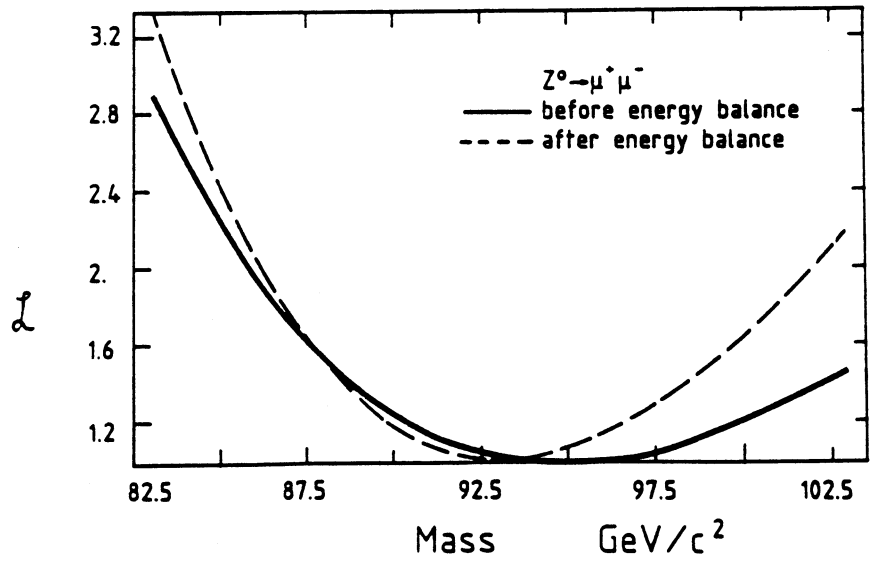

Figure 27: Likelihood Curves Before and After Energy Balance

7.7 Conclusions on the Z Mass

Using the current UA1 $Z \rightarrow \mu\mu$ candidates, we have obtained an estimate of the Z mass:

without energy balance, $94.1 + 8.4, -6.6(\text{stat}) \pm 2.8(\text{syst})$ GeV/c²,

and with energy balance, $90.7 + 5.2, -4.8(\text{stat}) \pm 3.2(\text{syst})$ GeV/c².

This result is to be compared with our result of 93.1 ± 1.0 ± 3.1 GeV/c² from the electron channel [55]. Also, it is in good agreement with the result from the UA2 Collaboration of 91.5 ± 1.2 ± 1.7 GeV/c² [56]. For subsequent calculations, we choose to use the energy balance result.

7.8 The Standard Model Parameters from the Muon Channel

An outline of the Standard Model was given in chapter 5. Quantitatively it predicts the ratio of the W and Z masses and also the strength of the weak (charged and neutral) coupling constants in

terms of a single parameter: $\sin^2\theta_W$ [61], [62]. By manipulating the form of these results, it is possible to provide tests of the consistency of the model. Such tests are important since they can ultimately yield information on the unknown parameters of the Standard Model: the top quark mass, the Higgs mass and the number of additional fermion generations [61], [63].

In order to compare experimental results from different energy ranges (for example: low energy neutrino scattering with results from the Collider), it is necessary to allow for the radiative corrections. Therefore, $\sin^2\theta_W$ is defined by:

$$\sin^2\theta_W \equiv 1-(m_W/m_Z)^2 \tag{7.10}$$

since this definition is least susceptible to theoretical uncertainties[28] [64]. All other estimates of $\sin^2\theta_W$ are radiatively corrected to be compatible with this definition.

Following the ideas of reference [63], we use our measurements [65] of the W and Z masses to estimate i) the value of $\sin^2\theta_W$, ii) the radiative correction Δr defined by

$$m_W^2 = \pi\alpha \{\sqrt{2}G_\mu \sin^2\theta_W(1-\Delta r)\}^{-1} \tag{7.11}$$

where $\sin^2\theta_W$ can be provided by equation (7.10) or low energy results,[29] and G_μ is the muon decay constant. The values of the constants can be found in reference [63]. Other parameters can be obtained; however, they are not all independent.

Using expression (7.10), some of the systematics on the W/Z masses cancel in the ratio. In table 16, our value of $\sin^2\theta_W$ is compared with the current estimate from the UA1 electron analysis [55], the UA2 result [56] and a compilation from νN experiments [66]. The latter provides a measurement of $\sin^2\theta_W$ independent of the W and Z masses, by measuring the ratios of charged to neutral current couplings. To estimate Δr, G_μ is used to make connection with the weak charged current couplings. At the tree level, Δr is zero; however, there are important radiative corrections, which make it non-zero. These come mainly from the photon vacuum polarisation, which modifies α at the W/Z mass scale. These corrections are predicted, within the framework of the Standard Model, and depend on the

[28] The only renormalisation is that of the fine structure constant, α.

[29] In what follows, we will use the low energy estimates, which provide greater precision.

unknown parameters listed at the start of this section. The theoretical result [63] given in table 16 is evaluated for a top quark mass of 60 GeV/c^2 and a Higgs mass equal to m_Z. The theoretical error quoted in the table is due to the hadronic contributions.

The precision which is obtained from the muon channel is insufficient to be able to derive helpful conclusions.

Table 16: Standard Model Parameters

	$\sin^2\theta_W$			Δr		
UA1 (muon)	0.187	± 0.148	± 0.033	0.10	± 0.12	± 0.08
UA1 (electron)	0.211	± 0.025		0.125	± 0.021	± 0.057
UA2 (electron)	0.232	± 0.025	± 0.010	0.068	± 0.022	± 0.032
νN	0.232	± 0.004	± 0.003		–	
Theory		–		0.071	± 0.002	(theory)

8. OVERVIEW OF SUPERSYMMETRY

In this chapter some of the problems of the Standard Model are discussed. These provide the motivation for its extension to include Supersymmetry (SUSY) [67]. We discuss some of the theoretical and phenomenological ideas behind SUSY and present a selection of the current experimental results.

8.1 The Need for SUSY

Throughout the history of particle physics, scientists have attempted to obtain the simplest and neatest description of the constituents of our universe. There is a diversity of 'fundamental' particles and forces and the goal is to unite these into a simpler scheme.

A major step forward in our understanding has arisen with the emergence of the Standard Model, incorporating the electroweak theory of GSW, discussed in chapter 5. The obvious step after this is to unite the electroweak force, associated with the group $SU(2)_L \otimes U(1)$, with the QCD colour force, associated with the group $SU(3)_C$. This is the task of Grand Unified Theories (GUT's). It turns out that it is possible to embed the known particles in certain groups, for example SU(5), SO(10), SO(32); and at very high energies the interactions associated with $SU(3)_C$, $SU(2)_L$ and U(1) asymptotically attain the same coupling strengths. The increased symmetry of these groups introduces additional gauge bosons, labelled X and Y, with masses $m_X \approx 10^{15}$ GeV/c^2. The manifestation of the separate gauge forces at low energies less than about 1 TeV implies that the symmetry of the GUT group is broken, and the scale at which this happens is m_X. The mechanism proposed for this is spontaneous symmetry breaking (ssb) generated by a new scalar field - a heavy Higgs mechanism. The Higgses have vacuum expectation values (vev's) which are of the order of the mass scales at which ssb occurs (see section 5.3) and their masses are proportional to their vev's. Therefore, in the theory, there are light Higgses which generate the masses of the W and Z bosons, and have vev's of the order of $m_W \approx 10^2$ GeV/c^2, while the heavy GUT Higgses have vev's of the order of $m_X \approx 10^{15}$ GeV/c^2.

On the face of it, all is fine and it would seem that we are well on the way to a unified theory. However, since the two sets of Higgses inevitably interact, the light Higgs will pick up a contribution to its mass, proportional to the vev of the heavy Higgs, which is of the order of m_X [68]. This then destroys the ssb at the W mass. By special arrangement of the couplings, known as 'fine tuning', it is possible to restore the light Higgs mass to around 10^2 GeV/c^2. However, this requires adjustments to m_H^2 to a precision of $(m_W/mx)^2 \approx 10^{-26}$! This is bad enough, but because the Higgses are elementary scalars, they pick up quadratically divergent contributions to the mass, which must be controlled at each level of perturbation. While there is no reason why this is not possible, it seems unnatural and inelegant. Maybe, it is indicative that the use of perturbation theory is not the 'natural' way to perform calculations which require renormalisation, and that perhaps we have 'missed the point'. Further, Hawking et al [70] propose that a scalar propagating through the space-time foam picks up radiative corrections due to quantum gravity which produce a shift in the Higgs mass of the order of the Planck mass, $m_P \approx 10^{19}$ GeV/c^2.

In addition to the interactions with the heavy Higgs, there are simple, quadratically divergent contributions to the propagator of the light Higgs. These modify the effective mass of the elementary scalar[30] particle [69], producing a shift:

$$\delta m_H^2 \sim g^2 \int_p^{\Lambda} k.dk \qquad (8.1)$$

where the limits of the integration are the momentum of the particle, and Λ - the scale at which 'new physics' manifests itself. In the absence of any new interactions, Λ is of the order of m_X.

There are two solutions to the above problems:

1. Dynamic symmetry breaking or Technicolour - kill the Higgs !
2. Supersymmetry (SUSY) - kill the quadratic divergences.

---

[30] fermions and vector particles do not suffer from these problems [70]

8.1.1 Technicolour

Technicolour [71] avoids the quadratic divergences associated with the Higgses by dissolving them on a scale Λ around 1 TeV. The Higgs is replaced by a technipion, containing technifermions. The technipions have interactions with the gauge bosons analogous to the coupling of a normal pion to a W or Z. Thus the gauge bosons effectively gain mass due to the modification of the propagator - the mass being proportional to the technipion form factor. With this mechanism, the troubles associated with the vev's in ssb are totally avoided. However, there are several problems with Technicolour:

a. Unlike with ssb, it is necessary to invoke additional features (Extended Technicolour) to generate fermion masses.
b. It is anticipated that there should be light technipions around 5 to 15 GeV/c^2 - these have not been seen at PEP or PETRA.
c. Technicolour tends to lead to flavour changing neutral currents far in excess of present limits.

So Technicolour has been abandoned by most theorists in favour of SUSY.

8.1.2 Supersymmetry

It can be shown [72] that the quadratically divergent corrections to the propagator of a scalar are opposite in sign for fermion and boson loops. By invoking a scalar partner for every fermion and a fermion for every boson, it becomes possible to cancel the radiative divergences which plague the Higgs. If the fermions or bosons have masses m_f or m_b, then the shift of the square of the Higgs mass is proportional to $|m_f^2 - m_b^2|$. As will be seen below, SUSY gives rise to a spectrum of pairs of bosons and fermions, and these are able to restore the respectability of the Higgs.

It was originally shown by Coleman and Mandula [73] that the only symmetries which preserved the unitarity of the S matrix were those associated with Poincaré invariance (space-time invariance) and internal symmetries (global symmetries, e.g. isospin; and local symmetries, e.g. gauge symmetries) and their direct products. However, they considered only the existence of commutators of the generators, and the transformation of fermions to fermions and bosons to bosons. By contrast, SUSY introduces explicit transformations between the different types of particles:

$$Q|f> = |b> \text{ and } Q|b> = |f> \tag{8.2}$$

Since the algebra [74] of the generator Q includes anticommutators, it avoids the no-go theorem of Coleman and Mandula. In fact, the symmetries of the generator Q provide the only remaining symmetry of the S matrix [75]. One can consider several such generators $\{Q^i; i = 1,N\}$ where N is ≤ 8 and where each Q^i relates different spins. However, N = 1 is the most popular model due to its simplicity and the fact that the others lead to left-right symmetric models which are in conflict with the existence of $SU(2)_L$.

The (anti-)commutation relations satisfied by Q are:

$$[Q,M^{\mu\nu}] = i\sigma^{\mu\nu}Q \tag{8.3}$$

$$[Q,p^{\mu}] = 0 \tag{8.4}$$

$$\{Q_\alpha,\bar{Q}_\beta\} = -2(\gamma p)_{\alpha\beta} \tag{8.5}$$

where $M^{\mu\nu}$ are the generators of the proper Lorentz transformations (i.e. space-time rotations); $\sigma^{\mu\nu} \equiv {}^1/_4[\gamma^\mu,\gamma^\nu]$; p^μ is the generator of translations (i.e. it is the four-momentum); and α and β are spinor indices.

From (8.3), we see that Q transforms as a spinor. This is not unreasonable, since in (8.2), to transform a fermion into a boson requires an operator which transforms with half integer spin.

From (8.5), we see that the operation of Q on itself leads to the momentum operator - the generator of space-time translations, and in this sense, Q is the 'square root' of translation.

The N = 1 operator, Q, transforms within the spin supermultiplets:

$$\text{gauge } (1,{}^1/_2) \text{ and chiral } ({}^1/_2,0).$$

The 'chiral' fields are the matter fields, which are labelled as 'left' or 'right' handed; the 'gauge' fields are those which appear when gauge invariance is imposed; and in addition there are the Higgs fields. It is important to ask if the operation of Q on known particles yields particles which are also identified. Since Q carries no internal quantum numbers (for example: charge, baryon number, lepton number),

all the internal quantum numbers of a particle will be unchanged by the operation of Q. Within the known spectrum of particles, it is impossible to identify partners which have all the same quantum numbers, apart from spin. We conclude that if Supersymmetry is true, then for every known particle, there exists a supersymmetric partner (or sparticle) which has not been observed yet. This is somewhat uneconomical ! A list of some of the particles and their partners is shown in table 17. The naming convention is such that the partners of the fermions gain the prefix 's'; while the partners of the bosons, the suffix 'ino'. The partners are represented by a tilde over the particle symbol.

Table 17: Particles and S-Particles

particle	spin	sparticle	spin
Higgs	0	Higgsino	$^1/_2$
lepton	$^1/_2$	slepton	0
neutrino	$^1/_2$	sneutrino	0
quark	$^1/_2$	squark	0
photon	1	photino	$^1/_2$
gluon	1	gluino	$^1/_2$
W	1	wino	$^1/_2$
Z	1	zino	$^1/_2$

It is important to note that for every known particle, there exists a sparticle. For example, when discussing the electron, one should distinguish between two particles: the left handed electron, e_L, which is a member of the weak isospin doublet $(\nu,e^-)_L$, and the right handed electron, which is the singlet e_R. The SUSY partners are $\tilde{e}_L$ and $\tilde{e}_R$. Since the sleptons are spinless, and therefore do not have spinor wave functions, they cannot have handedness in the sense of being eigenstates of $1\pm\gamma_5$. 'L' and 'R' are therefore labels which distinguish particles.

From (8.4), we see that if Q and p^μ commute, then so do Q and $p\cdot p$. Therefore, since p^2 is the mass operator, the particles related by Q must have the same mass.

8.2 SUSY Phenomenology

8.2.1 Masses

The non-observation of the supersymmetric partners of the electron, muon, gluon and quarks is evidence that if these particles are to exist, then, in contradiction to the conclusions of the last section, they cannot have the same masses as the known particles. Therefore, the world cannot be exactly invariant under transformations generated by Q. Thus, SUSY must be broken and the masses of the sparticles may be larger than those of their partners. Nevertheless, the symmetry breaking must not invalidate the original aim of taming the quadratic divergences of the Higgs. Therefore, we require that $|\tilde{m}^2 - m^2|$ is less than or of the same order as m_W^2 (SUSY masses are denoted by $\tilde{m}$). Thus the SUSY masses ought to be in the region of 0 to 1 TeV/c^2.

Breaking SUSY turns out to be non-trivial due to its special properties. For example, invoking ssb introduces scalar fields with negative mass-squared terms; in turn, this carries over to the fermion partners, giving them imaginary masses. Symmetry breaking can be obtained by explicitly adding mass terms to the Lagrangian or alternatively it can be extracted from local supersymmetry or Supergravity (SUGRA) in the presence of ssb. The coupling of the particles and sparticles to the Goldstino generates a mass difference (see chapter 9 of reference [72]). Unfortunately, the predictions which can be derived are very model dependent.

In the analysis which follows in chapter 9, we consider a model in which the photino is the lightest supersymmetric particle (see below), the wino and zino have masses greater m_W and can be ignored as can the squarks; and the sleptons are unstable, decaying very rapidly.[31] It is a immaterial whether the sneutrinos decay - whatever, they will give missing energy. If they do decay, it is through the triangle graphs of figure 28. (Expressions for the decay widths of the sneutrino and selectron are given in chapter 3 of reference [72].)

---

[31] For $\tilde{m}_l \geq \tilde{m}_\gamma$, the width will be $\alpha\tilde{m}_l/2$ which is around Γ_W, giving a $c\tau$ of about 1fm.

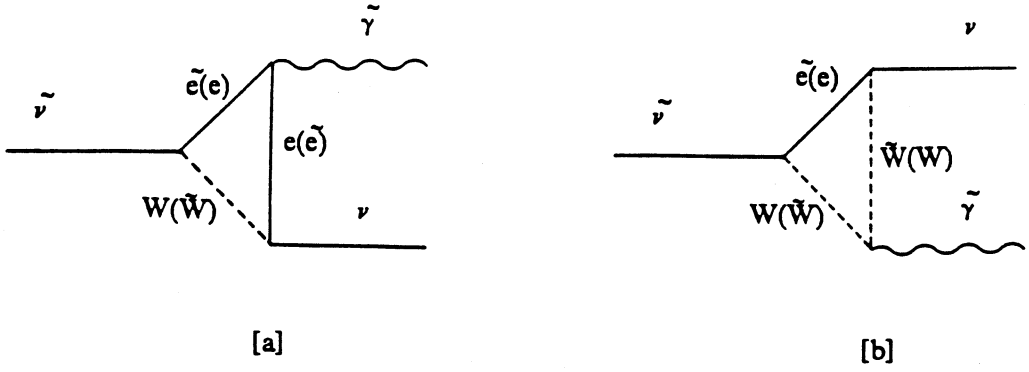

Figure 28: Examples of Graphs for Sneutrino Decay

A typical SUGRA model, which has some correspondence with the above, is discussed by Kounnas et al [76]. The masses derived in this model are shown in table 18.

Table 18: Suggested SUSY Masses from one Supergravity Model

$\tilde{m}_\gamma$	~ 5 GeV/c²	$\tilde{m}_W$	~ 80 GeV/c²
$\tilde{m}_{l,\nu}$	~ 25 GeV/c²	$\tilde{m}_q$	~ 60 GeV/c²

Because of the different couplings of the left and right handed selectrons, the presence of renormalisation effects causes the mass degeneracy of the left and right handed states to be lifted. Looking at $W \rightarrow \tilde{e}_L \tilde{\nu}_L$ provides information on $\tilde{e}_L$, while, in principle, the decay $Z \rightarrow \tilde{e}_L \tilde{e}_L$ and $\tilde{e}_R \tilde{e}_R$ provides information on $\tilde{e}_R$.

Further, we note that in the light of the result $\tilde{m}_g > 53$ GeV/c² (see experimental results below), it becomes less plausible that $\tilde{m}_\gamma = 0$ GeV/c²; since in a minimal N = 1 SUGRA model, $\tilde{m}_\gamma \approx \tilde{m}_g/6$.

8.2.2 R-Parity and the LSP

In SUSY theories, there is an additional global symmetry, leading to a conserved 'charge' called R-parity. Its definition is not unique; however all the 'known' particles (including the Higgs) have one value, while their SUSY partners have another value. When a massive sparticle decays it will eventually give rise to the lightest supersymmetric particle (LSP), which is unable to decay due to the conservation of R-parity and consequently is stable. In many models, the LSP is taken to be the photino.

It is important to consider the interaction of the LSP with matter, in particular, its signature in the calorimeter of a collider detector.[32]

The Consequence of the Photino as the LSP

Firstly, we consider the case when the photino is the LSP, while the selectron is significantly more massive. An energetic photon loses energy by pair production; however, the corresponding process for a photino (an example of such a graph is shown in figure 29 [a]) is highly suppressed due to the difficulty of obtaining the required centre of mass energy. Fayet [77] has shown that the most important process is Compton scattering (for an example, see figure 29 [b]). However, this too is highly suppressed due to the propagator involving the massive selectron. The nature of the suppression is identical to that found for neutrino interactions, which are suppressed by the exchange of a very massive W boson. The cross-section, relative to the antineutrino cross-section, is given by

$$\sigma(\tilde{\gamma}e \rightarrow \tilde{\gamma}e) = (75\text{Gev}/\tilde{m}_e)^4 \, \sigma(\bar{\nu}e) \qquad (8.6)$$

In addition there are interactions with the nuclei to consider. Nevertheless, the cross-sections are very low in the relevant energy range, and the flux is so low that one would not expect a photino to be seen at a collider (with the above conditions), and it behaves as an additional source of missing energy.

---

[32] The significance of a collider detector is the implied energy available to an LSP, and the implication of low fluxes of such particles.

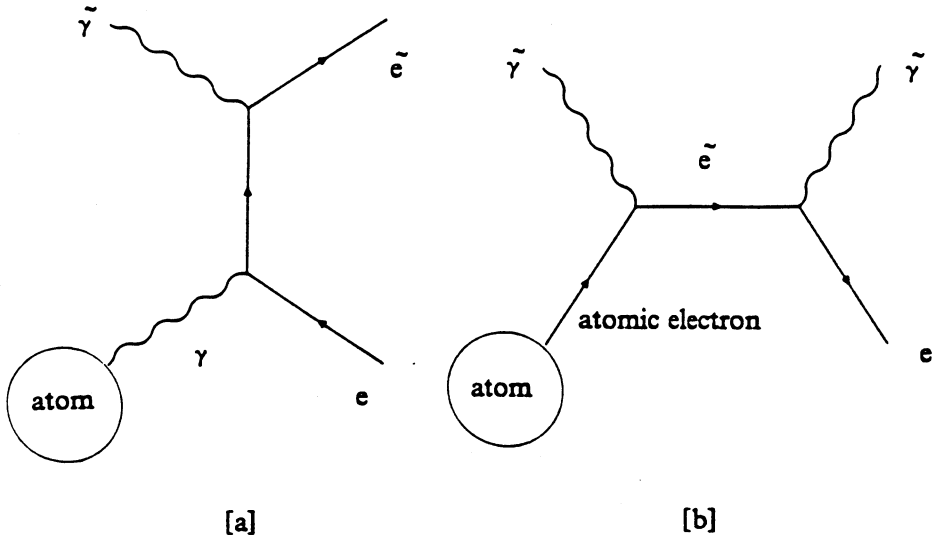

Figure 29: Photino Interactions with Atomic Electrons

The Consequence of the Selectron as the LSP

In the case of a stable selectron [79], since the particle is charged, it can radiate photons. Very light selectrons readily radiate bremsstrahlung, and thus behave like electrons. Heavier selectrons will be only minimum ionising, and so behave like muons.

8.3 Experimental Results

At present, there is no evidence for SUSY from any experimental observations. The most promising suggestions of the manifestation of SUSY came in the observations of 'monojets' by the UA1 collaboration. These results are considered below.

8.3.1 Missing Energy Analysis of UA1

In 1984, UA1 reported on the observation of events with large single hadronic jets (monojets) with little visibly recoiling against them (leading to 'missing energy') [81]. These events gave rise to speculation that their origin was the pair production of squarks or gluinos with a mass around

40 GeV/c^2 [75]. It was suggested that the squarks decayed to quarks (giving rise to jets) and photinos (giving rise to missing energy). One of the squarks gave most of its energy to a jet, while the other gave most of its energy to the photino, and the second smaller jet failed to cross the threshold of 12 GeV.

However careful analysis by UA1 of the final data set[33] [82], [83], has shown that the monojets observed are well described by

- $W \rightarrow \tau\nu \rightarrow$ hadrons (70%),
- $Z \rightarrow \nu\nu$ with a recoil jet (14%),
- jet fluctuations (7%),
- $W \rightarrow e\nu$, $W \rightarrow \mu\nu$ and $W \rightarrow \tau\nu \rightarrow$ leptons (7%),

The agreement between the Monte-Carlo predictions and the data is used to provide limits on the mass of a fourth generation heavy lepton: $m_l > 41$ GeV/c^2 at 90% confidence [84]. Subsequently, the analysis has been extended [85] to maximise the sensitivity to SUSY in the hadronic sector. Events were selected with the following cuts:

1. It was required that the missing transverse energy, $\not{E}_t$, > 15 GeV and $N_\sigma > 4$, where $N_\sigma \equiv \not{E}_t/\sigma(\not{E}_t)$.
2. There should be ≥ 2 jets with $E_t > 12$ GeV and with CD validation of the largest jet.
3. Events with electrons or muons were removed.
4. The tau likelihood [82], L_τ, should be negative in order to remove most of the $W \rightarrow \tau\nu$ decays.
5. The angle in the transverse plane, $\Delta\phi$, between the two highest E_t jets should be $< 140°$ (see figure 30),
6. Finally, additional technical cuts were applied to remove cosmic rays, beam halo and double interactions.

Four events passed the cuts, where the expected backgrounds are:

- heavy flavour decays: 2.0 events

---

[33] with an increase of a factor of six on the integrated luminosity

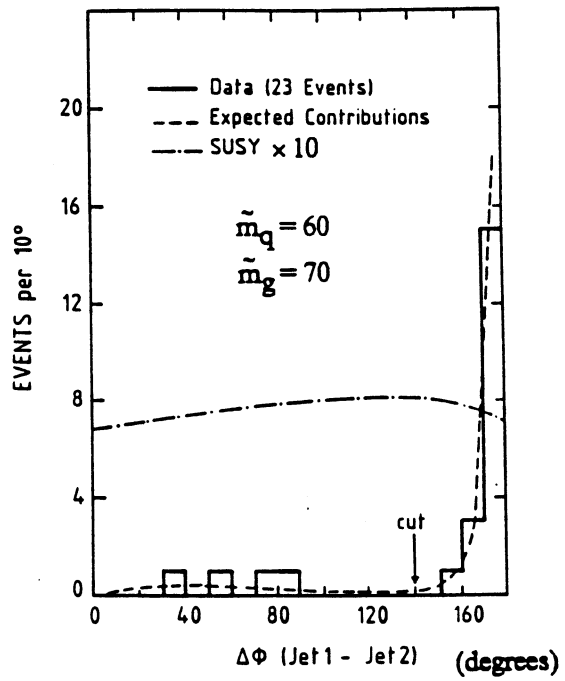

Figure 30: $\Delta\phi$ between Two Highest E_t Jets

- $W \rightarrow \tau\nu$: 1.9 events
- $Z \rightarrow \nu\nu$: 1.2 events
- jet fluctuations: 0.2 events

with a total of 5.2 ± 1.9 events. For example, with $\tilde{m}_q = \tilde{m}_g = 70$ GeV/c², one would expect an additional 10.2 events. This leads to the limit on the squark and gluino masses shown in figure 31.

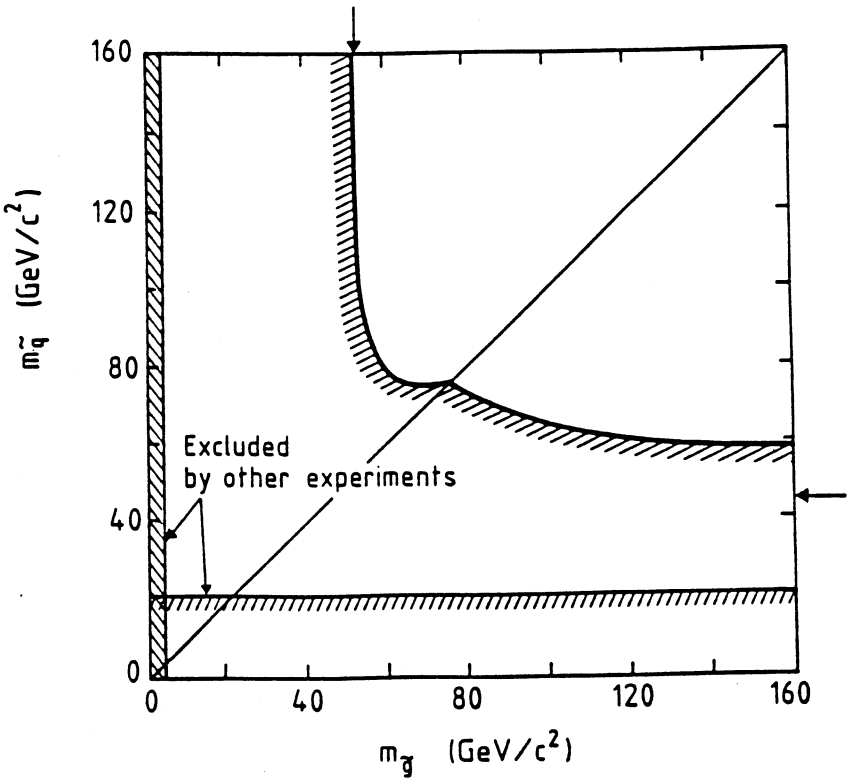

Figure 31: 90% Confidence Limit on Squark and Gluino Masses

8.3.2 Search for $W \to \tilde{e}\tilde{\nu}$ by UA1

A quick study of the process $W \to \tilde{e}\tilde{\nu}$ (with $\tilde{m}_\gamma = 0$) was made by UA1 using the data from 1982, 1983 and 1984 [86]. No evidence was found for $W \to \tilde{e}\tilde{\nu}$ and the limits obtained are shown in figure 32.

This search has been considerably extended with

- more data - including 1985 data,
- improved methods and, in particular, better Monte-Carlo,
- more channels.

The new analysis is presented in chapter 9.

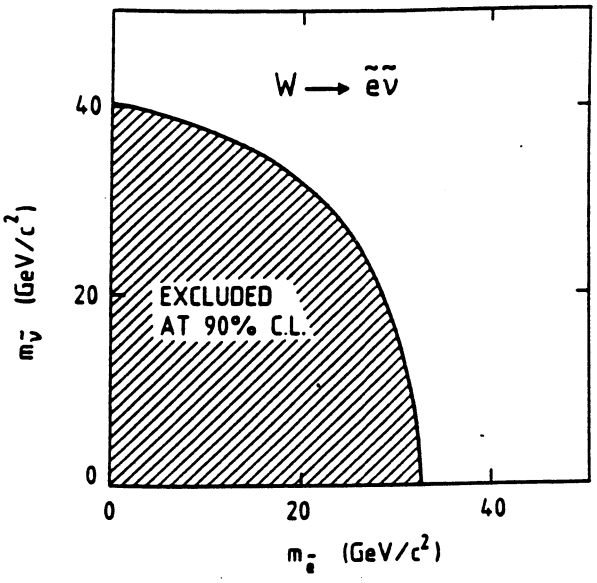

Figure 32: 90% Confidence Limit on Selectron and Sneutrino Masses

8.3.3 Search for SUSY by UA2

UA2 have used their di-electron data to search for $Z \rightarrow \tilde{e}\tilde{e} \rightarrow ee\tilde{\gamma}\tilde{\gamma}$ (where $\tilde{m}_e > \tilde{m}_\gamma$) [87]. This has been done using a two dimensional distribution of events with p_t^{η} against M_{ee} (the mass of the electron pair) (see figure 33). In the dashed region, they observe one event, while the number expected from Drell-Yan is six [78]. The absence of a SUSY signal leads to the confidence limits shown in figure 34. The downwards fluctuation of the background has not been used to provide stronger limits.

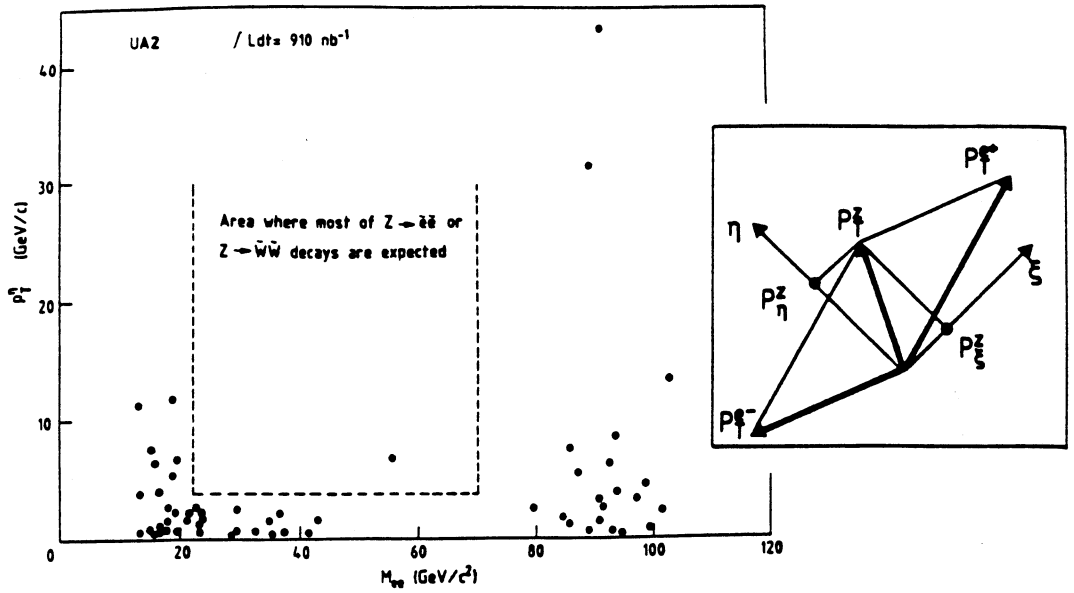

Figure 33: Distribution of Di-electron Candidates from UA2

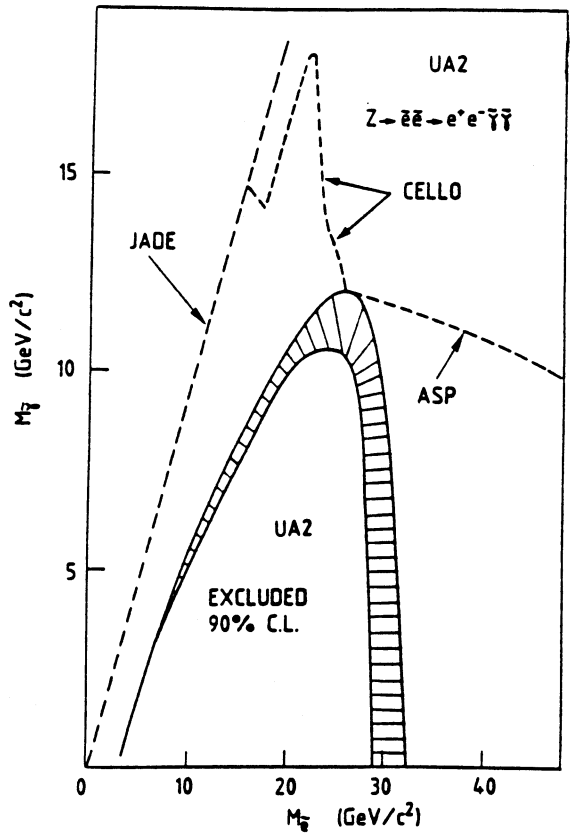

Figure 34: Confidence Limits from UA2 for the Selectron Mass

8.3.4 Results from e^+e^- Experiments

There are many results from e^+e^-, all of which show no indication of SUSY. Limits have been derived for all manner of processes and under different hypotheses for the LSP. It would be beyond the scope of this discussion to review all the results; instead a selection of some of the results concerning sleptons are presented.

Smuons

Smuons can be produced only in pairs through virtual photons. The corresponding limits are therefore bounded by the beam energy, and in practice lie just below it. If $\tilde{m}_\mu > \tilde{m}_\gamma$, then each $\tilde{\mu}$ decays to a $\tilde{\gamma}$ and a muon, leading to an acoplanar di-muon pair. For $\tilde{m}_\mu < \tilde{m}_\gamma$ with a stable $\tilde{\mu}$, at lower $\tilde{m}_\mu$, the agreement between the theoretical differential cross-section for muon pair production and the data excludes $\tilde{\mu}$ production. At higher masses, the absence of slow minimum ionising particles excludes the production. Limits from the Jade Collaboration [79] are shown in figure 35.

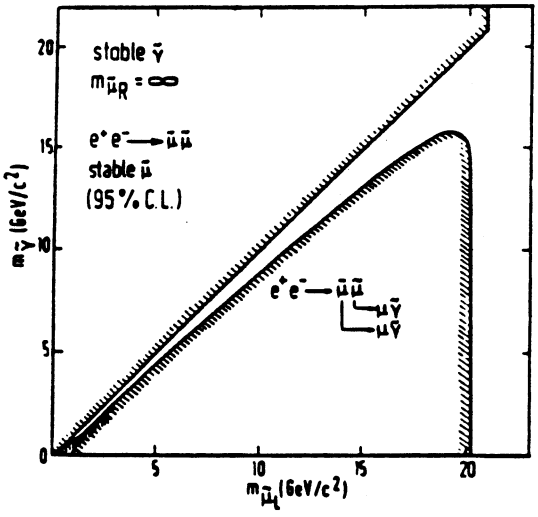

Figure 35: Confidence Limits from JADE for the Smuon Mass

Selectrons

The results for selectrons can be treated in a similar manner to those for smuons. However, in addition, there are virtual processes which allow the limits to be extended considerably beyond the beam energy.

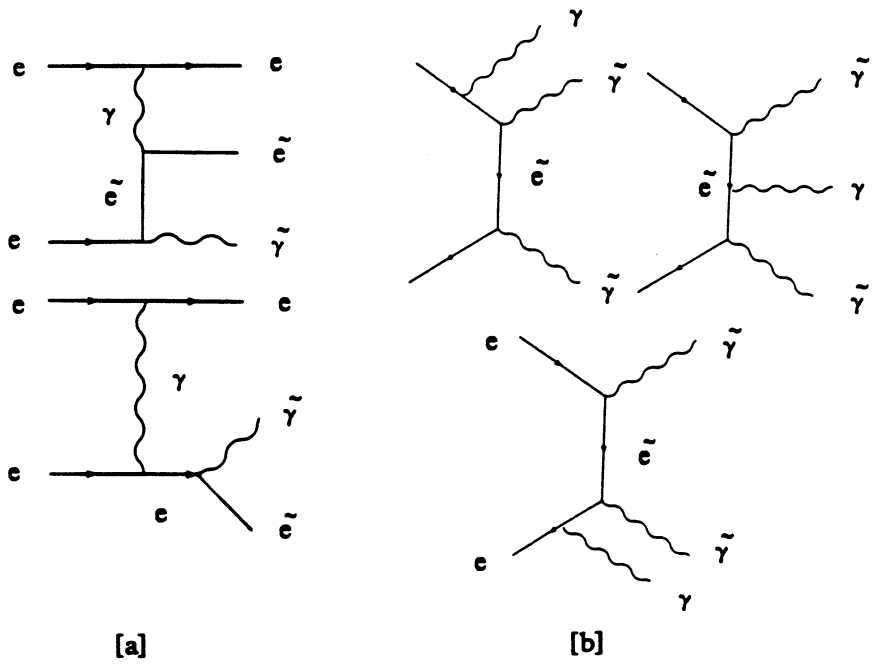

Figure 36: Diagrams Involving Virtual Selectrons

In the processes where there is one real selectron in the final state (figure 36 [a]), the electron which radiates the photon is hardly perturbed and is lost down the beam pipe, while the selectron decays to an observed electron and missing energy. Where there are no final state selectrons (figure 36 [b]), the signature is a single photon with missing energy. This process extends the sensitivity to $\tilde{m}_e$ beyond those from the processes of figure [a]. The best limits come from the single photon searches made by the CELLO [88], MAC [89], and ASP [90] Collaborations which report zero, one and one events respectively. The expected backgrounds from $e^+e^- \rightarrow \gamma\nu\bar{\nu}$ are of the order of 0.7, 1.1 and 2.2 events respectively. The limits are presented in figure 37. The 'best' limit comes from ASP, who find $\tilde{m}_e > 66$ GeV/c^2 at 90% ($\tilde{m}_\gamma = 0$ with degenerate $\tilde{e}_L$ and $\tilde{e}_R$).

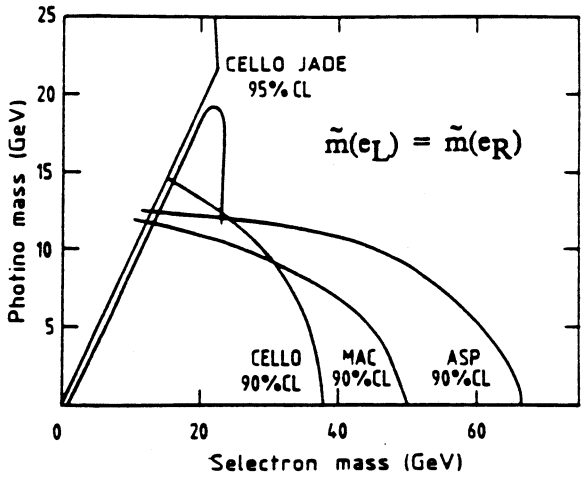

Figure 37: Confidence Limits from e^+e^- for the Selectron Mass

8.4 Cross-section for $W \rightarrow \tilde{e}\tilde{\nu}$

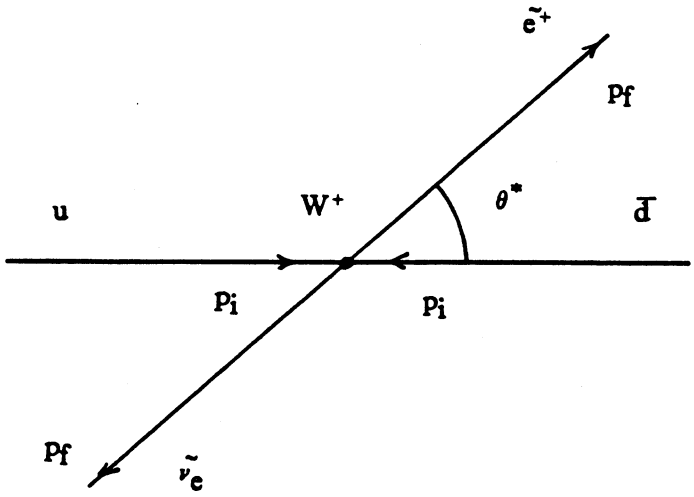

Figure 38: Decay of W to Selectron and Sneutrino

In preparation for the analysis of the next chapter, we examine the decay $W \to \tilde{e}\tilde{\nu}$. The form of the differential cross-section relative to $W \to e\nu$ is readily understood.

a. The decay matrix is proportional to the product of the W polarisation vector, W_μ, and the vector current of the sleptons, which is proportional to the slepton four-momentum, p^μ. As the spin of the W is aligned along the beam direction, its polarisation is transverse, so that summing over the polarisation states picks up the transverse component of p^μ. Therefore the matrix element is

$$\mathcal{M} \sim W_\mu p^\mu \sim p_t = p \sin\theta^* \tag{8.7}$$

b. Spin factors give a term $(2J_f + 1)$, which is 1 for the decay to scalars, and 2 for the fermion decay.

c. Phase space gives a factor $\kappa = p(\tilde{m})/p(\tilde{m}=0)$.

Putting all these things together, we deduce that the angular distribution is

$$\sigma(\Omega) \sim \sin^2\theta^* \tag{8.9}$$

and the rate is given by

$$\sigma(W \to \tilde{e}\tilde{\nu})/\sigma(W \to e\nu) = {}^1/_2\,(\kappa)^2\kappa = {}^1/_2\,\kappa^3 \tag{8.10}$$

where $\kappa^2 = [1-(\mu_e-\mu_\nu)^2] \times [1-(\mu_e+\mu_\nu)^2]$, with $\mu \equiv \tilde{m}/m_W$. The full calculation of the matrix element is performed in appendix D.

The angular distribution should be compared with the V−A distribution arising in standard leptonic decays of the W. Further, the fact that, for the proton, the u quark structure function is harder than that of the d, means that the W tends to acquire a longitudinal boost in the reverse direction to the V−A electron decay asymmetry, so that the angular distribution of selectrons in the lab frame shows the reverse asymmetry compared with standard electron decays. The subsequent decay of the selectron and boost from the W tend to force the angular distribution of the electrons to even higher $|\cos\theta|$.

The above results also hold for the decay $W \rightarrow \tilde{\mu}\tilde{\nu}$. In addition, they hold for the sleptonic decays of the Z, but the different 'chirality' states of the sleptons ($\tilde{e}_L$ or $\tilde{e}_R$, and $\tilde{\mu}_L$ or $\tilde{\mu}_R$) must be treated separately if they are not degenerate. The left and right handed couplings of the sleptons are exactly the same as those of the corresponding leptons.

9. DESPERATELY SEEKING SUSY

In the previous chapter, we reviewed some of the theoretical concepts of SUSY. In this chapter, the search for sleptonic[34] decays of the W and Z bosons is discussed. After a short discussion of where to look for SUSY decays, and the potential backgrounds, a simple Monte-Carlo program is discussed. Initially this Monte-Carlo is used to understand how to test the data for events resulting from leptonic decays of supersymmetric particles. Next, the data selection is discussed, and the distributions are tested to see if they are compatible with known processes, as predicted by the ISAJET Monte-Carlo. No clear evidence for SUSY is found, and the agreement between the data and the predictions is used to set limits on the masses of the supersymmetric particles. The derivation of these limits is discussed in the second half of this chapter. The shapes of the distributions expected for various slepton and sneutrino masses are derived with the simple Monte-Carlo, while the normalisation is obtained from calculations with a supersymmetric version of ISAJET.

In the following analysis, we have not assumed the degeneracy of the left-handed slepton and sneutrino, as suggested in some models.[35] The shape of the lepton spectrum from the decay of the slepton is in principle sensitive to the difference between a heavy $\tilde{l}$ with a light $\tilde{\nu}$, and a light $\tilde{l}$ with a heavy $\tilde{\nu}$. However, in the decay $Z \to \tilde{l}\tilde{l}$, there is little sensitivity to the distinction between $\tilde{l}_L$ and $\tilde{l}_R$ - both have a $\sin^2\theta^*$ distribution, and the only distinction comes from the different rates for the left and right handed decays, which occur in the ratio 0.6 to 0.4 [75]. Therefore, as in reference [75], the left and right handed sleptons are treated as degenerate, even though this is not generally expected.

9.1 Where to look for SUSY, and Potential Backgrounds

To investigate the processes

$$W \to \tilde{l}\tilde{\nu} \text{ and } Z \to \tilde{l}\tilde{l} \tag{9.1}$$

---

[34] We will use '(s)lepton' to refer collectively to the (scalar) electron and (scalar) muon, which will be denoted by 'l' for the leptons, and $\tilde{l}$ for the sleptons.

[35] In the absence of 'D-terms' [80], $\tilde{l}_L$ and $\tilde{\nu}_L$ are degenerate in mass.

with the subsequent decay $\tilde{l} \rightarrow l\,\tilde{\gamma}$, we are interested in events with properties similar to the observed decays:

$$W \rightarrow l\,\nu \text{ and } Z \rightarrow l\,l \tag{9.2}$$

where frequently the virtual photon processes will be implicitly included in the processes labelled as 'Z' decays. The leptons from the SUSY decays should have a relatively large p_t, although this will be less than that of leptons from the direct decays. In both cases, the leptons should be isolated. In the SUSY decays of the W, there will be substantial missing transverse energy ($\not{E}_t$) and there may be some in the Z decays. The obvious place to search for these new processes is in data similar to that used for our search for standard W and Z events. To maximise our sensitivity, it is desirable to relax some of the cuts used in selecting standard W and Z candidates. However, this must not be done at the cost of introducing substantial proportions of other backgrounds. The major contributions to such data sets are shown in table 19.

Table 19: Backgrounds to SUSY processes

	SUSY processes	
	$W \rightarrow \tilde{l}\tilde{\nu}$	$Z \rightarrow \tilde{l}\tilde{l}$
	backgrounds	
electron	$W \rightarrow e\,\nu$	$Z \rightarrow e\,e$
		$\gamma \rightarrow e\,e$
	$W \rightarrow \tau\,\nu$	$Z \rightarrow \tau\,\tau$
	jet fluc.	
muon	$W \rightarrow \mu\,\nu$	$Z \rightarrow \mu\,\mu$
		$\gamma \rightarrow \mu\,\mu$
	$W \rightarrow \tau\,\nu$	$Z \rightarrow \tau\,\tau$

The contribution labelled as 'jet fluc.' is the background which typically arises from two-jet events, resulting from QCD processes. Occasionally, one of the jets fluctuates so that it contains at least one high energy neutral particle (π^0's) and a fast charged particle (π^+ or π^-), and can fake an electron in

the CD and calorimeter. In addition, the response of the calorimetry may be such that the jet energies are not well measured, and a significant amount of missing energy is recorded.

Even in the presence of SUSY it is anticipated that most of our data will be described by standard W/Z decays. There are, in addition, a number of negligible backgrounds, which are discussed where appropriate. The effect of ignoring any of the remaining backgrounds will be to gain apparent sensitivity to new processes or will result in conservative limits, since the other backgrounds lie in a similar kinematic region (i.e. at lower p_t) to that populated by SUSY decays. The decay background to the muonic channels is less than about one event, and is ignored. Due to the isolation requirements, the contributions from heavy quark decays are negligible. We estimate that the background from $b\bar{b}$ and $c\bar{c}$ to the $W\rightarrow e\tilde{\nu}$ events is about 0.5 events (the selection of events is discussed in section 9.4); while the background to the $Z\rightarrow \tilde{e}\tilde{e}$ events is about 0.2 events. The implications of possible top quark decays are discussed in section 8.

9.2 SUSYMC – a Simple Monte-Carlo

From the start, it was very clear that there would be great demand on Monte-Carlo simulation. Testing distributions for SUSY is especially demanding because the uncertainty in the mass parameters means that tests should be made at a variety of different SUSY masses. It was envisaged that a fast Monte-Carlo program capable of producing high statistics would be tremendously helpful for this study. Such a program would be invaluable for:

- Understanding the physics of SUSY.
- Examining the effect of the cuts applied in the data selection.
- Choosing the best variables to use for the search.
- Obtaining the differential cross-section for SUSY decays.
- Estimating the sensitivity.

For these reasons, and in view of the simplicity of the mechanism for W/Z production and decay, a simple program called SUSYMC was written. (It turned out that this program was very useful for understanding the structure function of the u and d quarks sampled by the W, and also the kinematic properties of a low mass W-like boson.)

The starting point of the program was the simple generator used in the W mass fitting. The basic aims were to be able to generate event parameters or differential cross-section distributions for W and Z/γ decays to leptons, sleptons and tau leptons, with their subsequent decay to electrons or muons. The program consists of several distinct parts which are described below.

9.2.1 Generating W/Z Bosons

W Bosons

W's are generated with a Breit-Wigner distribution with a central mass of 83.4 GeV/c^2 (as used by ISAJET) and width 2.8 GeV (the method for this is described in appendix E). Since the W is produced with an essentially unique mass (ignoring its width), we can construct a simple relationship involving the values of the momenta, p_u and p_d, of the quarks which form the W. In the simple parton model, the quarks travel along the beam directions, so that the requirement that they should form an on-mass-shell W is

$$m_w^2 = 4p_u p_d \tag{9.3}$$

The longitudinal motion of the W is $p_w = \pm(p_u - p_d)$, where the sign depends on the charge of the W. Using equation (9.3) to eliminate either p_u or p_d, it is possible to express the other momentum as a function of p_w, and therefore the structure function effects may be described solely in terms of p_w. Using the structure functions of Eichten et al (with $\Lambda = 0.2$ GeV) in the context of the ISAJET Monte-Carlo, we find that the longitudinal motion is well described by a Gaussian of width 65 GeV/c and with an offset in Qp_w of 16 GeV/c - where Q is the charge of the W. The transverse motion, which to first order is independent of p_w, is parameterised from the calculations of Altarelli at al [91].

Z Bosons

The generation of Z's is considerably more complicated if we consider the full Z-γ electroweak interference. This means that there is no unique mass for the intermediate state, and the simplicity of equation (9.3) is lost. The approach taken is to 'collide' incoming quarks and weight events by the cross-section.

Very simple structure functions have been used [48]. For the valence quarks, a single function is used for u and d quarks:

$$xv(x) \sim \sqrt{x}(1-x)^3$$

and for the sea quarks:

$$xs(x) \sim (1-x)^7$$

with the following sum rules:

$$\int v(x)dx = 3$$

and

$$\int xv(x)dx = 40\%, \ \int xs(x)dx = 10\%$$

with the remaining 50% of proton momentum being carried by the gluons. The effective structure function arising from the possible quark combinations sampled by the Z is approximately $xf(x) = x(v(x)+0.3s(x))$. It should be emphasised that for the production of Z's, the form of the sea quark structure function is not very important since their contribution to the cross-section is only a few percent, and for the production of $\tilde{l}\tilde{l}$, the main contribution comes from valence quarks interacting at the Z resonance. The quark momenta are generated according to a $(1-x)^3$ distribution and are then weighted to the distribution f(x).

At this stage, the quark and lepton chiralities are chosen at random. The p_t of the Z is generated in a manner similar to that of the W; however, the p_t is scaled in proportion to the mass of the Z.

Subsequently, the events are weighted to the Z cross-section [44] at the parton centre of mass energy, $\sqrt{s}$:

$$\sigma(s) \sim s^{-1}|Q_q + c_q c_l r|^2 \tag{9.4}$$

where

$$r = \sqrt{2}Gm_Z^2/(s - m_Z^2 + im_Z\Gamma_Z) \times s/e^2 \tag{9.5}$$

and c_q and c_l are the quark and lepton couplings, respectively, and Q_q is the quark charge.

Since the most important contribution comes from the Z resonance, events where the mass lies within $3\Gamma_Z$ of the pole are preferentially used to increase the useful statistics, and the event weights are adjusted accordingly.

The production cross-section is essentially independent of the decay modes. The event yields are, however, dependent on the branching ratios, which are taken as $1:1:{}^1/_2\kappa^3$ (see section 8.4 for definition of κ) for $W\to l\nu:W\to\tau\nu:W\to\tilde{l}\tilde{\nu}$ and for $Z\to ll:Z\to\tau\tau:Z\to\tilde{l}\tilde{l}$, with branching ratios of $17^1/_2\%$ for the τ to decay to either an electron or a muon.

9.2.2 Decays of W/Z Bosons

Direct Decays

W's are forced to decay with the V−A asymmetry in the centre of mass frame, that is with a distribution $(1+Q\cos\theta^*)^2$. The leptons are then boosted into the lab frame. A similar method is used for the Z's. However, the angular distribution of the decay leptons is a mixture of $(1+Q\cos\theta^*)^2$ and $(1-Q\cos\theta^*)^2$ in nearly equal proportions, leading to a distribution which is almost symmetric.

Tau decays

The decay of a W or Z to tau leptons proceeds precisely as for the decay to electrons or muons (with a slight reduction in the centre of mass momentum). The subsequent decay of the tau is very complicated because of the polarisation effects. A simplified model is used where m_τ is neglected with respect to the W or Z masses, so that the tau is not depolarised. The subsequent decay of the tau is weighted according to the distribution [92]:

$$2\varepsilon^2(3-2\varepsilon) \times \{1-\mathcal{H}(1-2\varepsilon)/(3-2\varepsilon)\cos\theta^*\} \tag{9.6}$$

where the decay leptons are treated as being massless, ε is the energy of the daughter lepton as a fraction of the maximum possible, and θ^* is the direction of the charged lepton in the tau rest frame with respect to the direction of the tau in the W rest frame. $\mathcal{H}$ is a factor which describes the helicity of the tau, and is $+1$ for W decays. For the W's, this distribution peaks for $\varepsilon = 1$ and $\cos\theta^* = +1$, which tends to give rise to a harder lepton spectrum than would be expected from a decay with a structureless matrix element. This point is important, and is discussed later.

SUSY Decays

For both W and Z decays to sleptons, the angular distribution is symmetric and given by $\sin^2\theta^*$ in the centre of mass (see chapter 8). The sleptons are then boosted into the lab frame. Subsequently, the sleptons are decayed in their rest frame to leptons and photinos with an isotropic distribution.

9.2.3 Simulation of the Real Event and Event Selection

Smearing

The electron energies are smeared according to the following parameterisation of the resolution:

$$\sigma(E) = 23\%\sqrt{E} \tag{9.7}$$

The CD momentum is smeared according to

$$\sigma(1/p) = f(\lambda,\Phi) \tag{9.8}$$

where the angles λ and Φ are defined in chapter 2. This parameterisation is obtained separately for electrons and muons (the errors on electron tracks tend to be greater, due to the less stringent track quality cuts). In addition to the W or Z produced in an event, there are other particles which emerge from the breakup of the proton and antiproton, and some particles may appear in one or more jets recoiling against the IVB. All the particles other than those originating from the IVB are described as the 'rest of the event'. For our purposes, the only characteristic of the 'rest of the event' which is important is the summed vector E_t. While none of these extra particles are simulated, the vector E_t of the 'rest of the event' can be found from the reversed vector p_t of the W or Z. This is then smeared according to its nominal resolution. For the di-electron events, it is very important to have a reasonable parameterisation of this quantity, as it affects the resolution of the missing energy in an event. Therefore, the $Z \rightarrow ee$ data itself has been used to provide this parameterisation.

Acceptance and Cuts

The electron acceptance and trigger efficiency is taken as being 100% - in practice, any global effects are removed by the normalisation, as discussed in section 9.6. Further, when used to compare distributions from standard processes with those expected from SUSY, and where both are obtained from SUSYMC, many of the simplifications should cancel out. The muon acceptance is simulated using a simple geometrical description of the muon chambers and the approximation that the muons from IVB decays travel in almost straight lines.

E_t and p_t cuts are applied precisely as for the real data - these will be described in section 9.4. To simulate the track quality cuts, which heavily depopulate the horizontal region, a horizontal ϕ cut is made which removes between $\pm 15°$ and $\pm 30°$ of the horizontal region, being largest at the centre. There is also a $\pm 6°$ ϕ cut in the vertical plane for the electrons alone.

Finally, the event parameters for each generated event are constructed precisely as for the real data events.

9.3 Choice of Variables

Classes of events with different features (for example, masses and spins of particles) can, in principle, be distinguished by examining the distributions of events in the same variables. The number of these defines the maximum number of independent quantities which can be measured and allow distinction of the different event types. In practice, it is more usual that we have only indirect measures of these features, and there is no unique nor totally obvious set of variables to use. In principle, all useful measurements can be used. However, since the derivation of the pdf's inevitably requires Monte-Carlo techniques, it is difficult to estimate these distributions in many dimensions.

The goal is to choose a small set of variables which provide good sensitivity to the different processes being analysed. Fortunately, in simple situations it is often possible to find a few variables which are fairly closely correlated to the distinguishing features. Using fewer variables than there are distinguishing features leads to a loss of sensitivity, while using many more may not be a great advantage due to the correlations. Further, using many variables leads to greater complications, in particular, it becomes difficult to visualise multidimensional pdf's, and the statistical fluctuations in the estimated pdf's can become substantial.

9.3.1 $W \to \tilde{l}\tilde{\nu}$

The characteristics of this decay, as compared to $W \to l\nu$ are:

i. The production of spinless particles - this gives rise to an angular distribution which is different from the $V-A$ distribution.

ii. The charged slepton decays to a lepton and a photino which is not detected - this results in a lepton with less energy than the slepton.

iii. The decaying slepton may have significant mass - this affects the branching ratio of the SUSY decay of the W. Also, the hardness of the lepton p_t spectrum is sensitive to $\tilde{m}_l$, and hence the number of events passing the cuts is affected. However, since the masses are unknown, the experimental distributions can be used to determine them, if the SUSY decays can be detected.

So we can identify two useful features of the decay $W \to l\tilde{\nu}$, namely the first two above. The ideal variables to use would be $Q\cos\theta^*$, which measures the charge-angular distribution in the centre of mass of the W, and M_t, which is a measure of the momentum of the lepton. In a simplified picture, where the W is produced with zero p_t, then M_t is $2p\sin\theta^*$ and one finds that $W \to l\nu$ events lie on an ellipse in the $(Q\cos\theta^*, M_t)$ plane, while $W \to l\tilde{\nu}$ events lie inside the ellipse, with a different angular distribution. Unfortunately, we do not actually measure $\cos\theta^*$ directly, since we are unable to measure the neutrino longitudinal momentum and hence cannot deduce the W rest frame. By imposing the mass constraint - which explicitly imposes the W mass on the system, we can estimate $\cos\theta^*$. However, the use of the mass constraint effectively gives

$$\cos\theta^* = \sqrt{(m_W{}^2 - M_t{}^2)}/m_W \tag{9.9}$$

and this forces all events to lie on one ellipse !

We note in the simplified description of the lepton-neutrino event, we measure only two useful quantities: $\cos\theta$ and p of the lepton. In chapter 4, it is shown that the likelihood is invariant to a change of variables. Therefore, the sensitivity which we can obtain is independent of how we use these two measurements. Therefore, the variables we choose to use are $Q\cos\theta$ and M_t. The charge is determined by the CD with a fractional error which grows with p and hence M_t. However, since we are interested in distinguishing the processes at lower M_t, the charge resolution is satisfactory for charge measurement. For practical reasons, as discussed in chapter 6, we use $M_t{}^{-1}$ for the $W \to \tilde{\mu}\tilde{\nu}$ search.

There are other pairs of variables which we could use, but since they are closely related to the two we have chosen, there is no statistical gain. Further, since these two variables are easily visualised and the location of various backgrounds is readily understood, it is easier to identify problems with $(Q\cos\theta, M_t)$ than with other choices for the variables.

Finally, since the pdf's cannot be generated continuously by Monte-Carlo methods, it is necessary to evaluate them in bins. It is important to retain reasonable statistics in each bin, while not losing the shape of the distribution. Also, care must be taken not to lose data events outside the region of the

binning and to avoid data events falling in bins in such a way that they receive 'uncharacteristic' estimates of the pdf, which may arise when the pdf is a rapidly falling function or is dominated by statistical errors from the Monte-Carlo. With these points in mind, a grid of ten by ten bins was chosen, with Qcosθ running from -1 to $+1$ and with M_t (M_t^{-1}) between 0 to 120 GeV/c^2 (0 to 0.04 $GeV^{-1}c^2$) for the electrons (muons).

9.3.2 $Z \rightarrow \tilde{l}\tilde{l}$

This process was first suggested as a good place to look for SUSY by Cabibbo et al [93]. We consider this decay in a similar manner to the above. The characteristics are as for $W \rightarrow l\tilde{\nu}$, although there are now two sleptons which decay to charged leptons. The measurable quantities in a simple description are:

i. the momentum p_1 and angle θ_1 of the first lepton,

ii. the momentum p_2 and angle θ_2 of the second lepton,

iii. the azimuthal angle between the leptons.

Possible variables which might be considered are:

a. M (or M^{-1} for muons) : leptonic decays of the Z should appear as a clear resonance, whereas the SUSY decays should have a smooth distribution below the pole.

b. $\not{E}_t$: some SUSY decays should have considerable missing energy.

c. ω : $\omega \equiv 180° - \Delta\phi$ (see figure 39). Leptons from the decays of sleptons will not, in general, be back to back in the transverse plane due to the emission of photinos. This contrasts with the back to back leptons from the direct decay of Z's (with low p_t).

d. $\not{E}_t(\perp)$: since there is missing energy in a SUSY event and the leptons are not back to back, it is to be expected that the transverse missing energy will have a component along the bisector of the di-leptons (see figure 39). This is especially useful if there is substantial smearing of the leptons causing significant amounts of fake missing energy along the lines of the leptons.

The last three are all characteristics of the missing energy, and the last two are highly correlated.

The perpendicular component of missing energy (see figure 39), $\not\!\!E_t(\perp)$, and the difference in azimuthal angle, ω, have signs which are defined as positive if the neutrino lies on the same side as the lepton pair. This means that for ordinary leptonic Z decays where there is some recoil (so that the leptons are not back to back) and the lepton momenta are mismeasured, then when the di-lepton mass is reconstructed too low, $\not\!\!E_t(\perp)$ and ω are positive, whereas for SUSY decays with similar topologies, these quantities are negative.

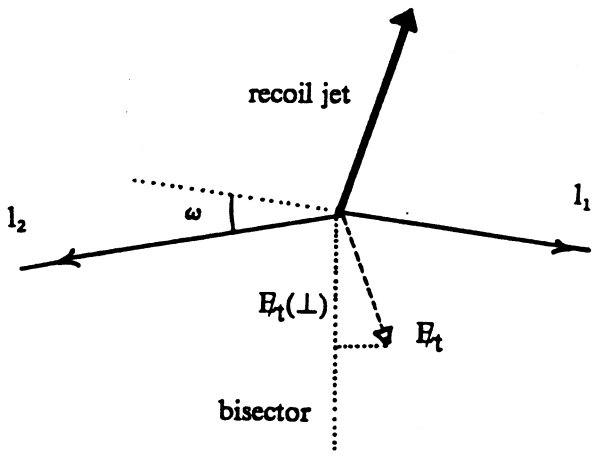

Figure 39: Definition of ω and $\not\!\!E_t(\perp)$

For the electrons, the mass affords a good distinction between $Z \to \tilde{e}\tilde{e}$ and $Z \to ee$. However, there is little distinction between Drell-Yan and $Z \to \tau\tau$ and SUSY in just the mass variable. Therefore M is used in a trivial way to distinguish between $Z \to \tilde{e}\tilde{e}$ and $Z \to ee$. Consequently, we choose a further pair of variables to give us sensitivity below the Z resonance: either $(M, \not\!\!E_t, \omega)$ or $(M, \not\!\!E_t, \not\!\!E_t(\perp))$.

For the muons, it makes little sense to use $\not\!\!E_t$ due to the substantial smearing on the measurement of p from the CD for standard muonic Z decays. So for the di-muon search, it is appropriate to use the variables (M^{-1}, ω) or $(M^{-1}, \not\!\!E_t(\perp))$.

9.3.3 Bayesian Risks

Ideally, to choose the best set of variables, one would estimate which variables would give the most significant estimate of the signal or the strongest confidence limits. This is not simple to do. Alternatively, we can seek a measure of how well different sets of variables distinguish between signal and background. One such measure is the Bayesian [36] risk which estimates the overlap of two distributions.

Given two density functions s (the signal) and b (the background) defined in some space $\{\Gamma\}$, with the correct relative normalisation and such that the normalisation of the sum is unity, the Bayesian risk is usually defined as the overlap:

$$\mathfrak{R}^b = \int d\Gamma \min(s,b) \tag{9.10}$$

This can never exceed $\int d\Gamma s$ or $\int d\Gamma b$, and here, it is more useful to normalise to the signal:

$$\mathfrak{R} = \mathfrak{R}^b \div \int d\Gamma s \tag{9.11}$$

$\mathfrak{R}$ varies between 0 (no overlap) and 1 (complete overlap). The latter case corresponds to a situation where on an event by event basis, one would be forced to conclude that it was more likely that each event was a background event - hence the 'risk'.

The risk has been evaluated in the context of SUSYMC using distributions binned in a grid 50 by 50 or 25 by 25. It is necessary to use fine bins to obtain a good approximation to the continuous distributions, however it is important to avoid statistical fluctuations within bins. The risks have been evaluated for several sets of variables using the distributions for Z(and γ)$\rightarrow \tilde{l}\,\tilde{l}$ and those for Z(and γ)$\rightarrow$l l and $\tau\tau$. This has been done for $\tilde{m}_l$ = 25 GeV/c^2 and $\tilde{m}_\gamma$ = 0 GeV/c^2. Note that the best choice of variables to obtain sensitivity to one SUSY mass combination may not represent the best choice at some other mass combination, so the values chosen are in the region of our previous limits. For the electrons, since we will probe the distribution in 3-D and we are interested in events well below the Z resonance, the mass variable is ignored, but a mass cut of 75 GeV/c^2 is used to remove events coming from the resonance.

Table 20: Bayesian Risk for Various Variables for Di-leptons

		Risk (%)
e	{ $\not{E}_t$ vs ω	31 ⇐ best
	{ $\not{E}_t$ vs $\not{E}_t(\perp)$	36
	{ M vs $\not{E}_t$	40
μ	{ M vs ω	43
	{ M vs $\not{E}_t(\perp)$	32 ⇐ best

For $Z \to \tilde{e}\tilde{e}$, $(M, \not{E}_t, \omega)$ appear to be the best variables, $\not{E}_t(\perp)$ seems less useful due to its correlation with $\not{E}_t$. For $Z \to \tilde{\mu}\tilde{\mu}$, $(M, \not{E}_t(\perp))$ appear to be the best pair. Due to the poor resolution giving rise to large fluctuations in the reconstructed missing energy along the line of the muons, $\not{E}_t$ is not so useful. Which variable is favoured when comparing $\not{E}_t(\perp)$ and ω, depends on whether the smearing of the 'rest of the event' or the effect of the p_t of the Z dominates. It appears that the p_t of the Z is sufficiently large to give the $Z \to \mu\mu$ events a significant spread in ω causing them to overlap the SUSY signal.

Due to the sharpness of the ω distribution in the allowed range $[-180°, +180°]$, it is quite difficult to reproduce the shape with a binned pdf. For numerical convenience, the variable $\sqrt{\omega}$ is used. This introduces a Jacobian $2\sqrt{\omega}$ which makes the distribution easier to handle with bins.

For the electrons, M is coarsely binned in the bins $0-40$, $40-80$ and $80-120$, the last bin containing all of the $Z \to ee$ candidates. $\not{E}_t$ is binned in 6 bins in the range [0,60], while $\sqrt{\omega}$ is binned in 20 bins in the range $[-12, +12]$ - which corresponds to $\pm 144°$. For the di-muons, M^{-1} is binned in 10 bins in the range [0,0.05] and $\not{E}_t(\perp)$ is binned in 10 bins in the range $[-55,15]$ - we use an asymmetric interval since $Z \to \mu\mu$ will tend to populate the central region at lower masses (and the negative side at higher masses), while the SUSY decays will predominantly populate the negative region.

9.4 Selection of Events

9.4.1 $W \to \widetilde{e\nu}$

The selection of events which has been used for this process is the standard UA1 selection which was made for $W \to e\nu$ [24] and is described below. Note that in the following, a distinction is frequently made between the energy of particles determined by the calorimetry and the energy measured in the CD. The former is usually referred to as the 'energy' E, while the latter is referred to as the 'momentum', p. In the case of a single electron, these are different measures of the same quantity - the rest mass is absolutely insignificant.

1. Electron energy: we require an electromagnetic cluster in the Gondolas or Bouchons of $E_t > 15$ GeV.
2. Cluster validation: to ensure reliable reconstruction of the electron energy, we demand that the summed p_t of all tracks, other than the electron candidate, entering the calorimeter cell containing the cluster is < 3 GeV/c and that the centroids of the samplings are consistent with a shower produced by a single electron.
3. Track validation: the CD track identified as belonging to the electron candidate should have $p_t > 7$ GeV/c or be within 3 standard deviations of 15 GeV/c. Further, it should include > 20 points and have a projected length (in the x-y plane) of > 30 cm.
4. Isolation: to exclude jet fluctuation background and remove heavy flavour contamination, we demand that
    a. in a cone of $\Delta R = 0.4$, Σp_t from all other tracks $< 10\%$ of the E_t of the electron cluster, and the hadronic energy is $< 10\%$ of the total calorimetric energy;
    b. in a cone of $\Delta R = 0.7$, Σp_t from all other tracks < 3 GeV/c, and ΣE_t, excluding the electron cluster, < 3.2 GeV.
5. Electromagnetic shape: we require that the energy deposition in the four samplings of the electromagnetic calorimeter and the hadronic cells immediately behind the cluster should have a longitudinal profile which is compatible with results found in an electron test beam.

6. Neutrino energy: finally we demand that the missing transverse energy should be in excess of 15 GeV. Events where the electron candidate is within 15° of the vertical are removed if there is a jet (E_t > 7.5 GeV) also within 15° of the vertical, since such topologies are subject to fake neutrinos caused by the loss of particles through the crack in the calorimetry.
7. Transverse mass: a cut was made at 15 GeV/c^2 to remove one very low transverse mass event which was consistent with being a jet fluctuation.

This selection yields 290 $W \rightarrow e\nu$ candidates. Since these data are compared with ISAJET Monte-Carlo data which have a 10 GeV/c cut[36] on the CD track, the same cut was applied to the data, leaving 275 events.

9.4.2 $Z \rightarrow \tilde{e}\tilde{e}$

The standard UA1 $Z \rightarrow ee$ selection [86] is inappropriate for this search due to a 70 GeV/c^2 mass cut which removes the sensitivity to SUSY. Instead, we have used the same selection, but without the mass cut. The cuts applied to obtain the di-electrons are:

1. There must be one electromagnetic cluster (E_t > 15 GeV) which passes the electron W cuts, with the exception of the requirement of a CD track in regions of poor CD acceptance.
2. A second cluster is required with E_t > 8 GeV. We demand that this pass cuts similar to those of the first cluster, but with relaxed isolation and technical quality.

This selection is available only for the $\sqrt{s}$ = 630 GeV data and yields an initial sample of 60 events. The mass spectrum of these events is shown in figure 40.

Inspection of these events on the Megatek revealed that for most of the low mass events, the electrons were far from isolated and appeared compatible with jet fluctuation events. Further, many of these lower energy electromagnetic clusters did not have fast CD tracks pointing to them. Since we expect that the general features of $Z \rightarrow \tilde{e}\tilde{e}$ events will be similar to those of $Z \rightarrow ee$ events, apart from the magnitude and angular distribution of the electron momentum vectors, we can use the latter as a

---

[36] The ISAJET preselection was made for the top quark search, which had a more stringent CD track requirement.

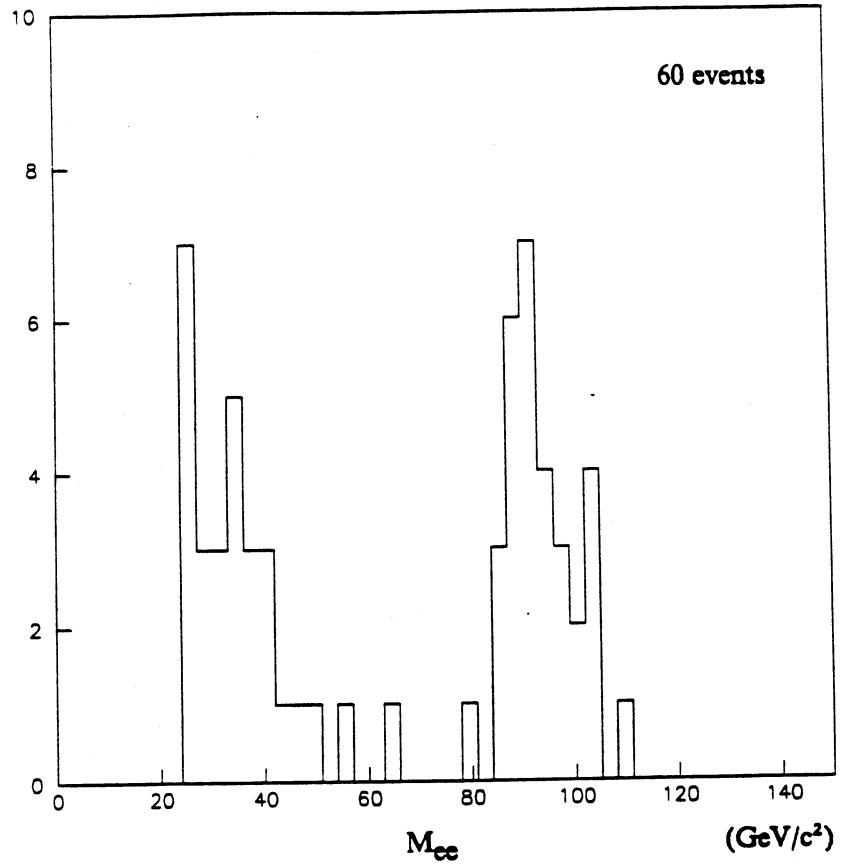

Figure 40: Initial Di-electron Mass Spectrum

control sample for choosing appropriate cuts with which to search for the former. Therefore, further cuts have been applied to the data which retain as many $Z \rightarrow ee$ events as possible while, at the same time, removing the low mass events.

Since we expect that electrons from the decay $\tilde{e} \rightarrow e\tilde{\gamma}$ will have fairly fast CD tracks, a very loose cut of 2 GeV/c is made on the p_t of both electrons. The effect of this cut is seen in table 21. Non-zero losses of Z events are anticipated from events with horizontal electrons for which there is virtually no CD acceptance. Also, it is possible that an electron has a substantial bremsstrahlung which dramatically distorts the CD track and hence the reconstructed momentum.

In the decay $Z \rightarrow \tilde{e}\tilde{e} \rightarrow ee\tilde{\gamma}\tilde{\gamma}$, the electrons have opposite charges. Therefore a very loose cut to remove like sign events is made. A measure of the accuracy of the sign determination from the curvature of a CD track is provided by the quantity $p^{-1}/\sigma(p^{-1})$ - the 'number of sigma' of the measurement. Events are rejected if the charges of the two electron candidates are the same, and both tracks are measured to at least 2 sigma. With this cut, one $Z \rightarrow ee$ event is removed. Inspection on the Megatek indicates that the digitisings belonging to one of the electrons in one of the CD drift volumes are systematically displaced as a result of some slightly inaccurate calibration constants. As a result, the track is distorted and the charge incorrectly measured.

We are left with 27 known $Z \rightarrow ee$ candidates and 4 low mass events. Of the latter, three contain a pair of very isolated clusters with fast CD tracks pointing at them. The fourth is a very interesting event. It too has an isolated pair with fast CD tracks, but there is substantial missing energy and a couple of small jets found by the jet algorithm [94]. This event will be discussed in more detail in section 9.5. Finally, as for the W's, a 10 GeV/c p_t cut was applied to the highest momentum CD track - however, this did not remove any data events.

Table 21: Effects of Cuts on Di-electron Sample

	Z candidates	non-Z events
original sample	31	29
p_t cut	28	7
charge cut	27	4

9.4.3 $W \rightarrow \tilde{\mu}\tilde{\nu}$

The standard $W \rightarrow \mu\nu$ data set of 67 events from 1983, 1984 and 1985 is used. The selection of this data is described in chapter 6.

9.4.4 $Z \rightarrow \tilde{\mu}\tilde{\mu}$

The selection for di-muon events has been made in the spirit of the one used for the selection of Z candidates, described in chapter 7. However, we have returned to the inclusive muon sample[37] with 'tight' selection (see below) and performed a new di-muon selection with lower p_t and mass cuts. This has the advantage of giving access to events with lower di-muon mass, although some events are lost due to the strict cuts made in the 'tight' selection.[38]

The muon 'tight' selection is intended to select reasonable quality inclusive single-muon events, while attempting to eliminate background coming from pion and kaon decays (see chapter 6). The cuts for the 'tight' selection [95] are similar to some of those used for the $W \rightarrow \mu\nu$ selection, and are reproduced below:

1. We demand a muon chamber track with matching CD track associated to the primary vertex.
2. The chi-squared for the matching between the CD and the muon chamber track must be less than 16 for each of the 4 quantities compared (two positions and two angles).
3. The p_t of the CD track must be greater than 3 GeV/c, and it is required to be at least 40 cm long in $x-y$ and have more than 20 digitisings, with a Sadoulet chi-squared of less than 3.
4. Finally, the muon should pass all the checks to remove i) cosmic rays, ii) non-interacting hadrons, iii) shower debris and iv) π/K decays.

Starting from this selection made for the $\sqrt{s}$ = 630 GeV data, a basic di-muon selection was made. In addition to the candidate muon, a second fast track in the CD was required. The cuts applied are:

1. p_t of the first track > 10 GeV/c,
2. p_t of the second track > 10 GeV/c,
3. mass of the pair > 20 GeV/c^2,

---

[37] This sample includes all events containing at least one muon candidate.

[38] To test the feasibility of making a further selection from the events passing the 'tight' cuts, the effect of the 'tight' cuts was tested on the $Z \rightarrow \mu\mu$ candidates in their final form. It was found that all but one of the candidates passed the cuts.

4. charge of the tracks must not be the same - as for the di-electron selection,
5. very loose isolation of the muon candidates.

This selects 27 out of 8050 events and 55 out of 12032 events from the 1984 and 1985 'tight' selection data respectively (see table 22). Several of the 16 known $Z \rightarrow \mu\mu$ candidates in 1984 and 1985 were lost:

- One event was not included in the 'tight' selection as it occurred in a period of running with reversed magnetic field.
- One event occurred while the muon trigger was only partially operational and was thus excluded.
- One event was lost since the second track was not associated to the primary vertex - this was recovered 'by hand' from the $W \rightarrow \mu\nu$ selection for the $Z \rightarrow \mu\mu$ analysis.
- One event appears simply to have been lost when the 'tight' selection was made.

No additional $Z \rightarrow \mu\mu$ candidates were found.

Table 22: Percentage of Events Removed by Di-muon Cuts

	cuts					
%	1	2	3	4	5	survive
1984	90.6	8.5	0.3	0.1	0.2	0.3
1985	89.6	9.3	0.2	0.2	0.1	0.5

Subsequent cuts were applied - again the philosophy used was to keep as many $Z \rightarrow \mu\mu$ candidates as possible, while removing events of lower di-muon mass which had characteristics of events coming from sources other than Z-γ decays. The events surviving cuts 1 to 5 were scanned on the Megatek. It was found that the low mass events (70 of them) appeared to be poorly isolated; or the second muon candidate in these events had a low quality track in the CD. Therefore the following cuts were made:

6. The isolation was tightened to demand that in a cone of $\Delta R = 0.7$ $\Sigma E_t < 15$ GeV and $\Sigma p_t < 10$ GeV/c for each track.

7. If the second track was seen only in the CD, it was required that the number of digitisings > 20 or the track length > 40 cm.
8. There should be no CD track of p_t > 1 GeV/c within a cone of $\Delta R = 0.2$ around either track.
9. For tracks seen only in the CD, $\cos\theta < 0.98$.

Table 23: Events Removed by Final Di-muon Cuts

	cuts				
	6	7	8	9	survive
Z candidates	1	1	0	0	10
non-Z candidates	32	21	7	4	6
total	33	22	7	4	16

One of the Z candidates was lost due to a large neutral cluster in the Gondolas surrounding one of the muon tracks. A second was lost due to a track length of 15 cm and 18 digitisings in the CD. It had been recovered from the $W \rightarrow \mu\nu$ selection. The latter is a radiative event.

A final examination of the events revealed one cosmic ray. This was removed 'by hand'. Further, all of the events in which the second muon track was seen only in the CD were examined to check consistency with its being a muon, that is: i) minimum ionising in the calorimeters, and ii) no muon chamber hit expected since the track lies outside the geometrical acceptance. None of the events unambiguously violated these criteria. Of the 10 Z candidates, only 2 had a pair of muon chamber tracks, while 4 of the 5 non-Z candidates did.

In order to increase the statistics, the same procedure was employed in one step for the 1983 'tight' selection data. A further 2 Z candidates were selected. Of the 5 1983 candidates, the radiative event failed the isolation cuts; a second failed the track length cuts (this event was not used for the cross-section calculations); and a third event was lost when the 'tight' selection was made.

To summarise, we therefore use 17 events for the $Z \rightarrow \tilde{\mu}\tilde{\mu}$ search, 12 of which are known $Z \rightarrow \mu\mu$ candidates.

The events selected in the four categories above will be referred to as the W-e, Z-e, W-μ and Z-μ events, respectively.

9.5 Comparison of the Data with Monte-Carlo Predictions

The first question to ask is: 'Are our events compatible with expectations from known processes, or is there evidence for additional contributions, such as SUSY ?' To answer this question, Monte-Carlo events have been selected from a large Monte-Carlo production performed for the UA1 'Top' analysis. The resulting distributions are compared with those found for the data.

The Monte-Carlo production is described in appendix F. The selection was performed in precisely the same way as for the real events. Since the production was for inclusive W/Z decays, contributions from standard W and Z decays to tau's are included and should be selected with the correct proportions. The most significant additional background to W-e is from jet fluctuations. The magnitude of the contribution is estimated from the shape of the missing energy spectrum [24], while the shapes of the various distributions are deduced by looking at inclusive electron events with 10 GeV < E_t < 15 GeV, and scaling the energy to be greater than the cut. In table 24, the percentages of events expected solely from backgrounds (direct decays of IVB's to electrons or muons, decays of IVB's to tau's to electrons or muons, jet fluctuations, and Drell-Yan) are given.

In figures 41 and 42, the data are shown with the Monte-Carlo expectations (also, the SUSY predictions for $\tilde{m}_e$, $\tilde{m}_\mu$ or $\tilde{m}_\nu$ = 25 GeV/c^2 are shown as dotted). Generally the agreement is fairly good and there are no significant departures. The χ^2 probabilities for the 1-D fits are also shown in the figures - as usual, the probabilities have to be interpreted with care. The probabilities are given as percentages: the first value is calculated using the data in the denominator of the chi-squared, while the

Table 24: Contributions from Known Processes

	fraction of events (%)			
	direct	tau	jet fluc.	γ
W-e	92	6	2	–
W-μ	95	5	–	–
Z-e	77	2	–	21
Z-μ	66	1	–	33

second number, in brackets, uses the theoretical estimate. More meaningful fit probabilities will be derived in the next section.

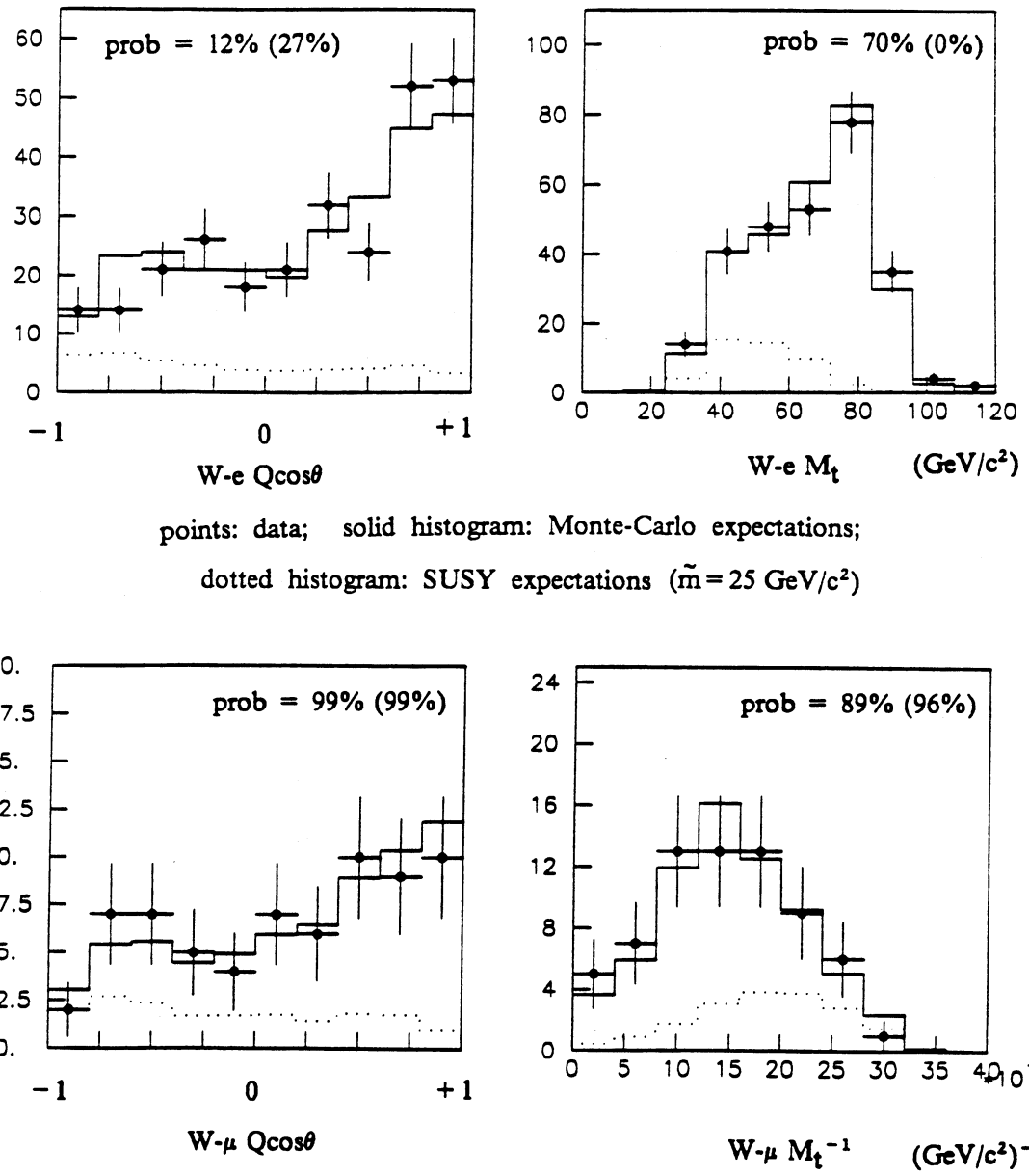

Figure 41: 1-D Distributions for Data, with Monte-Carlo Predictions

9.5.1 Methods for 2-Dimensional Tests

Using multidimensional distributions gives greater sensitivity to new processes and therefore it is important to test the distributions in several variables, in addition to their projections.

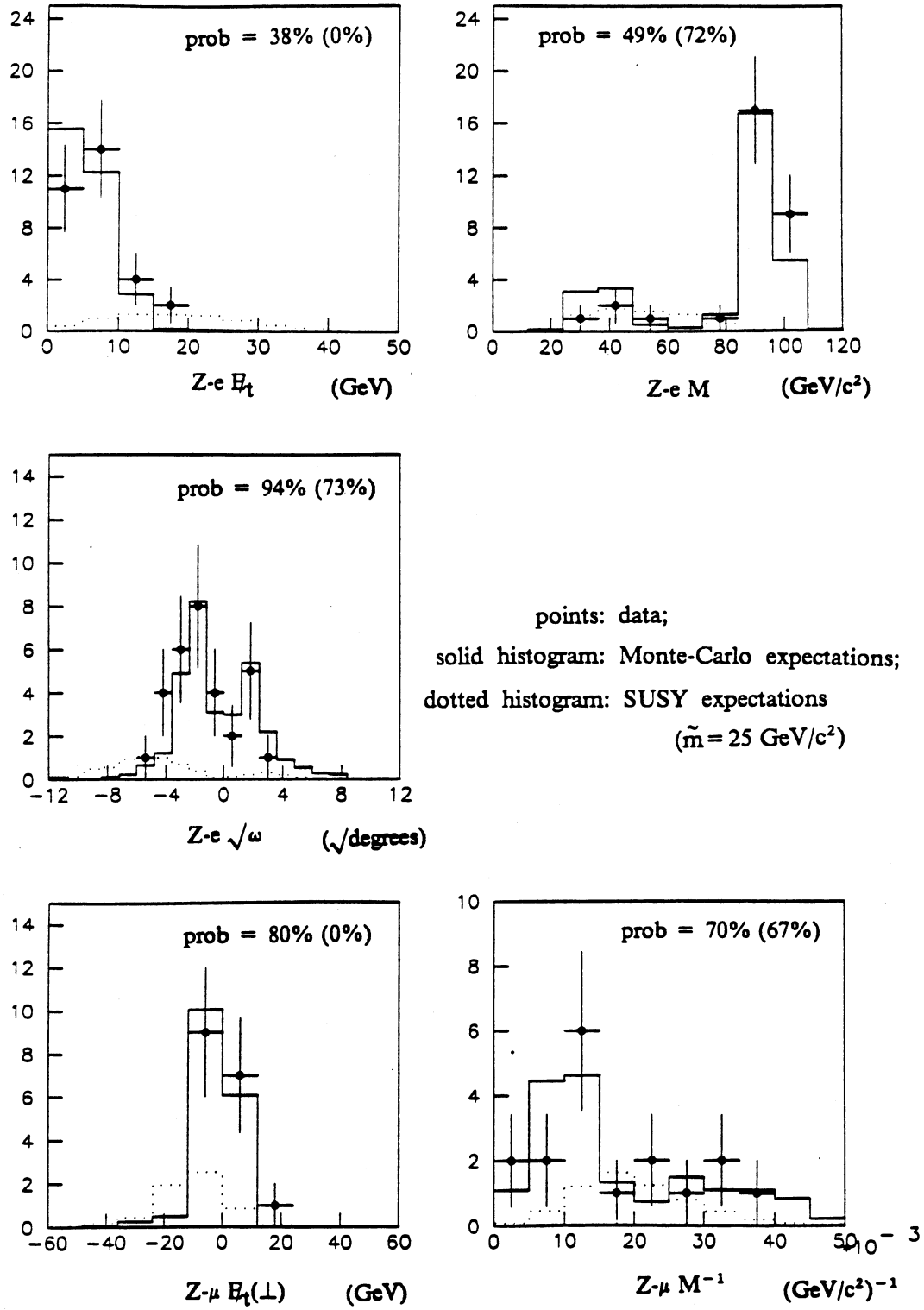

Figure 42: 1-D Distributions for Data, with Monte-Carlo Predictions

The standard method for comparing shapes, predicted and measured, is a χ^2 test. However, a χ^2

may be used meaningfully[39] only if the contents of each bin are large and can be considered to vary in an approximately Gaussian way. While it may be possible to rebin a distribution such that the bin contents are expected to be large, it is in practice non-trivial, and inevitably leads to a loss of shape information.

Instead, we seek a method for testing shapes which in principle can be made bin free. However, since we are dealing with non-parametric distributions, it is inevitable that we have to generate distributions which are binned.

If we have a multi-dimensional distribution which is binned in B bins, then these bins can be arbitrarily labelled with a single index 'i', where i takes values from 1 to B. If our data has n_i events in bin i, where $\Sigma n_i = N$, then we can define a multinomial probability:

$$\mathcal{M} = N! \prod_i e_i^{n_i}/n_i! \qquad (9.12)$$

where e_i (i = 1,B) is the probability that a single event should be in bin i. We evaluate the fraction of times we would expect to see a multinomial probability less than our calculated value $\mathcal{M}$ for sets of simulated events which are described by the distribution $\{e_i;\ i = 1,B\}$. This fraction is the probability that the data can be described by the Monte-Carlo distribution. The double use of the word 'probability' is a little confusing. The 'multinomial probability' (which will inevitably be a very small number) is best thought of as a measure of fit - as is a χ^2 - and as for a χ^2, the 'probability' is the integral of the pdf for the measure of fit beyond the value obtained for the data being tested. This probability should be uniform in the interval [0,1] if the Monte-Carlo predictions correctly describe the underlying distribution of the data. No allowance is made for the fluctuations in the Monte-Carlo pdf's; so care has been taken to ensure that in important regions, the predicted distributions are satisfactorily smooth.

This method can in principle be extended to the continuum limit: as cell size $\to$ 0, $e_i \to$ pdf (at centre of bin i) $\times$ cell size, and $n_i \to$ 0 or 1, so that apart from some normalisation factors (and removing the vanishing cell size), $\mathcal{M} \to \Pi f_j$, where the product is now over the events, j = 1,N and f is the pdf. This is identically the likelihood function. For this analysis, the continuum limit was not used

[39] in the sense that its distribution is described by the probabilities found in chi-squared tables

since it is incompatible with the method for evaluating the expected distribution of $\mathcal{M}$.

Just as with likelihoods, the distribution of $\mathcal{M}$ is not known (to be contrasted with a χ^2, which is the reverse of the continuum limit, and where the distribution is known). Instead, the distribution must be evaluated by Monte-Carlo methods. This can be done quite simply: we envisage B cells containing the probabilities $\{e_i\}$ and we find the cumulative probabilities $\{c_i = \sum_{i'=1}^{i} e_{i'}\}$. Then we choose a random number, r_j, which is uniformly distributed in [0,1]. If $c_{(i-1)} \leq r_j < c_i$, then an 'event' is attributed to cell 'i'. This is done for j equals 1 to N, and in this way, a multinomial distribution is generated. By finding the multinomial probability for many samples of size N, it is possible to establish the distribution of $\mathcal{M}$. If S samples are generated and the estimated probability for the observation of the data is ρ, then the statistical error on this estimate is $\sqrt{[\rho(1-\rho)/S]}$. In practice, 1000 samples were generated.

By using SUSYMC data and using pdf's generated by SUSYMC in a self consistent manner, it was possible to test the operation of this method. For 10 different data sets, each of 100 events, the following probabilities were obtained:

28%, 74%, 80%, 78%, 9%, 34%, 92%, 57%, 58%, 20.4%.

which have a mean of 53.1% and a spread of 30.3% − to be compared with an expected mean of 50% and width 28.9%.

9.5.2 Testing the Data

The W-e Events

The distribution of the events in $(Q\cos\theta, M_t)$ is shown in figure 43. Also shown are the distributions expected for the direct process $W \rightarrow e\nu$ and the tau contributions - the jet fluctuation contribution is not included. In addition, the distribution for the SUSY decays with $\tilde{m}_e = \tilde{m}_\nu = 25$ GeV/c² is given. For illustrative reasons, the Monte-Carlo scatter plots are produced with SUSYMC, although the multinomial test was performed using ISAJET and did include the jet fluctuations.

Naive attempts to obtain the probability that ISAJET can describe the ($Q\cos\theta$,M_t) distribution yield very low values. There are two main reasons. The first is that ISAJET (or, more correctly, the UA1 detector simulation) does not describe the high M_t tail of the data very well. This is due to a somewhat optimistic estimation of the resolution at high M_t in the standard simulation. (For the W-electron mass-fitting, this is handled more carefully, and the simulation describes the data better.) However, in this analysis we are not interested in deviations at high M_t, but rather at the low end. So to test the description of the bulk of the distribution, it is sufficient to look at the data below 108 GeV/c^2 in M_t.

Further, in the data M_t distribution, we see a significant shoulder around 40 to 50 GeV/c^2. In this region, we expect contributions from $W\rightarrow\tau\nu$ and the jet fluctuations. Our estimate, using ISAJET, for the fraction of tau background is 4.0% of the $W\rightarrow e\nu$ rate (excluding the hadronic decays of the tau), which should be compared to the estimate of 6.0% for the cross-section estimate [55]. The latter uses Monte-Carlo data where the polarisation effects of the tau decay have been included, whereas in the former, the decay is determined solely by phase-space. With SUSYMC, we have estimated this fraction as 5.8% as opposed to 4.5% with a flat $\cos\theta^*$ distribution for the tau decay. To allow for the underestimation of the contribution from tau's in the Monte-Carlo generation used, an additional number of tau events have been included (from SUSYMC) to restore the contribution to 6.0%.

With these two modifications, the probability of describing the data is 24%.

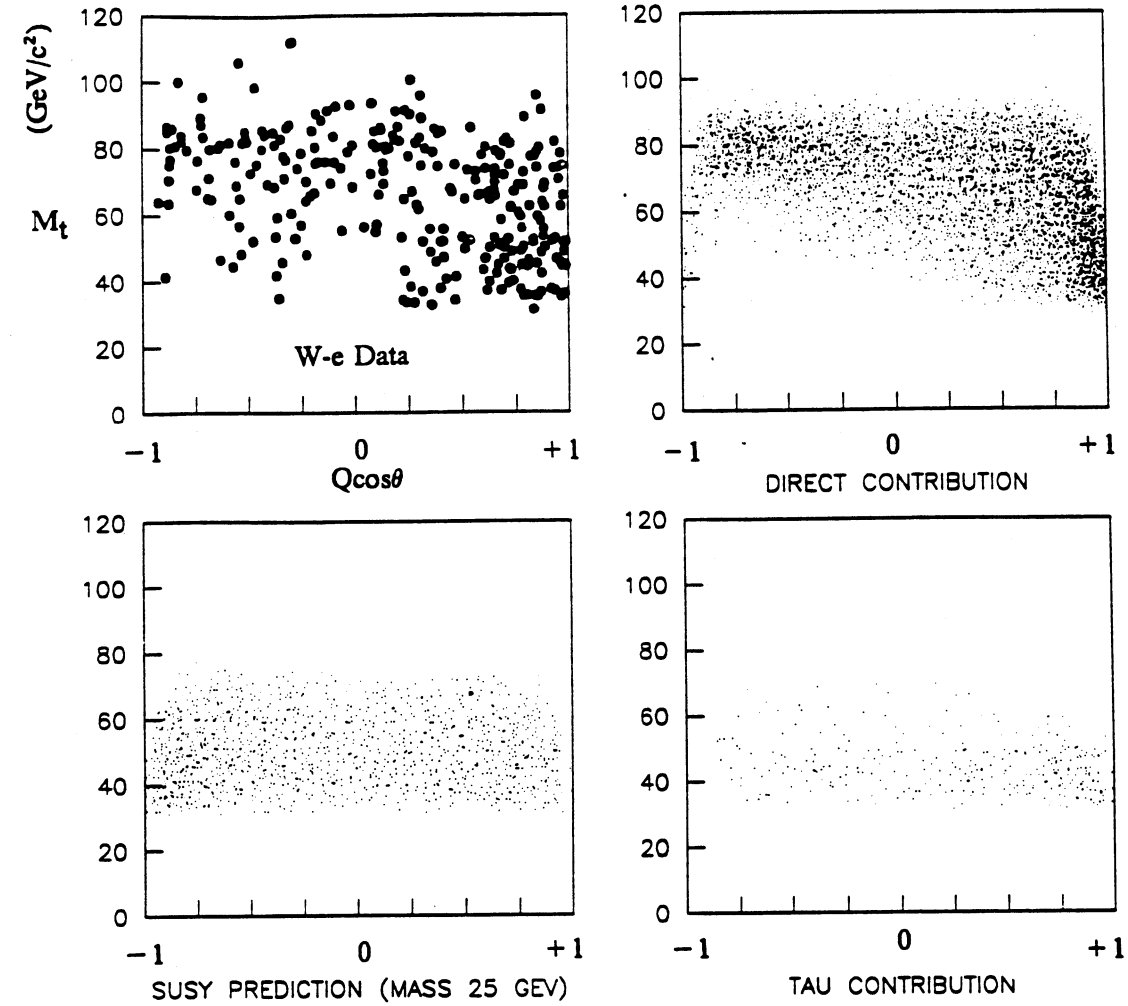

Figure 43: Distributions for W-e Events, with Monte-Carlo Predictions

The Z-e Events

The distribution of the data in the variables E_t and M is shown in figure 44, along with the predictions from SUSYMC (where the same comments as made for the W-e events apply). The data contains 27 Z's and 4 low mass pairs, whereas we expect 23.7 Z's and 7.3 events from Drell-Yan and Z-tau decays (normalised to the total number of events). It is obvious, looking at the 2-D distribution for the di-electrons, that there is an 'interesting' event at lower mass and with significant missing energy - we shall refer to this as Event A. Removing this event, we find that the data is well described by the

background distributions, with a fit probability of 18%. Event A lies in a region where it would appear that the largest background contribution is from $Z \rightarrow \tau\tau$. However, the total tau contribution is expected to be 0.7 ± 0.2 events and the density of ISAJET Monte-Carlo events in the vicinity of A in $(M, \not{E}_t, \sqrt{\omega})$ is low (as it is everywhere).[40] Therefore, the $Z \rightarrow \tau\tau$ contribution to the pdf has been removed in the ISAJET generation and replaced by an estimate using SUSYMC which is smooth due to the considerably larger statistics. With this adjustment, we obtain a fit probability of $4 \pm 1^1/_2\%$, where the uncertainty comes from the uncertainty in the size of the tau contribution.

[40] Of the ISAJET events, 10 tau events pass all the cuts. This leads to the estimate of a contribution of 0.7 to the data. However, SUSYMC suggests that one would expect a contribution of 0.3 events.

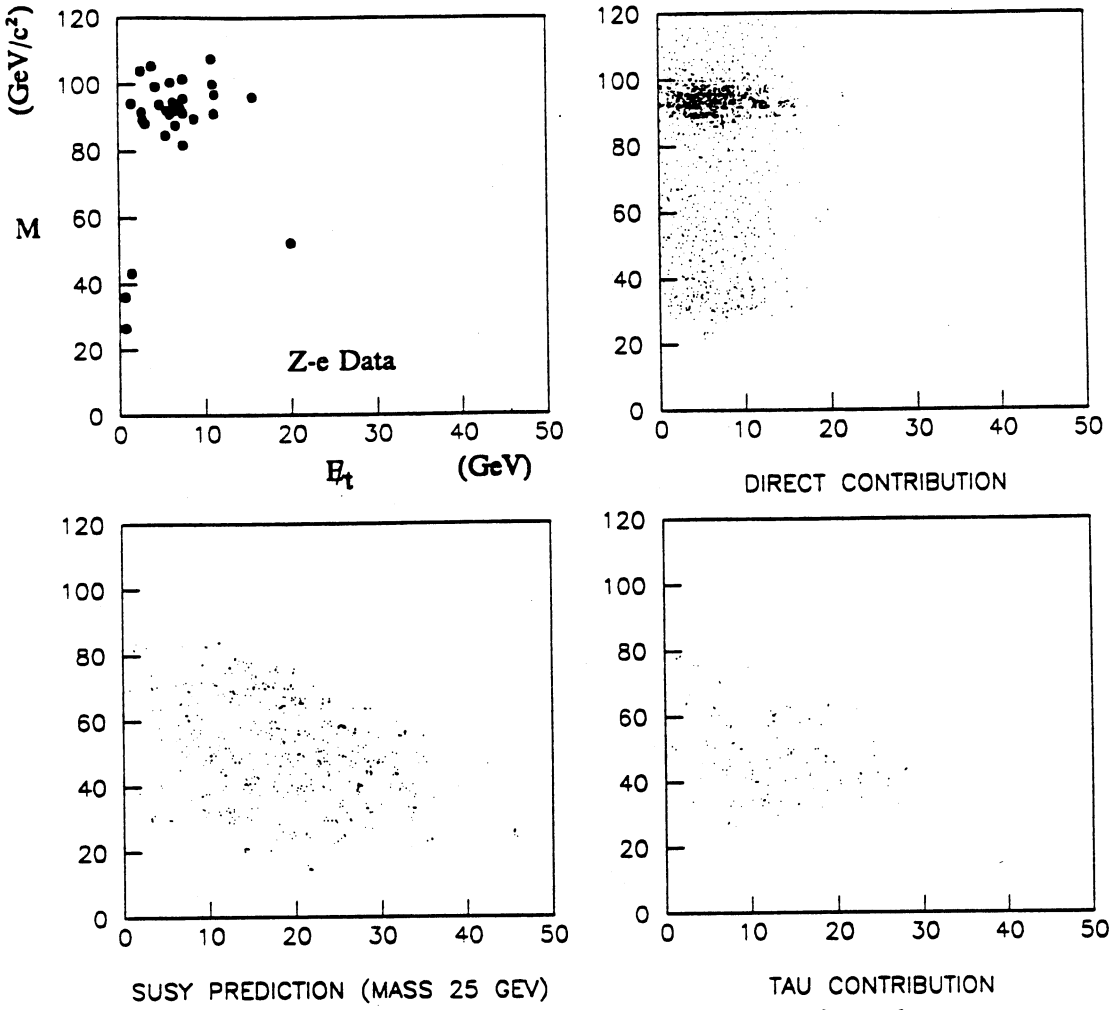

Figure 44: Distributions for Z-e Events, with Monte-Carlo Predictions

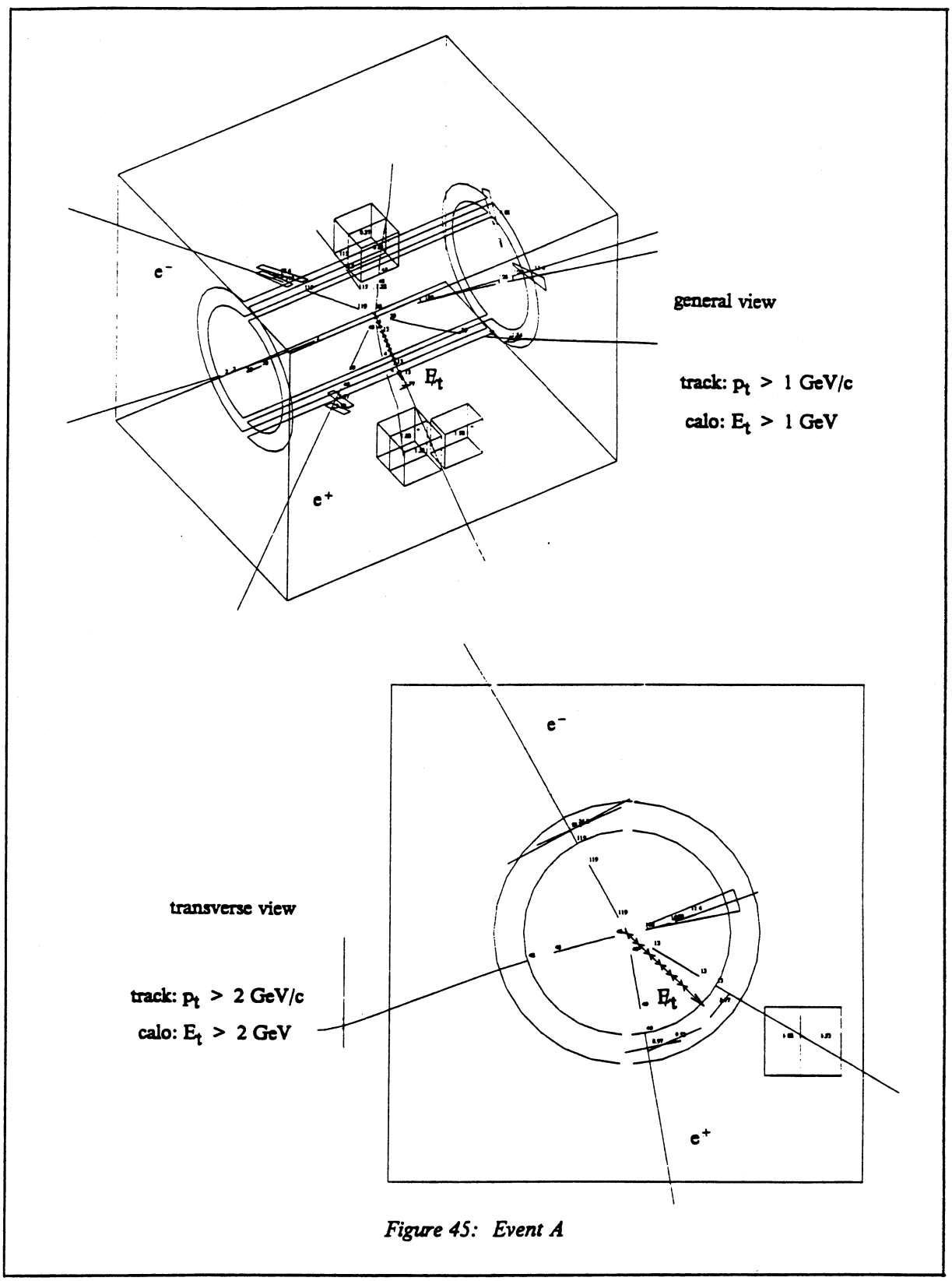

Figure 45: Event A

Event A is shown in figure 45 and its parameters are given in table 25. Several technical comments can

Table 25: Parameters for Event A

e^+	E_t = 15 GeV	p_t = 16 ± 2 GeV/c
e^-	E_t = 52 GeV	p_t = 31 ± 18 GeV/c
	$M = 52 \pm 2$ GeV/c^2 $\not{E}_t$ = 20 GeV ω = 19° $\not{E}_t(\perp)$ = 9 GeV	
jets	E_{t1} = 13 GeV	E_{t2} = 5 GeV

be made about this event:

1. The e^+ is very close to the vertical (ϕ = 10°) and the response of the Gondolas is sometimes dubious close to the vertical, so that for the Z mass fitting, events in which either electron is within ±15° of the vertical are removed. This event might arguably be removed.
2. The CD track momenta are in good agreement with the calorimetry - although they have large errors, and, if anything, can be expected to be underestimates due to possible bremsstrahlung.
3. ω is measured in the CD, which is more accurate than the Gondolas. However, it does rely on the measurement of the z coordinate, which can be prone to systematics. For the e^+, most of the digitisings lie in a reasonable line; however, there are a few which lie above the track, probably due to the effect of a nearby track, but perhaps indicating that ω has been overestimated.
4. The jets lie close to the direction of the missing energy flow in the transverse plane, so that if their energies were underestimated, this might account for some of the missing energy. Further, one of the jets is close to the crack in the calorimetry at x=0, although the displacement of the vertex by +17 cm in x should ensure that no particles escape down the crack.
5. There is one track of p_t = 2.6 GeV/c which apparently deposits 1.2 GeV in the calorimetry, and has some matching Iarocci hits in the side wall, but no muon chamber hits. This particle could be a muon which is ranged out in the side wall iron. If this were the case, it represents a

loss in the recorded calorimetric energy, and would increase $\not\!\!E_t$ by about 1 GeV. There are no other muon candidates in the event.

6. The distribution of energy in the Gondola samplings for the e^+ is a little unusual, since it is spread quite widely. However, the χ^2 which measures the longitudinal development of the electromagnetic shower (comparing it with results from test beam) is 22, which is below the cut of 60. Although the shower shape is not as good as would be expected for a good electron, it is acceptable, and could appear worse by being near the end of the Gondola. Also, it is possible that there could be neutral particles entering the Gondola; however, there are no charged particles entering. The e^- has a chi-squared of 5.
7. The measurement of $\not\!\!E_t$ is highly susceptible to the corrections which allow for the response of the calorimeter to electrons as opposed to hadrons, and the corrections to measured jet energies.

The physics comments which can be made are:

1. If Event A is to be explained by the known physics, the highest probability comes from the tau decays of the Z. However, Event A is at the edge of all interesting distributions for $Z \to \tau\tau$, except the mass plot. For $Z \to \tau\tau$, due to the low mass of the tau, the electrons should more or less follow the line of flight of the tau's and therefore be fairly back to back. The fact that one electron has an E_t of 52 GeV is hard to explain in terms of $Z \to \tau\tau$ with the subsequent decay $\tau \to e\nu\nu$.
2. Although we expect 0.7 ± 0.2 $Z \to \tau\tau$ events, the probability of 1 event out of 31 having $\not\!\!E_t > 20$ GeV and $\sqrt{\omega} < -3.6$ (or $\omega < 13°$) is about $^1/_2$%. However, this probability is not as meaningful as the probability derived from the multinomial test.
3. Other possible explanations of the event are:
    a. $Z \to ee$: this explains the E_t of e^-, but then there is a significant mismeasurement of the e^+ to understand.

b. $p\bar{p} \rightarrow Wg \rightarrow e\nu$ + 'fake e': using ISAJET, we estimate this background to be of the order of 10^{-1} events. One Monte-Carlo event passed the selection, and it did not look at all like Event A.

c. Heavy flavour production: we estimate that the contribution from $b\bar{b}$ and $c\bar{c}$ is of the order of 2×10^{-1}, and none of the Monte-Carlo events selected resembled Event A.

d. Top production: see section 9.8.

e. Jet fluctuations: the technical quality of the e^- would suggest that it is probably a genuine electron, and that it is unlikely that the event is a jet fluctuation. More comments are provided below.

f. SUSY: could be ! It lies comfortably in the centre of all the distributions for $\tilde{m}_e, \tilde{m}_\nu$ = 35 GeV/c^2. However, even with SUSY, it is difficult to explain the 52 GeV E_t of the e^-.

Before concluding, we comment on the possibility that Event A is a result of jet fluctuations. The most important cut to remove the background in the later stages of the event selection is the p_t cut applied to the lowest energy electron candidate - we denote this p_t by p_{t2}. The preferred way of determining jet fluctuation backgrounds is to use the actual data (rather than Monte-Carlo) and to examine the effects of relaxing the cut used to remove the background. The effects of this can be seen in figure 46 [a], where the data is shown as a function of the p_{t2} after all the cuts have been applied (except the 10 GeV/c cut on the fastest track in the CD). It can be seen that there is a steeply falling section of the spectrum below 2 GeV/c which is attributed to jet fluctuations. Above 10 GeV/c are the four low mass di-electron events and the Z's. One is tempted to conclude that the probability that one of the 31 selected events is background is negligible. However, we note that in figure 46 [b], for the like sign events, there are 8 events below the cut at 2 GeV/c; but in addition, there are 3 events above the cut. Two of these 3 events have indications that they could be jet fluctuations, while the third appears to be a photon conversion. By contrast, the 4 opposite sign low mass di-electron candidates are very clean and show no signs of being the result of jet fluctuations.

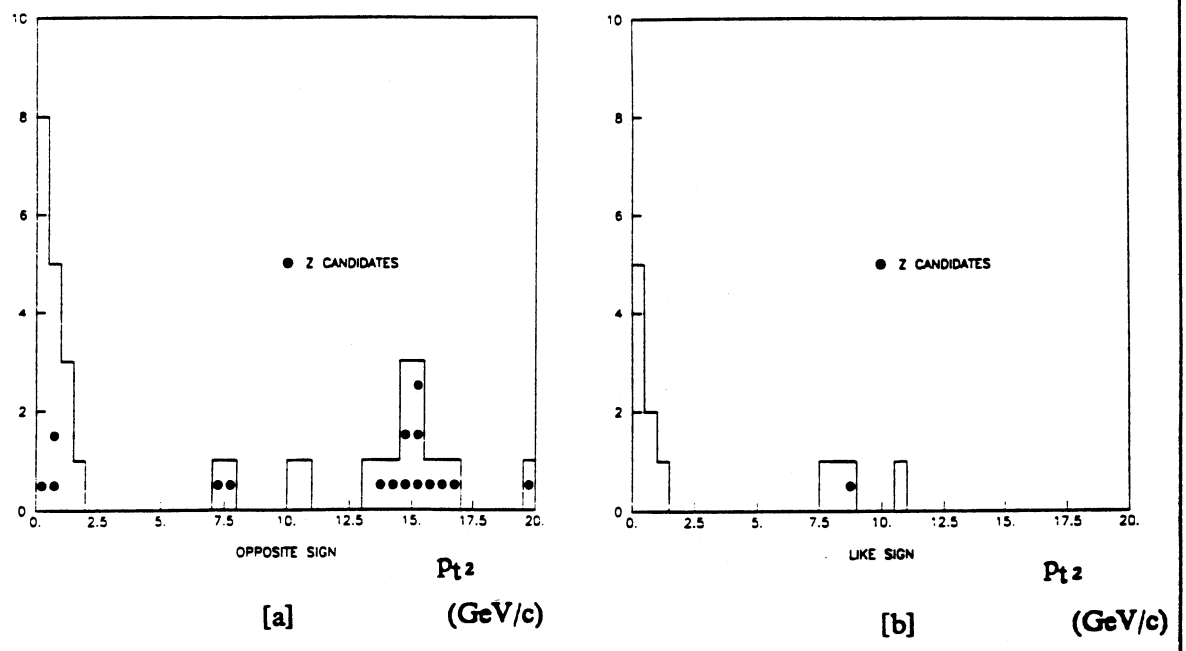

Figure 46: Z-e spectrum as a function of p_{t2}

To conclude, it would appear that Event A is difficult to describe by known processes and could be explained by a supersymmetric decay of a Z. However, there are some doubts as to the reliability of the measurement of the energy of the e^+. Further, the only process which gives a good explanation of the transverse energy of the e^- around $m_Z/2$ is the direct electronic decay of the Z. It seems to the author that the best explanation of Event A is that of $Z \rightarrow ee$, where one of the electrons is very badly measured in the detector, and in a way that is not described by the detector simulation. On the basis of one event, it is impossible to conclude that we have observed 'new physics'. Furthermore, there are no indications from the other three channels of anything exciting.

The Muon Events

The probabilities which are obtained for the muon data are 60% and 35% for the W-μ and Z-μ data respectively. The W-μ events are well described by the Monte-Carlo predictions. It can be seen from the 1-D distributions for the di-muon events that one event has a significant $\not{E}_t(\perp)$. This is the

$Z \rightarrow \mu\mu$ candidate which was removed from the Z mass fitting - see chapter 7. The event is compatible with the decay $Z \rightarrow \tau\tau$, with $\tau \rightarrow \mu\nu\nu$, or a simple Z decay where the momenta of both muons are underestimated. In spite of the large $\not{E}_t(\perp)$, the event is not well explained by SUSY, where one expects that the missing energy arises from photinos recoiling on the opposite side of the muon pair, and hence leading to negative $\not{E}_t(\perp)$.

9.6 S-ISAJET – a More Sophisticated Monte-Carlo

So far, we have seen that the UA1 data is fairly well explained by known processes, and that there is no compelling evidence for 'new physics' beyond the Standard Model. We therefore attempt to find the extent to which we can exclude contributions from SUSY, and set limits on the masses of the supersymmetric particles.

A simple Monte-Carlo (SUSYMC) has already been discussed. However it is important to cross-check its predictions and test the effects of the detector and selection with a more realistic simulation. To this extent, we have attempted to incorporate the SUSY processes in the ISAJET Monte-Carlo. This means that the SUSY events can then be handled in an identical way to the events generated by ISAJET for standard processes. In particular, there are three important tasks to perform:

i. Estimate the observable[41] cross-sections to obtain the normalisation for the distributions generated from SUSYMC.
ii. Verify the shapes of distributions generated by SUSYMC.
iii. Verify the predictions from SUSYMC for the change in observable cross-section with SUSY masses.

For the production of W's, Z's and virtual photons (Drell-Yan) ISAJET [11] uses the explicit matrix element[42] for:

$$\begin{aligned} q\,\bar{q} &\to l + \nu + g \quad \text{via W} \\ q\,\bar{q} &\to l + l + g \quad \text{via Z or } \gamma \end{aligned} \tag{9.13}$$

This is the so called 2→3 matrix element, and its form is very complicated. Since the author is unable to calculate reliably the 2→3 matrix element for final state sleptons, the 2→2 matrix element has been used. This is calculated for the SUSY decays in appendix D.

---

[41] the cross-section which we effectively measure because of the effects of acceptance and selection: $\sigma_{obs} \equiv \langle N_{obs} \rangle / \mathcal{L}$

[42] The phrase 'matrix element' is a misnomer, since what is actually used is the square of the spin averaged matrix element, which is proportional to the differential cross-section, but without the phase-space factor.

ISAJET optionally uses a 2→2 matrix element where the IVB is generated with zero p_t. However, due to the subsequent evolution according to the scheme of Altarelli and Parisi [96] it gains a finite p_t, the distribution of which is not too different from that produced in the 2→3 process. (Use of the 2→3 matrix element is essential only when one requires a reasonable description of the primary jets in W/Z events.)

The appropriate form of the matrix element for the SUSY decays in the Mandelstam representation (see for example [97]) is

$$(ut-\tilde{m}_1{}^2\tilde{m}_2{}^2)/((q^2-m_W{}^2)^2+m_W{}^2\Gamma_W{}^2) \tag{9.14}$$

which replaces the standard 2→2 matrix element, and can be derived from (D.5). $\tilde{m}_1$ and $\tilde{m}_2$ are the masses of the sleptons. Further, the phase space factor is explicitly added - since ISAJET assumes that the decay products of W's and Z's are massless. The modified version of ISAJET will be referred to as S-ISAJET.

In comparing standard W/Z decays from the 2→3 process with SUSY events from the 2→2 process, we might worry about how the absence of an explicit jet in the 2→2 affects: i) the lepton isolation cuts and the jet vetoes, and ii) the shape of the kinematic distributions of the leptons. With regard to i), firstly real W/Z events are generally very quiet and tend to have relatively few high E_t jets; secondly, there are jets in the 2→2 events which are not that dissimilar from those in the 2→3 events. Concerning ii), using standard decays, we find that the differences in shape of the p_t and $\cos\theta$ distributions is totally negligible.

When producing events from ISAJET, we normalise the distributions by the generated luminosity, where luminosity in this context is the number of events generated divided by the integrated cross-section. Thus, our distributions are effectively the differential cross-sections. However, we find that the production cross-section for 2→2 processes is a factor of 1.13(1.16) lower than that for the 2→3 processes for W(Z) production. Since we use the 2→3 generations for the background sources, it is necessary to enhance our 2→2 SUSY generation by this factor.

9.6.1 Using S-ISAJET

To achieve the aims set out at the beginning of this section, events were generated in the following categories:

- $W \rightarrow \tilde{e}\tilde{\nu}$ $\tilde{m}_e = \tilde{m}_\nu = 25$ GeV/c^2
- $W \rightarrow \tilde{\mu}\tilde{\nu}$ $\tilde{m}_\mu = \tilde{m}_\nu = 25$ GeV/c^2
- $Z \rightarrow \tilde{e}\tilde{e}$ $\tilde{m}_e = 25$ GeV/c^2
- $Z \rightarrow \tilde{\mu}\tilde{\mu}$ $\tilde{m}_\mu = 25$ GeV/c^2
- $W \rightarrow \tilde{e}\tilde{\nu}$ $\tilde{m}_e = \tilde{m}_\nu = 15$ GeV/c^2

All of these were with a massless photino.

For each channel, of the order of 2000 events were passed through a fast preselection to apply loose cuts on the generated track momenta. These were intended to be sufficiently loose so as not to reject any events which might pass the subsequent selection. The events passing these cuts were then put through the standard reconstruction and selection. Of the order of 500 events[43] were selected - some events were removed by the cuts, and some were not processed (for which allowance was made).

Using i) the S-ISAJET luminosity, ii) the number of events generated, iii) the fraction of events processed, iv) the factor for comparing the $2 \rightarrow 2$ and $2 \rightarrow 3$ processes, v) the empirical factor required to increase the ISAJET cross-section predictions to agree with the UA1 measurements (see appendix F), the observable SUSY cross-sections are obtained. These cross-sections (σ_{SUSY}) are presented in table 26. Also shown in the table are the observable cross-sections (σ_{back}) for the direct decays including the appropriate tau contributions, but not the Drell-Yan. The ratios of the cross-sections for the supersymmetric decays and standard decays are also included, and are to be compared with the ratios predicted by SUSYMC.

There are a few points to note:

---

[43] the equivalent of one magnetic tape

Table 26: Observable SUSY Cross-sections

	σ_{SUSY} (pb)	σ_{back} (pb)	ratio (%)	ratio from SUSYMC (%)
$W \to \tilde{e}\tilde{\nu}$	47 ± 2	362 ± 6	13.0 ± 0.6	14.0
$W \to \tilde{\mu}\tilde{\nu}$	23 ± 1	190 ± 4	12.1 ± 0.7	13.7
$Z \to \tilde{e}\tilde{e}$	7.7 ± 0.3	44 ± 2	17.7 ± 1.1	14.7
$Z \to \tilde{\mu}\tilde{\mu}$	6.3 ± 0.3	38 ± 2	16.8 ± 1.2	14.6

i. Although the ISAJET predictions are scaled to agree with the measured cross-section in the electron channels, the predictions for the observable muon cross-sections are expected to be overestimated. This arises since the simple detector simulation cannot reproduce all the problems which result in the loss of real events. In particular, it produces near perfect CD-muon chamber matching, and this results in an overestimation of the acceptance. However, these effect cancel out in the ratio of the muon cross-sections.

ii. For the muons, the cross-sections shown in the table are before allowance was made for the muon trigger. The only requirement was that there should be a track in the muon chambers. Throughout, no allowance is made for the electron trigger, which is 96% efficient for single high E_t electrons, as used in this analysis.

iii. For the di-electrons, the cross-sections shown in the table are before the final cuts described in section 9.4.

iv. The error propagation for σ_{SUSY} is a slight underestimate, due to the effect of using a fraction of the events at each of the selection stages.

v. There is probably an uncertainty on the empirical scale factors, and this is not allowed for.

vi. The ratios derived from SUSYMC have errors of the order of ±0.1%.

Looking at the results in table 26, we see that the agreement between SUSYMC and S-ISAJET is reasonable. Obtaining agreement is not essential, but provides a cross-check. S-ISAJET is expected to be more reliable, and is therefore used to fix the SUSY cross-sections relative to those from the standard decays. Applying the muon trigger efficiency and the final selection cuts we obtain the following observable cross-sections:

- $\sigma(W \to \tilde{e}\tilde{\nu}, \tilde{m} = 25)$ = 47 ± 2 pb
- $\sigma(W \to \tilde{\mu}\tilde{\nu}, \tilde{m} = 25)$ = 18 ± 1 pb
- $\sigma(Z \to \tilde{e}\tilde{e}, \tilde{m} = 25)$ = 6.9 ± 0.3 pb
- $\sigma(Z \to \tilde{\mu}\tilde{\mu}, \tilde{m} = 25)$ = 5.8 ± 0.3 pb

The kinematic distributions for S-ISAJET(points) and SUSYMC(histograms) are compared in figures 47 and 48. Chi-squared probabilities are also given, and should be interpreted with care.

Finally, we have checked the evolution with SUSY mass for one channel. The ratio of $\sigma(W \to \tilde{e}\tilde{\nu})$ for $\tilde{m}_e$ = 15 and 25 GeV/c^2 is found to be 1.63 from S-ISAJET and 1.64 from SUSYMC. The ratio of the cross-sections before detector acceptance and selection is equal to the cube of the ratio of the κ factors, and is 1.59.

9.7 Methods for Obtaining Confidence Limits

The confidence limits on the masses of the supersymmetric particles are obtained using likelihood methods, as described in chapter 4. It must be stressed that the limits obtained depend critically on the assumptions for the hierarchy of the masses of the different particles - see chapter 8.

9.7.1 Obtaining the Likelihood

We define a (negative log-) likelihood which is a function of the slepton masses $\tilde{m}_1$ and $\tilde{m}_2$:

$$\mathcal{L}(\tilde{m}_1, \tilde{m}_2) = - \Sigma \log f(x_i, y_i | \tilde{m}_1, \tilde{m}_2) \qquad (9.15)$$

$\{x_i, y_i;\ i = 1,N\}$ are the event parameters of the N data events (for example, M_t and $Q\cos\theta$); f is the corresponding pdf. Note the use of the minus sign. The pdf has two components: i) the sum of contributions from standard (background) processes, ii) the contribution from a potential SUSY signal with particles of masses $\tilde{m}_1$ and $\tilde{m}_2$:

$$f(x,y|\tilde{m}_1, \tilde{m}_2) = \kappa\{ \partial^2\sigma/\partial x \partial y|_{back} + \partial^2\sigma/\partial x \partial y(\tilde{m}_1, \tilde{m}_2)|_{SUSY} \} \qquad (9.16)$$

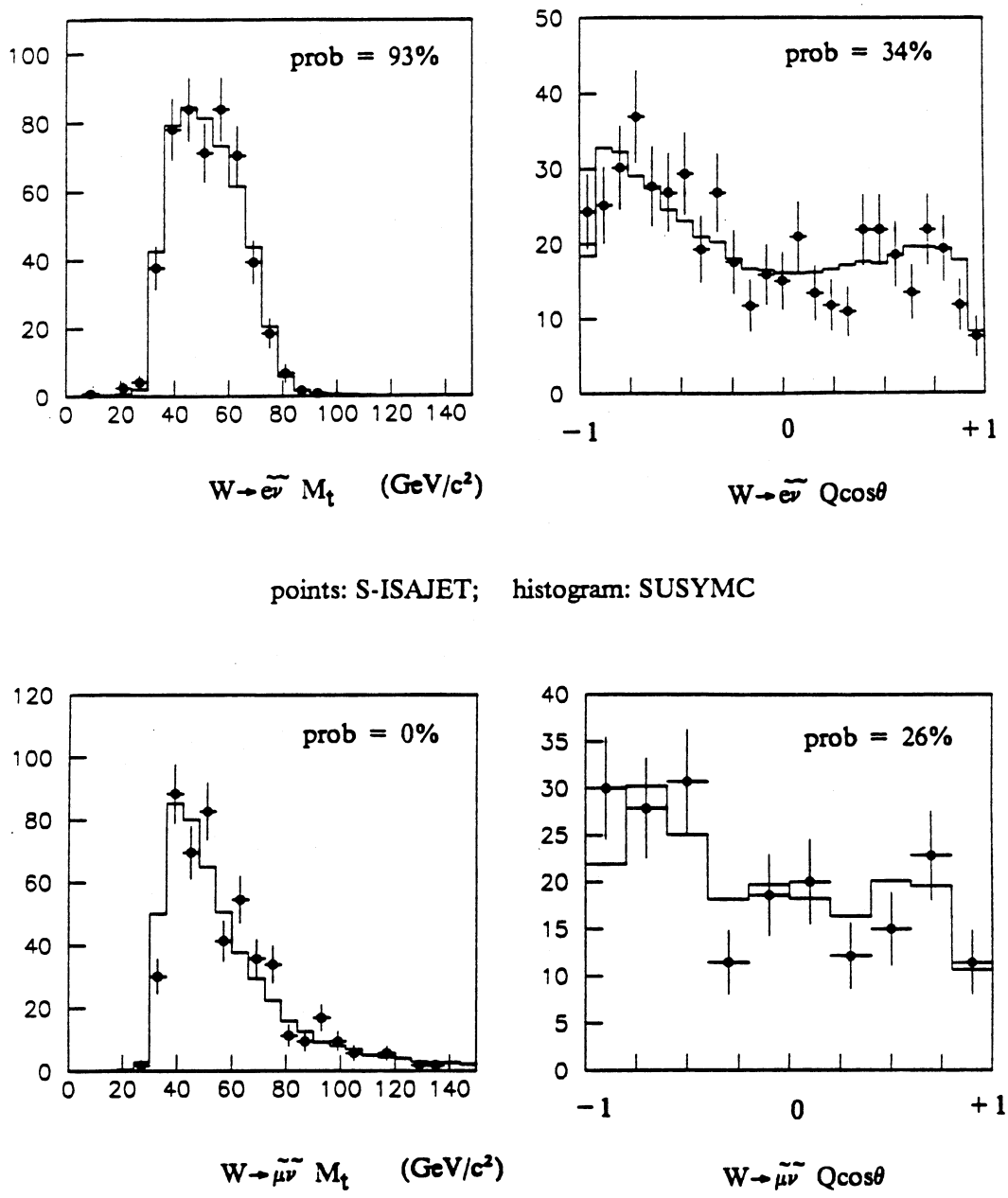

Figure 47: Distributions from S-ISAJET and SUSYMC

where ℵ is the normalisation. The distribution of SUSY events is predicted using SUSYMC, while the normalisation is obtained such that at $\tilde{m} = 25$ GeV/c², the cross-section agrees with the calculation from S-ISAJET in section 9.6. The distribution at and beyond the kinematic limit (where $\tilde{m}_1 + \tilde{m}_2 \geq m_{W,Z}$) is trivially obtained from the background distribution alone.

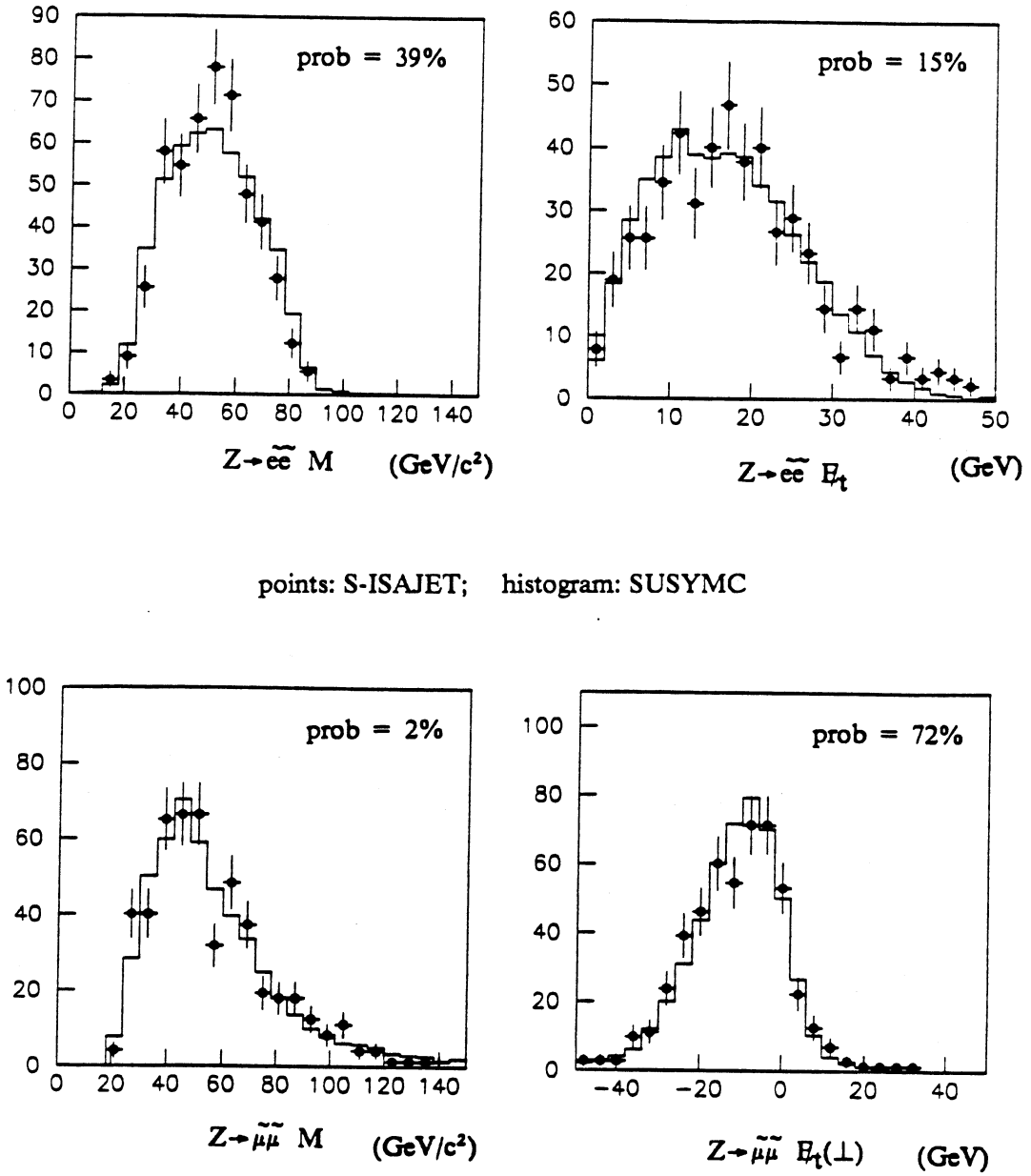

Figure 48: Distributions from S-ISAJET and SUSYMC

In practice, the differential cross-sections are binned as described in section 9.3. Likelihood tests may readily be made on binned data, however, as with any process in which a continuous distribution is sampled in a discrete manner (for example, optical imaging with pixel devices), there is a loss in precision. To improve this, a second order approximation to the shape of the distributions is obtained.

If an event has parameters $(x_0+\delta x, y_0+\delta y)$ where (x_0,y_0) is the centre of the bin containing the event, then the pdf for the event is approximately:

$$f(x_0,y_0) + \partial f/\partial x\cdot\delta x + \partial f/\partial y\cdot\delta y + \partial^2 f/\partial x^2\cdot\delta x^2/2 + \partial^2 f/\partial y^2\cdot\delta y^2/2 + \partial^2 f/\partial x\partial y\cdot\delta x\delta y \qquad (9.17)$$

where the derivatives are estimated by looking at the eight neighbouring bins. Tests indicate that this procedure can produce an improvement of the order of 1 or 2 GeV/c^2 on the limits. There is an additional important effect of this correction. Although the Monte-Carlo predictions for $\partial^2\sigma/\partial x\partial y|_{SUSY}$ are made with very high statistics (tens of thousands events from SUSYMC), when a small change is made in the mass parameters $(\tilde{m}_1,\tilde{m}_2)$, the statistical fluctuations in a given bin can be of the same order as the change in the number of events expected. Since the likelihood method is sensitive to differential changes, care must be taken to minimise statistical effects in the derivatives of the pdf's with respect to masses. The use of expression (9.17) ensures that a better approximation is made to the true pdf and statistical fluctuations are reduced. Further, it is important to be careful with numerical precision, since for a typical $W\rightarrow e\nu$ candidate, the contribution to $\mathcal{L}$ is of the order of -3 and with approximately 300 events, $\mathcal{L}$ is about -1000. We are interested in the differential form of $\mathcal{L}$ and must be able to evaluate this to better than 0.1. Rather than calculating the likelihood explicitly as in equation (9.15), the pdf for a given $(\tilde{m}_1,\tilde{m}_2)$ is divided by the pdf for no SUSY in order to produce an increment to $\mathcal{L}$ which is closer to 0, leading to a value of $\mathcal{L}$ of the order of 0.

9.7.2 Extracting Confidence Limits from the Likelihoods

For $Z\rightarrow\tilde{l}\tilde{l}$ processes, with fixed $\tilde{m}_\gamma$, we consider just one mass parameter: the slepton mass, $\tilde{m}_l$. Estimates of the likelihood ($\mathcal{L}$) are made at a set of values of $\tilde{m}_l$ = 0,5,10,15 ... GeV/c^2. A fourth order polynomial is fitted to the likelihood in the vicinity of the minimum. The location of the minimum, in principle, gives an estimate of the value of $\tilde{m}_l$. However, in the absence of a signal, any minimum is interpreted as a result of statistical fluctuations. A minimum at the kinematic limit is indicative of distributions which show no features expected from a SUSY signal. The likelihood is then exponentiated to form the probability function, which is normalised to unity. The 90% confidence limit is the point below which the area under this function is 10%.

For $W \rightarrow \tilde{l}\tilde{\nu}$ processes, with fixed $\tilde{m}_\gamma$, the confidence limit is necessarily a contour in the plane $(\tilde{m}_l, \tilde{m}_\nu)$. The location of this contour is not a priori well known, although from the previous UA1 analysis one can guess that for $W \rightarrow \tilde{e}\tilde{\nu}$ the contour lies between an arc of radius of about 40 GeV/c^2 and the kinematic limit in the SUSY mass plane. When the approximate location of the confidence limit is found, it is necessary to probe at many points in the mass plane. This requires i) the ability to generate high statistics Monte-Carlo samples at many points in the mass plane - the great advantage of using SUSYMC, and ii) the flexibility to be able to use estimates of the likelihood irregularly scattered in the plane.

The mass plane is divided into cells 2 GeV/c^2 by 2 GeV/c^2. If a value of the likelihood is estimated at some point in the plane close to the centre of a cell, then that value is associated with that cell. Many of the cells do not contain a likelihood estimate, but by looking at the likelihoods of nearby cells, it is possible to make estimates of the likelihoods in these cells. Explicitly, if a cell does not contain an estimate of the likelihood, a search is made within a circle of radius of 10 GeV/c^2. If three likelihood estimates can be found corresponding to distributions generated by SUSYMC, then a planar interpolation is made to estimate the likelihood at the cell's centre. Although the mass combinations at which SUSYMC distributions were generated may be scattered somewhat randomly, with this method the likelihood can be estimated at most points in the mass plane within the kinematic bounds. Again, the likelihood is exponentiated to form the probability function, which is normalised to unity. The region which is excluded with 90% confidence is the area over which the probability function is lowest and accounts for 10% of the integrated probability. This region is identified by including the cells in order of their probability density, lowest first, until the cumulative probability is 10%. The confidence limit contour is the contour of constant probability density which bounds the excluded region.

By using events generated by SUSYMC for $Z \rightarrow \tilde{e}\tilde{e}$ with the appropriate admixture of $Z \rightarrow ee$, and background distributions also generated by SUSYMC, it was possible to test the computer program used to derive the limits. SUSY masses of 15 and 25 GeV/c^2 were used, and in both cases the likelihood showed a sharp minimum at the correct mass.

9.7.3 Handling Systematic Errors.

Three important types of systematics can be identified and have been explicitly allowed for :

i. the uncertainty on the pdf's for the backgrounds due to finite Monte-Carlo statistics;

ii. the normalisation of the SUSY signal;

iii. the effect of a 3% energy scale uncertainty in the electromagnetic calorimeter, and the subsequent effect on the number of (electron) SUSY events which would pass the selection cuts.

The first effect is examined in chapter 4, and leads to the reduction factor, R, defined by equation (4.22).

Uncertainty in the cross-section for the SUSY signal at $\tilde{m} = 25\ GeV/c^2$, obtained with S-ISAJET, leads to a systematic uncertainty in the differential cross-section for every combination $(\tilde{m}_1,\tilde{m}_2)$. If a is the mass of a sparticle (for simplicity, we just consider one) then the discrepancy between the true and the estimated value of a is inversely proportional to the rate of change of the pdf with respect to a: $\delta a \propto (\partial f/\partial a)^{-1}$ (see the discussions in chapter 4). The quantity $\partial f/\partial a$ is essentially the rate at which the differential cross-section changes as the mass parameter, a, is varied. Therefore, the uncertainty in the normalisation of the differential cross-section determines the uncertainty in $\partial f/\partial a$. Hence, the fractional error on the estimate of a will be equal to the fractional error on the normalisation of the SUSY cross-sections deduced from S-ISAJET. If the number of SUSY events selected from the S-ISAJET generation is N_S, then the fractional error on the normalisation is $1/\sqrt{N_S}$. This systematic should be combined in quadrature with the reduction factor for i).

Finally, of all the systematics on the measurements of the event parameters, the most significant is the energy scale uncertainty of $\pm 3\%$ on the energy of electrons. The effect on the $W \rightarrow e\nu$ and $Z \rightarrow ee$ backgrounds is small since the bulk of these electrons have transverse energies well in excess of the 15 GeV cut. However, since the E_t cut potentially removes a significant fraction of electrons from SUSY decays, the uncertainty on the energy scale reflects in the (fractional) uncertainty (ε) on the number of signal events we would expect to pass our selection cuts. This is of the order of 3 or 4%. This effect is also combined in quadrature with the other systematics.

As described in chapter 4, the effect of these systematics can be allowed for by scaling the likelihood. We therefore reduce the likelihood by the factor:

$$R = \{ \sqrt{(1+N_d/N_b)} \oplus 1/\sqrt{N_s} \oplus \varepsilon \}^2 = 1 + N_d/N_b + 1/N_s + \varepsilon^2 \qquad (9.18)$$

9.8 Confidence Limits for SUSY Masses from the Data

9.8.1 The W-e and W-μ Events

Using the W-e events, we find that the likelihood attains its minimum close to the kinematic limit. This is indicative of the absence of a SUSY signal. The confidence limit is shown in figure 49 (solid curve). The $\tilde{m}_e = \tilde{m}_\nu$ limit occurs at 37 GeV/c².

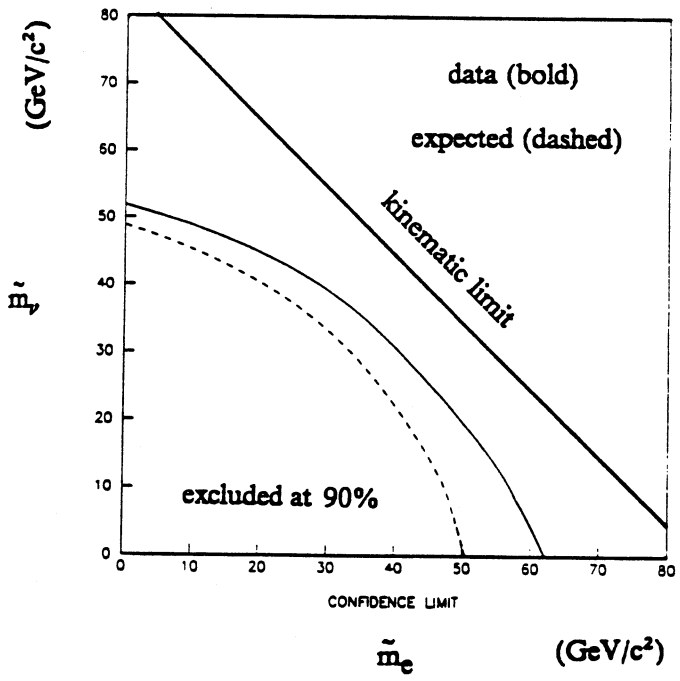

Figure 49: 90% Confidence Limit for $\tilde{m}_e$ and $\tilde{m}_\nu$

Using the muons, we find that the likelihood is minimal near to the kinematic limit; however, it rises far less rapidly than for the electron events. The confidence level is shown in figure 50 (solid curve). The contour is not very stable since the probability function is very flat in the low mass corner of the plot.

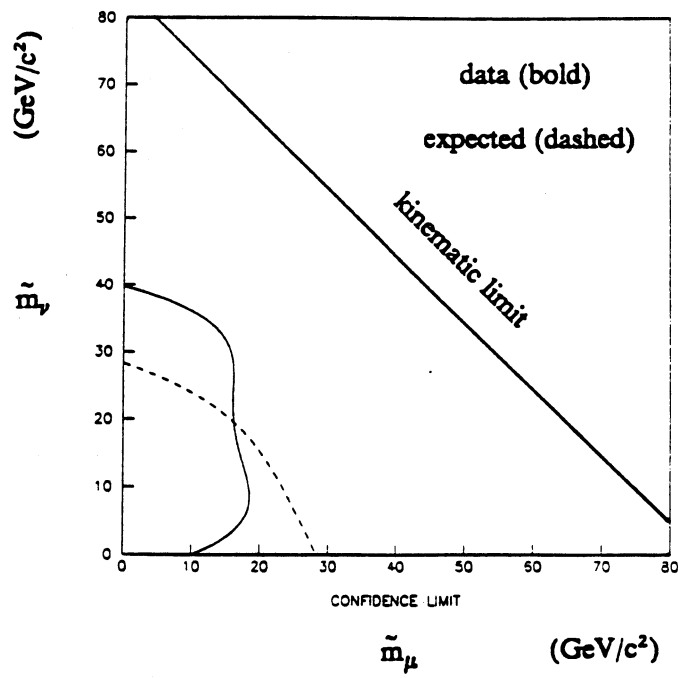

Figure 50: 90% Confidence Limit for $\tilde{m}_\mu$ and $\tilde{m}_\nu$

9.8.2 The Z-e and Z-μ Events

Using the di-electron events, we obtain the likelihood curve shown in figure 51 (solid curve). The curve has a minimum at $\tilde{m}_e$ = 37 GeV/c², with a 90% confidence limit at 14 GeV/c². If the mass of the selectron really were 37 GeV/c², then we would expect 2 events arising from slepton decays of the Z. The minimum is produced by Event A, and this event is responsible for the very low limit. If this event were removed, then the minimum would move up to the kinematic limit, and the limit would become 28 GeV/c² (dotted curve).

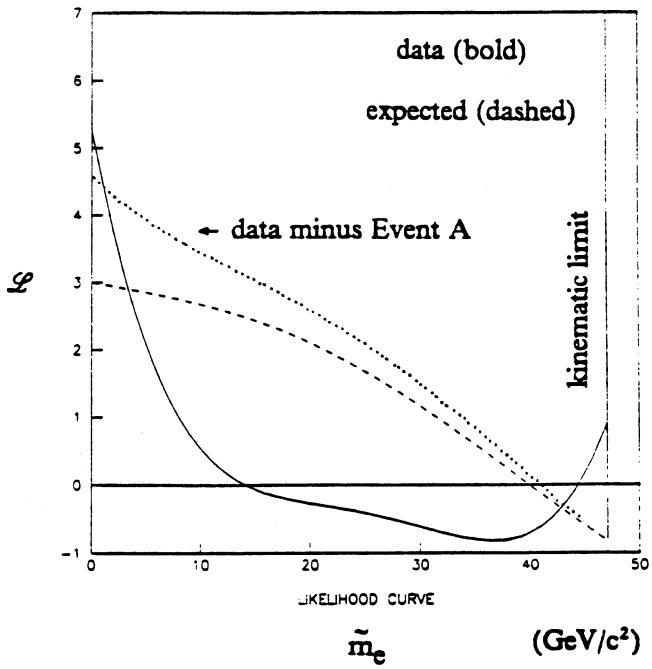

Figure 51: The Likelihood curve for Z-e Events

Using the Z-μ events and the methods outlined in chapter 4, it is, in principle, possible to set a confidence limit on the smuon mass. However, this limit suffers from the second problem alluded to in section 5 of chapter 4. At higher $\tilde{m}_\mu$, the signature for the SUSY process is clear in the variable $\not{E}(\perp)$, but the rate is low. As $\tilde{m}_\mu$ decreases, so the expected rate increases, but the signature diminishes. Therefore, the likelihood rises from the minimum near the kinematic limit, but turns over for $\tilde{m}_\mu$ around 20,25 GeV/c² and starts to fall again. At the turning point of the likelihood, the number of SUSY events which could be expected is about 2.2, which is less than the limit of 2.3 needed to set a 90% limit in the absence of any background, were one to use the number of events as a Poisson variable. The method which we use allows a limit to be set, because implicit in the use of mass as the parameter is the assumption that SUSY decays can contribute. So formally any limit would be correct, but not very realistic. An indication of this appears when the likelihood fails to change by several units between the maximum and minimum (the likelihood curve for the data is shown as the solid curve in figure 52). We do not attempt to set a limit from this channel.

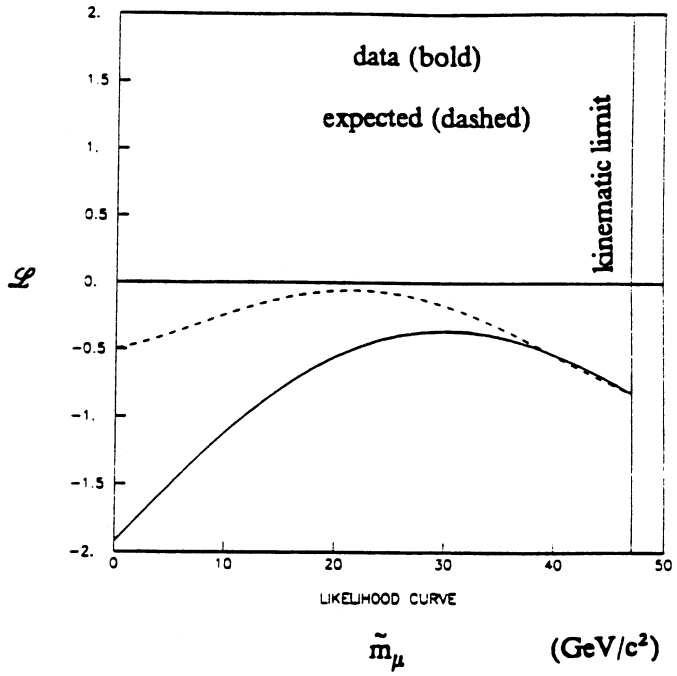

Figure 52: The Likelihood curve for Z-μ Events

9.8.3 The Effect of the Top Quark

The effect of a contribution from the possible decay of top quarks has been investigated in the electron channel. If the top quark exists, then we can expect that some of our data events might be explained by the decay of these quarks. There are two main production mechanisms for top quarks:

- $W \rightarrow t\bar{b}$ (if kinematically allowed)
- gg and $q\bar{q} \rightarrow t\bar{t}$

Since the leptons from top decays tend to be softer than those from W and Z decays (for m_{top} less than or of the order of the IVB masses), they lie in a similar kinematic region to the leptons which would come from slepton decays. Further, it is readily seen that the electron angular asymmetry resulting from $W \rightarrow t\bar{b}$ is in the opposite sense from the V−A asymmetry from $W \rightarrow e\nu$ direct decays, and is in the same sense as the asymmetry for SUSY decays, in the lab frame. Therefore, the decay of

these quarks would represent a further source of background, which, when subtracted from the data, should enhance the SUSY mass limits. In not considering this potential background, we have been conservative.

The current top quark mass limits come from the 'top' analysis of UA1. These limits are complicated by the dependence on the $t\bar{t}$ production cross-section, which is not calculated precisely due to the complexity of higher order processes. This is discussed more fully in reference [98]. Ignoring these complications, the 95% confidence limit is of the order of 40 to 50 GeV/c^2. (There exist indirect limits from the Argus Collaboration [99] from combining their results on $B^0 - \bar{B}^0$ mixing with the constraint of the unitarity of the Kobayashi-Maskawa matrix.)

In considering the effect of a top contribution, the mass of the top quark has been taken as 50 GeV/c^2. Events have been selected from the $m_{top} = 50$ GeV/c^2 ISAJET Monte-Carlo data (see appendix F). The cross-section for $t\bar{t}$ production is estimated by the EUROJET Monte-Carlo [100], which includes some of the α_s^3 matrix elements.

For m_{top} = 50 GeV/c^2, the number of Monte-Carlo events passing the W-e and Z-e selections is shown in table 27. The integrated luminosities are 8.4 and 10.0 pb^{-1} for $t\bar{t}$ and $t\bar{b}$ respectively - to be contrasted with about 0.7 pb^{-1} for the data. The change in the confidence limit from the W-e events is an increase in the limit for $\tilde{m}_e = \tilde{m}_\nu$ of 0.5 GeV/c^2. There are too few Monte-Carlo events to examine the effects on the Z-e limits; however, we have looked at the Monte-Carlo events passing the Z-e selection to determine whether they could explain Event A. Of the seven Monte-Carlo events selected as $t\bar{t}$ background to our Z-e events, one of the events has two isolated electrons; however there is a large neutral jet recoiling against the electron pair. In the remainder of the events, the electrons are highly correlated to jets. For m_{top} = 40 GeV/c^2, none of the six Monte-Carlo events selected resemble Event A.

Table 27: Monte-Carlo 'Top' Events passing Electron Selections

	$t\bar{t}$	$t\bar{b}$
W-e	71	41
Z-e	7	1

9.9 Estimating the Sensitivity

It is important to determine the sensitivity one might expect with the present data. By sensitivity, we mean the limits which would be obtained in the absence of statistical fluctuations and with a perfect description of the various processes. This has been investigated in two ways.

Firstly, using large numbers of Monte-Carlo events, limits were obtained in the same way as the real data. For this study, it was desirable to use SUSYMC to generate the 'data' with large statistics. Consequently, for consistency SUSYMC was also used to generate the differential cross-sections for the background. To obtain the likelihoods corresponding to the number of real events, the likelihood was scaled by the ratio of the number of real events to the number of Monte-Carlo events. Since we cannot simulate jet fluctuation events, this contribution was omitted. This leads to limits which are less conservative since the presence of the jet background reduces our sensitivity to $W \rightarrow \tilde{e}\tilde{\nu}$. However, since it is a factor of three down on the $W \rightarrow \tau\nu$ background, which lies in a similar kinematic region, it is not so significant. This method was used mainly for development studies and tests.

The second method used the background differential cross-sections predicted by ISAJET, including the distribution expected for the jet fluctuations. These distributions were used to predict the expected contents in each bin of the measured parameters. Since only the numbers of events expected are available, and not the event parameters (M_t, $Q\cos\theta$ etc.), the likelihood was obtained as a sum over the bins, and normalised to correspond to the number of data events. This method is expected to be slightly conservative due to the use of binned 'data'. We refer to the limits obtained from this method as the 'asymptotic limits'.

Using the second method, the limits which have been obtained for the W events are shown in figures 49 and 50 (dashed curves), while the likelihood curves for the Z events are shown in figures 51 and 52 (also dashed). The limit expected for the Z-e events is $\tilde{m}_e > 23$ GeV/c^2. We note that the expected limit for the W-e events lies below the limit extracted from the data, which suggests that the data fluctuated downwards in the region where one would expect to see the most SUSY decays. Therefore, it is more sensible to be conservative and to take the expected contour as our final limit in the $\tilde{m}_e$-$\tilde{m}_\nu$ plane.

9.9.1 The Effect of a Massive Photino

All the previous results assumed a very light photino, with a mass close to 0 GeV/c^2. If the photino is massive, the branching ratios for the sleptonic decays of the IVB's are unchanged; however, the spectrum of the leptons from the decay of the sleptons is softened. This means that fewer leptons survive the p_t cuts. For slepton masses well above the photino mass, the change is negligible; however, as $\tilde{m}_l \to \tilde{m}_\gamma$, the energy of the lepton vanishes, and the sensitivity to the processes is lost, since the leptons fail the E_t or p_t cuts. Where the photino is more massive than the slepton, the slepton may be stable and therefore will not decay to a lepton. In this case, the analysis presented here no longer applies. Whatever the photino mass in relation to the sneutrino mass, the sneutrino will inevitably give rise to missing energy, irrespective of whether it decays.

The asymptotic limits for $W \to \tilde{e}\tilde{\nu}$ are given for $\tilde{m}_\gamma = 0$, 10 and 20 GeV/c^2 in figure 53. The likelihood curves for $\tilde{m}_\gamma = 0$, 10 GeV/c^2 are shown in figure 54. In setting limits for $Z \to \tilde{e}\tilde{e}$ with massive photinos, we face a similar problem to that with the Z-μ events. For $\tilde{m}_\gamma$ around 20 GeV/c^2, there are insufficient events to be able to set limits using simple Poisson statistics - at the most, there are 1.4 events expected. For $\tilde{m}_\gamma = 10$ GeV/c^2, the upper limit is unchanged at $\tilde{m}_e > 28$ GeV/c^2; however there is a window for $\tilde{m}_e < 20$ GeV/c^2.

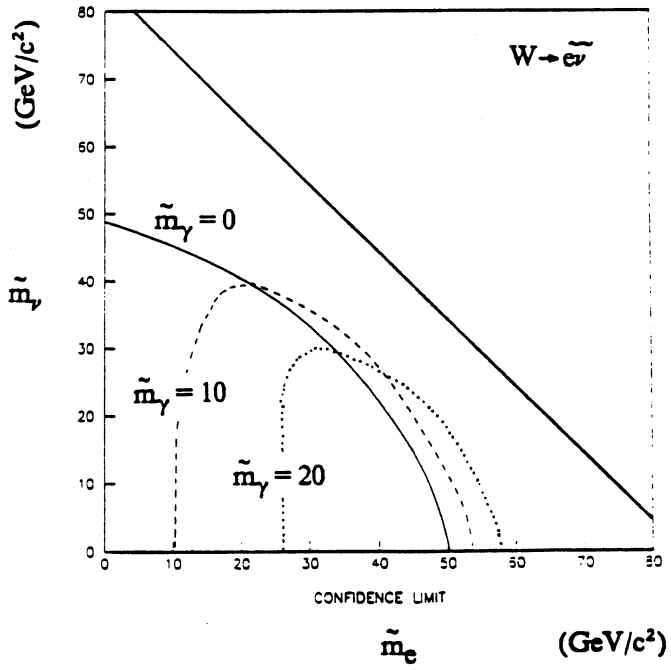

Figure 53: Confidence Limit as a Function of $\tilde{m}_\gamma$

9.9.2 Expectations for ACOL

Finally, it is easy to estimate our sensitivity with integrated luminosities provided by ACOL. We assume identical trigger efficiencies and selection procedures to those used in this analysis[44] and a canonical factor of ten increase in integrated luminosity, and hence in the number of events which would be selected. The confidence limits which are expected for the W events are shown in figure 55. The curves suggest that there is slightly greater sensitivity to the slepton mass compared to the sneutrino mass. This is due to the harder lepton spectrum which results from a heavy slepton (with a light sneutrino), as opposed to the spectrum from a light slepton (with a heavy sneutrino). Consequently, for a heavy slepton, more leptons pass the kinematic cuts. However, this effect is compensated for considerably by the fact that, although there are more events, the extra events have a higher transverse mass, and thus lie under the peak of the direct decay spectrum.

---

[44] It is not obvious that this will actually be the case, since selection criteria may well be tightened to cope with the increased amount of data.

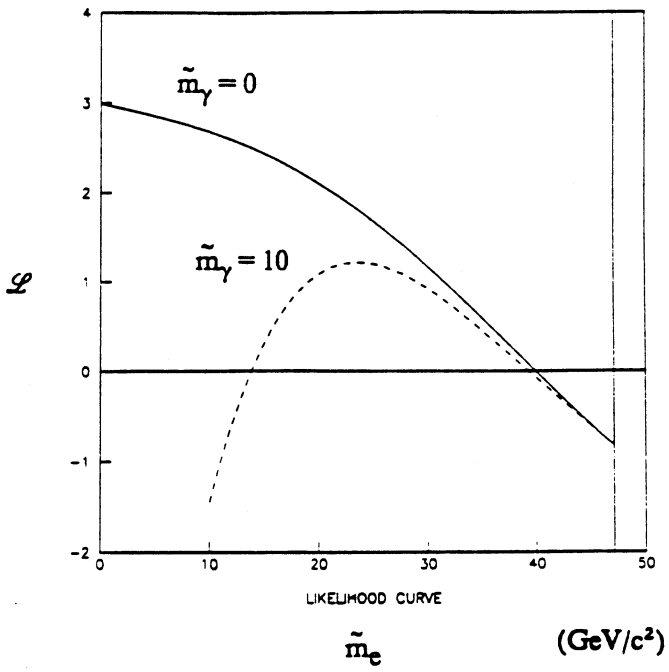

Figure 54: Likelihood Curve as a Function of $\tilde{m}_\gamma$

The likelihood curves for the Z events are shown in figure 56. The limits which can be obtained from this channel are $\tilde{m}_e > 44$ GeV/c² and $\tilde{m}_\mu > 41$ GeV/c².

9.10 Conclusions

With the present UA1 data, there is no evidence for the decay $W \to e\tilde{\nu}$. In the di-electron events, there is one interesting event which can be considered as a candidate for the decay $Z \to \tilde{e}\tilde{e} \to ee\tilde{\gamma}\tilde{\gamma}$. However, this event does have some technical problems, and a more likely explanation is that it is a badly measured $Z \to ee$ decay. We find no evidence for the decays $W \to \tilde{\mu}\tilde{\nu}$ and $Z \to \tilde{\mu}\tilde{\mu}$; however, the sensitivity to these processes is marginal. In the absence of a signal, we set conservative limits on the slepton masses:

$$\tilde{m}_{eL} > 50 \text{ GeV/c}^2 \text{ (with } \tilde{m}_\nu = 0) \text{ at 90\%,}$$

$$\tilde{m}_{\nu L} > 48 \text{ GeV/c}^2 \text{ (with } \tilde{m}_e = 0) \text{ at 90\%,}$$

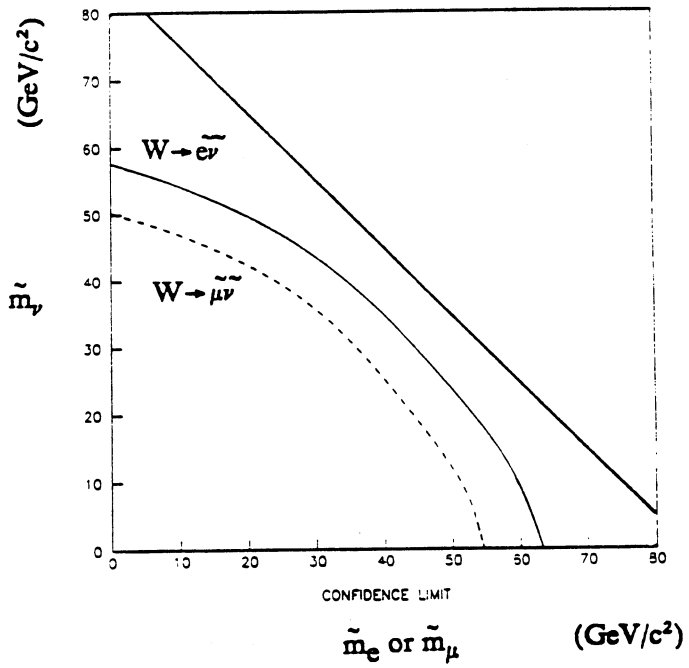

Figure 55: Limits Expected at ACOL Luminosities

$$\tilde{m}_{eL} > 32 \text{ GeV/c}^2 \text{ at } 90\%, \text{ if } \tilde{m}_{eL} = \tilde{m}_{\nu L}$$

The limits from the di-electron channel are severely reduced by the presence of the one unusual event, while the limits from the muon events make no improvement over the results from other experiments.

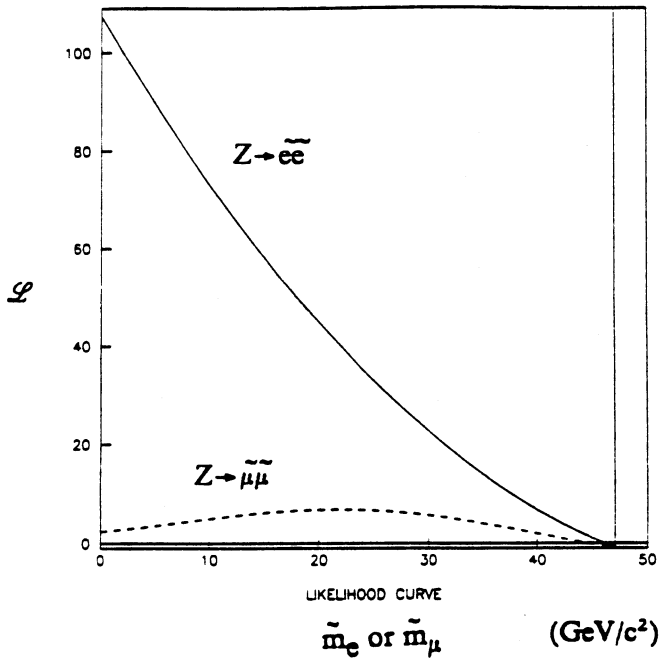

Figure 56: Likelihoods Expected at ACOL Luminosities

APPENDIX A

MULTIPLE SCATTERING

It is readily shown that a fast particle (of charge e) scattered by a charge Ze undergoes a momentum transfer independent of its momentum, in the limit of $v \to c$. For small momentum transfer, the impulse is perpendicular to the line of flight of the particle, and so the angle of deflection (in radians) is proportional to 1/p [101]:

$$\Delta\theta = 2Z\alpha\hbar/pb \tag{A.1}$$

where b is the impact parameter.

For scattering in bulk matter, it can be shown [30] that

$$\Delta\theta_{rms} \approx 0.014(GeV)/p \times \sqrt{L} \tag{A.2}$$

where L is the number of radiation lengths of material traversed.

In figure 57, the passage of a muon through several absorbers is illustrated schematically. What is required for OMF is the correlation after several absorbers between two displacements which arise from multiple scattering [102]. These displacements are to be evaluated at planes k and l, and are denoted by Δx_k and Δx_l, respectively. Resolving the multiple scattering, orthogonal to the original particle direction, into the ξ,ψ directions and evaluating it at the centre of each absorber (i), we obtain:

$$\Delta x_k = \sum_{i=1}^{n(k)} (\partial x_k/\partial\theta^i_\xi \, \Delta\theta^i_\xi + \partial x_k/\partial\theta^i_\psi \, \Delta\theta^i_\psi) \tag{A.3}$$

where n(k) is the number of the last absorber before the kth plane.

Now we consider the product $\Delta x_k \Delta x_l$. The scattering at each absorber (i) is independent, as are the ξ and ψ components. Therefore, the only non-vanishing expectation values are:

$$E[\Delta\theta^i_\xi \, \Delta\theta^i_\xi] = E[\Delta\theta^i_\psi \, \Delta\theta^i_\psi] = {}^1/_2 \, \Delta\theta^i_{rms}{}^2 \tag{A.4}$$

The correlation between Δx_k and Δx_l is thus:

$$E[\Delta x_k \Delta x_l] = {}^1/_2 \sum_{i=1}^{n} (\partial x_k/\partial\theta^i_\xi \, \partial x_l/\partial\theta^i_\xi + \partial x_k/\partial\theta^i_\psi \, \partial x_l/\partial\theta^i_\psi) \, (0.014/p_i)^2 L_i \tag{A.5}$$

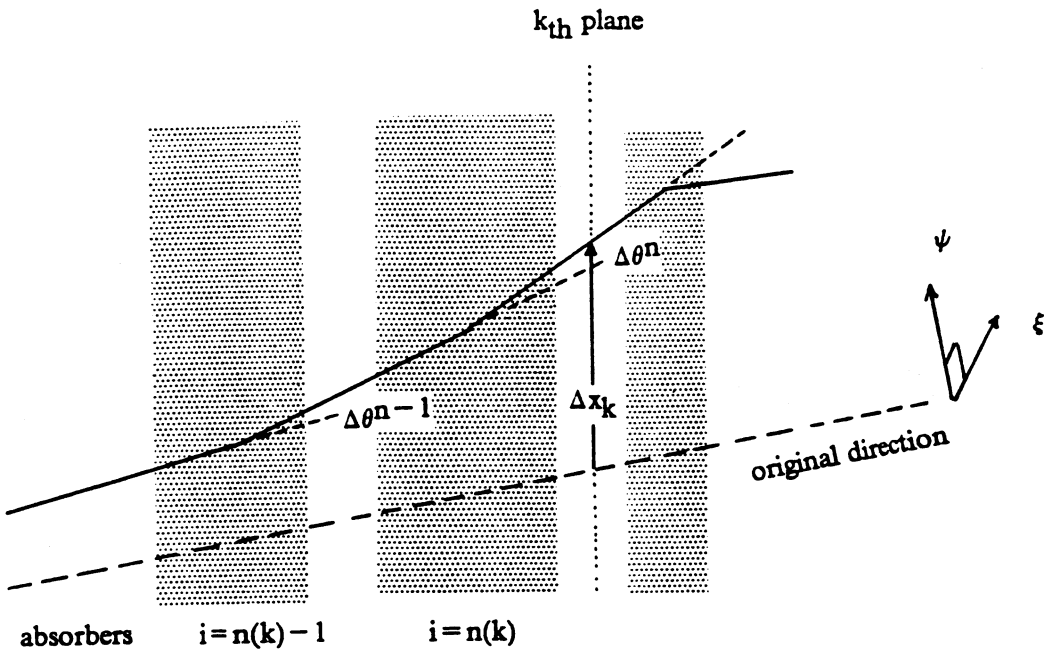

Figure 57: Multiple Scattering in Several Absorbers

where n is the minimum of n(k) and n(l), i.e. the correlation exists only up to the last absorber before the planes k and l, and common to them both.

APPENDIX B

THE UNBIASSED NATURE OF OMF

The method used for the overall momentum fit (OMF) is to find the shift, α (see equation (3.6)), which is to be made to the measured track parameters in the CD, a_0. The best estimate for the muon parameters becomes:

$$\hat{a} = a_0 + \hat{\alpha} \tag{B.1}$$

Effectively, this leads to a reciprocal momentum estimate which is a weighted mean of the CD measurement and the effective muon chamber measurement, as in equation (3.9). However, the multiple scattering error on the muon chamber measurement should be evaluated at the unknown true value of the momentum. In practice, it is necessary to use the best estimate of momentum. Therefore, the procedure is iterated, so that eventually the error σ_μ is expressed as a function of the left hand side of (3.9). Therefore it is not obvious that the estimate of (3.9) is an unbiassed estimate of r.

In this appendix, we show that in a special case, even though the weights may be functions of the estimate, the weighted mean is an unbiassed estimator.

We have measurements $\{r_i\}$ with weights $\{w_i(r_w)\}$ which, in practice, depend on some function of the measurements (the subscript 'i' will be left as implicit). The measurements will be assumed to be uncorrelated, although this proof is easily generalised to allow for correlations. The weighted mean is defined:

$$\hat{r} = \Sigma w(r_w) r \,/\, \Sigma w(r_w) \tag{B.2}$$

where the process of iteration causes r_w to be equal to $\hat{r}$.

If we consider small Gaussian fluctuations of r about a mean r_{true}, i.e. $r = r_{true} + \delta r$, then we can formulate a Taylor expansion for $\hat{r}$:

$$\hat{r} = r_{true} + \Sigma \partial \hat{r}/\partial r \, \delta r + {}^1/_2 \Sigma \partial^2 \hat{r}/\partial r^2 \, \delta r^2 + \ldots \tag{B.3}$$

The expectation of δr is zero, so the expectation of $\hat{r}$ is:

$$E(\hat{r}) \approx r_{true} + {}^{1}/_{2}\Sigma\partial^{2}\hat{r}/\partial r^{2}\, E(\delta r^{2}) + \ldots \qquad (B.4)$$

where the derivatives are evaluated at r_{true}.

After much algebra, we find:

$$\partial^{2}\hat{r}/\partial r^{2} = 2w\,[\partial w/\partial\hat{r}\,(\Sigma w) - w\,(\Sigma\partial w/\partial\hat{r})]\,/\,(\Sigma w)^{3} \neq 0 \qquad (B.5)$$

In general, these derivatives are non-vanishing. However, it is common to choose each weight such as to minimise the chi-squared, and so the weight is given by $w = E(\delta r^{2})^{-1}$ - the reciprocal variance. Thus the third term of (B.3) becomes:

$$[(\Sigma\partial w/\partial\hat{r})(\Sigma w) - (\Sigma w)(\Sigma\partial w/\partial\hat{r})]\,/\,(\Sigma w)^{3} = 0 \qquad (B.6)$$

The third order term will vanish by symmetry, and so $E(\hat{r}) = r_{true}$ to third order.

Therefore, we can conclude that the estimate made by OMF for the momentum is unbiassed to a good approximation.

An important point is that when we obtained the expression for the estimated shift in the parameters, $\hat{\alpha}$, in section 3.3.1, we did not differentiate the covariance matrix X, since strictly the multiple scattering is not a function of the estimated momentum, but of the true momentum. When it comes to the estimation of the Z mass, we are also faced with a chi-squared which is non-linear. However, this is different, since the non-linearities enter in the differences of the parameters, rather than weak non-linearities in the covariance. In addition, for the Z mass, the solutions are not readily obtained, and so the likelihood must be explicitly minimised. Therefore, the resulting estimates cannot be considered unbiassed as they are using OMF, and an attempt must be made to remove the bias. This problem is considered in appendix C.

APPENDIX C

ELIMINATION OF BIASES FROM χ^2 ESTIMATES

Frequently, parameters are estimated by minimising an appropriate χ^2 with respect to these parameters. However, in general these estimates are biassed. In this appendix, we examine the nature of this bias, and show how to remove it.

Suppose we form a χ^2 to describe a measurement m, and we wish to estimate a parameter r:

$$\chi^2 = \chi^2(m,r) \tag{C.1}$$

We minimise (C.1) with respect to r, which leads to r as a function of m:

$$r = r(m) \tag{C.2}$$

In general, r is a non-linear function of m. We assume that m varies with a Gaussian distribution. However, r may not be Gaussian - and this leads to a biassed estimate in the sense that the expectation value of r may not be the true value (which would be obtained in the absence of statistical fluctuations). If $m = m_{true} + \delta m$, then

$$r = r(m) = r(m_{true}) + dr/dm\ \delta m + {}^1/_2 d^2r/dm^2\ \delta m^2 + ... \tag{C.3}$$

$r(m_{true})$ is the true value of r, and so we find, taking the expectation value, that:

$$E(r) \approx r_{true} + {}^1/_2 d^2r/dm^2\ \sigma_m{}^2 \tag{C.4}$$

The second term of (C.4) represents a bias, β, in the estimate of r, and this should be removed. The problem is that, in general, the second derivative cannot be explicitly evaluated since the solution for r cannot be explicitly obtained. r must be found by numerical minimisation, and, in principle, the second derivative can be found by numerical methods - however, this is not very pleasant. Therefore, we seek an improved formulation of the bias.

The solution for r comes from:

$$\partial\chi^2/\partial r|_r = 0 \tag{C.5}$$

$(1-\gamma_5)(1-\gamma_5)$ becomes $2(1-\gamma_5)$, and the γ_5 leads to an antisymmetric tensor which vanishes due to the symmetry of $r^\mu r^\nu$. Therefore

$$|\bar{\mathcal{M}}|^2 \sim \mathrm{Tr}\,[\not{p}_2\gamma_\mu\not{p}_1\gamma_\nu]\, r^\mu r^\nu \tag{D.4}$$

$$= 4\,[2p_1\cdot r\; p_2\cdot r - p_1\cdot p_2 r^2] \tag{D.5}$$

With $p_1 = (p_i,p_i,0,0)$, $p_2 = (p_i,-p_i,0,0)$, and $r = (r_0,r_x,r_y,r_z)$, we find

$$|\bar{\mathcal{M}}|^2 \sim p_i^2 r_t^2 \tag{D.6}$$

where $r_t^2 = r_y^2 + r_z^2$. Since the selectron and sneutrino recoil with equal and opposite p_t in the centre of mass frame, $r_t = 2p_t = 2p_f \sin\theta^*$.

So we conclude that the matrix element behaves like

$$|\bar{\mathcal{M}}|^2 \sim p_i^2 p_f^2 \sin^2\theta^* \tag{D.7}$$

With a little more effort, the factor of $^1/_2$ in equation (8.10) can be extracted.

APPENDIX E

GENERATING MONTE-CARLO DISTRIBUTIONS

There are three common methods for generating events which are distributed according to some distribution, f(x), say.

1. generate events precisely with the distribution f(x);
2. random rejection of some events;
3. keep all events, but give them weights.

Which method one uses depends on what one wants to do, and where greatest statistical precision is required.

E.1 Method 1

Events are generated uniformly in [0,1] in some new variable, y - we denote this distribution by s(y). The transformation $y \rightarrow x$ is determined from:

$$dN = f(x)dx = s(y)dy \tag{E.1}$$

Integrating this with $y \in [0,1]$ gives

$$y = \int^{x} f(x')dx' \equiv F(x) \tag{E.2}$$

Inverting (E.2), we find $x = F^{-1}(y)$. So we can generate a uniform random number in the interval [0,1], and by using F^{-1}, we can derive the value of x, to which this corresponds, and which is distributed according to f(x).

This method works well in simple analytic cases where the function F^{-1} can be found. It is the most efficient way of generating events with the correct distribution. We have used this method in SUSYMC and for the W/Z mass fitting (see last section). If F^{-1} cannot be found, then either method 2 or 3 must be used.

E.2 Method 2

Events are generated uniformly in x and then the pdf at that value, f(x), is compared with some fixed value, L, which is larger than (or equal to) the maximum value of f(x). If the maximum value of f(x) can be found, it is most efficient to use this. The event is kept if $f(x) \geq rL$, where r is a random number distributed uniformly in [0,1].

This is sometimes grossly inefficient where the distribution, f(x), has large variations over the range of generation. In these cases, it may be helpful to generate events according to some distribution g(x) with method 1, where g(x) is a simple approximation to f(x), and G^{-1} can be found. The test then becomes: $f(x)/g(x) \geq rL'$. This method is used heavily by ISAJET.

E.3 Method 3

Events are generated uniformly in x, and then whenever the event is used in a histogram, it is entered with a weight f(x). Again, a hybrid method using method 1 can be adopted. Events can be generated according to g(x), and the weight becomes f(x)/g(x). This method has the advantage that statistical precision can be enhanced in interesting regions of the distribution where the number of events expected is low: instead, one can generate many events, each with low weight. This method is used in SUSYMC to generate Z decays and in handling tau decays.

E.4 Explicit Solutions for Method 1

E.4.1 V−A Distribution

The V−A distribution is described by

$$f(x) = {}^3/_8\,(1+x)^2 \quad \text{where} \quad x \equiv Q\cos\theta^* \tag{E.3}$$

It is readily shown that F^{-1} is given by:

$$F^{-1}(y) = 2\,(\sqrt[3]{y}) - 1 \tag{E.4}$$

E.4.2 SUSY decays

The angular distribution for $W \to \widetilde{e\nu}$ is given by $\sin^2\theta^*$, thus

$$f(x) = {}^3/_4\,(1-x^2) \quad \text{where} \quad x \equiv Q\cos\theta^* \tag{E.5}$$

Finding F^{-1} is non-trivial and requires the solution of a cubic equation, leading to

$$F^{-1}(y) = 2\sin[\,{}^1/_3\sin^{-1}(2y-1)\,] \quad \text{with} \quad \sin^{-1} \text{ in range } [-\pi/2, +\pi/2] \tag{E.6}$$

E.4.3 Breit-Wigner Resonance

Breit-Wigner's are never simple, since inevitably for W/Z production they appear in convolutions with the structure functions. Nevertheless, for a narrow resonance, the Breit-Wigner shape dominates in the region around the pole. A convenient representation of the shape, as a function of the variable s, is

$$f(x) = \mu\Gamma/\pi\,[(x-\mu^2)^2 + \mu^2\Gamma^2]^{-1} \tag{E.7}$$

The required inverse function is

$$F^{-1}(y) = \mu^2 - \mu\Gamma\cot\pi y \tag{E.8}$$

APPENDIX F

ISAJET PRODUCTION

Details of the ISAJET Monte-Carlo of Paige and Protopopescu can be found in reference [11]. To be able to compare Monte-Carlo events with real UA1 data requires a chain of procedures:

1. simulation of $p\bar{p}$ collision - using ISAJET;
2. simulation of the effects of each particle in the UA1 detector;
3. reconstruction of the simulated data - precisely as for the real data.

One such production [103] was performed for the studies made by the UA1 Collaboration in searching for the top quark. Relevant details related to ISAJET are discussed in recent UA1 publications [98], [104]. The amount of Monte-Carlo data generated corresponded to an integrated luminosity of about $10\,pb^{-1}$ - a factor of roughly 16 increase on the real data. This production included the processes

- $W \rightarrow$ anything except top
- $Z \rightarrow$ anything except top
- γ (Drell-Yan) $\rightarrow$ anything except top
- $b\bar{b}$ and $c\bar{c}$ production

Events containing top quarks were generated by the processes

- $W \rightarrow t\bar{b}$
- gg and $q\bar{q} \rightarrow t\bar{t}$

for various top quark masses.

The cross-section used for W production was taken from UA1 measurements [105]. This has the effect of multiplying the ISAJET production cross-sections for W and Z by 1.85 and 1.76 respectively. The high mass Drell-Yan was generated separately, and the ISAJET cross-section was found to be in good agreement with the measured cross-section [106].

Prior to the detector simulation stage, there was a preselection of events requiring that there should be at least one electron or muon in the event with $p_t > 8$ GeV/c. Further, at an intermediate stage in the reconstruction, there was a requirement that there should be a reconstructed electron with $E_t > 12$ GeV and $p_t > 10$ GeV/c, or a reconstructed muon with a track in the muon chambers and $p_t > 10$ GeV/c.

REFERENCES

[1] S.Glashow; 'The Renormalisability of Vector Meson Interactions'; Nucl. Phys. 10 p107 (1959).

[2] A.Salam; proceedings of the 8th Nobel Symposium, Aspenasgarden (1968).

[3] S.Weinberg; 'A Model of Leptons'; Phys. Rev. Lett. 19 p1264 (1967).

[4] C.Rubbia, P.McIntyre, D.Cline; 'Producing Massive Neutral Intermediate Vector Bosons with Existing Accelerators'; proceedings of the 'International Neutrino Conference', Aachen (1976).

[5] UA1 Collaboration; 'A 4π Solid Angle Detector for the SPS used as a Proton-Antiproton Collider at a Centre of Mass Energy of 540 GeV'; CERN/SPSC/78-06 (1978).

[6] UA1 Collaboration; 'Experimental Observation of Isolated Large Transverse Energy Electrons with Associated Missing Energy at $\sqrt{s} = 540$ GeV'; Phys. Lett. 122B p103 (1983).

[7] UA1 Collaboration; 'Experimental Observation of Lepton Pairs of Invariant Mass Around 95 GeV/c^2 at the CERN SPS Collider'; Phys. Lett. 126B p398 (1983).

[8] UA1 Collaboration; 'Observation of the Muonic Decay of the Charged Intermediate Vector Bosons'; Phys. Lett. 134B p469 (1984).

[9] UA1 Collaboration; 'Search for B^0-$\bar{B}^0$ Oscillations at the CERN Proton-Antiproton Collider'; Phys. Lett. 186B p247 (1987).

[10] UA1 Collaboration; 'Observation of Jets in High Transverse Energy Events at the CERN Proton-Antiproton Collider'; Phys. Lett. 123B p115 (1983).

[11] F.Paige, S.Protopopescu; 'ISAJET 5.20: a Monte-Carlo Event Generator for pp and $\bar{p}p$ Interactions'; invited talk at the 'Workshop on Observable Standard Model Physics at the SSC', BNL-38034 (1986).

[12] 'Achievements with Antimatter'; Publications Section CERN/DOC (1983).

[13] E.Radermacher; 'The Experimental Discovery of the W^+, W^- and Z^0 at the CERN $p\bar{p}$ Collider'; Prog. in Particle and Nuclear Phys. 14 (1985).

Thus, taking the absolute derivative with respect to m, we find:

$$d/dm(\ \partial\chi^2/\partial r\ ) = \partial/\partial m\ \partial\chi^2/\partial r + dr/dm\ \partial/\partial r\ \partial\chi^2/\partial r = 0 \qquad (C.6)$$

Including a factor of $^1/_2$ in the χ^2 definition, the second double derivative in (C.6) is simply the inverse variance of r, v^{-1}. So this leads to:

$$dr/dm = -v\ \partial/\partial m\ \partial\chi^2/\partial r \qquad (C.7)$$

Now, the χ^2 is inevitably constructed with the form:

$$\chi^2 = {}^1/_2\ (m-\phi(r))^2/\sigma_m{}^2 \qquad (C.8)$$

Thus, (C.7) becomes:

$$dr/dm = v/\sigma_m{}^2\ d\phi/dr \qquad (C.9)$$

$$\Rightarrow \qquad \beta = {}^1/_2\ d/dm\ (v\ d\phi/dr) \qquad (C.10)$$

The benefit of this result is that v and $d\phi/dr$ can be explicitly evaluated as functions of r, and to determine the bias requires only the numerical evaluation of a first derivative.

This result is readily generalised to a situation where there are several measurements $\{m_a\}$ and it is required to estimate the quantities $\{r_i\}$. Then the bias for r_i is

$$\beta_i = {}^1/_2\ d/dm_a\ (v_{ij}\ d\phi_a/dr_j) \qquad (C.11)$$

APPENDIX D

CALCULATION OF MATRIX ELEMENT FOR $F\bar{F} \to W \to \tilde{E}\tilde{\nu}$

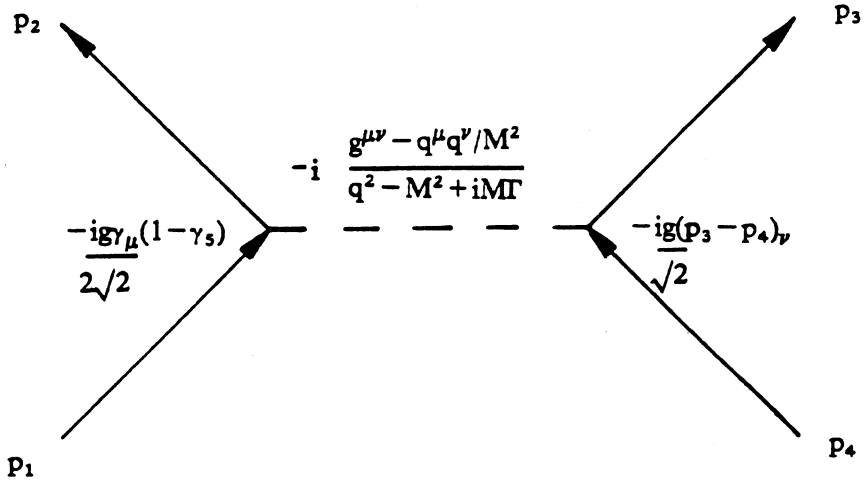

Figure 58: $f\bar{f} \to W \to \tilde{e}\tilde{\nu}$

Using the Feynman rules [72] as illustrated in figure 58 and the definitions of figure 38, we obtain the matrix element

$$\mathcal{M} = \frac{-ig\bar{v}(p_2)\gamma_\mu(1-\gamma_5)u(p_1)}{2\sqrt{2}} \; -i\frac{g^{\mu\nu}-q^\mu q^\nu/m^2}{q^2-m^2+im\Gamma} \; \frac{-ig(p_3-p_4)_\nu}{\sqrt{2}} \tag{D.1}$$

$\gamma_\mu q^\mu$ becomes $\not{q}$, which vanishes when acting on the quark spinors (in the limit that the quarks are massless), so that the $q^\mu q^\nu$ term vanishes. Dropping all the constants and the denominator of the W propagator gives

$$\mathcal{M} \sim \bar{v}(p_2)\gamma_\mu(1-\gamma^5)u(p_1)\, r^\mu \tag{D.2}$$

where $r \equiv p_3 - p_4$. So the square of the spin averaged matrix element is

$$|\bar{\mathcal{M}}|^2 \sim \mathrm{Tr}\,[\not{p}_2\gamma_\mu(1-\gamma_5)\not{p}_1\gamma_\nu(1-\gamma_5)]\, r^\mu r^\nu \tag{D.3}$$

[14] M.Barranco Luque et al; 'The Construction of the Central Detector for an Experiment at the CERN $\bar{p}p$ Collider'; NIM 176 p175 (1980).

[15] F.Sauli; 'Principles of Operation of Multiwire Proportional and Drift Chambers'; CERN 77-09 (1977).

[16] S.Cittolin; 'UA1 VME Readout System', proceedings of the 'VMEbus in Physics' Conference, CERN 86-01.

[17] C.Cochet at al; 'The Central Electromagnetic Calorimeter of UA1'; NIM 243A p45 (1986).

[18] M.Albrow; 'Issues of Calorimetry'; Nucl. Phys. 461A p417 (1987).

[19] M.Corden et al; 'Central Hadron Calorimeter of UA1'; NIM 238A p273 (1985).

[20] G.Bauer et al; 'Upgraded Muon Detection System for UA1 based on Limited Streamer Tubes'; NIM 253A p179 (1987).

[21] UA1 Collaboration; 'A Proposed Upgrade of the Large Angle Muon Detection in UA1'; CERN SPSC/82-51 (1982).

[22] K.Eggert at al; 'Large Area Drift Chambers for a Muon Detector at the $p\bar{p}$ Collider'; NIM 176 p217 (1980).

[23] A.Astbury et al; 'The UA1 Calorimeter Trigger'; NIM 238A p288 (1985).

[24] UA1 Collaboration; 'W Production Properties at the CERN SPS Collider'; Nuovo Cimento 41 p1 (1986).

[25] G.Hilgers et al; 'Short Description of the Muon Fast Trigger Electronics for the UA1 Experiment'; UA1 TN/81-22 (1981).

[26] J.Dorenbosch et al; 'Selection of Muon Events in the 168E Processors'; UA1 TN/85-31 (1985).

[27] M.Pimia; 'Track Finding in the Image Chamber by Chaining Method'; UA1 TN/81-12 (1981).

[28] A.Norton; 'Track and Event Reconstruction in the UA1 Detector'; 1983-1984 Academic Training Programme (CERN) unpublished.

[29] V.Karimaki; 'Fast Trajectory Fitting in Uniform Field'; UA1 TN/82-24 (1982).

[30] Particle Data Group; 'Particle Properties Data Booklet'; Phys. Lett. 170B (1986).

[31] S.Haywood, J.Kroll; 'The Autofixup Program'; UA1 TN/87-47 (1987).

[32] D.Drijard, A.Norton, L.Pape; 'Hybrid Fit of Track Parameters'; BEBC technical note, unpublished (1979).

[33] S.Haywood; 'Mid-Term Assessment'; report submitted to the University of Birmingham (1986).

[34] F.James; 'The Statistics of Very Small Samples - Bayesian and Classical Approaches'; 1986-1987 Academic Training Programme (CERN) unpublished.

[35] W.Eadie et al; 'Statistical Methods in Experimental Physics'; North Holland.

[36] A.Chillingarian; 'Statistical Decisions under Non-Parametric a Priori Information'; Yerevan Physics Institution 818(45)-85 (1985).

[37] T.Lavine; 'Search for Single Photons from Radiative Production of Supersymmetric Particles or Neutrinos'; thesis University of Wisconsin (1986).

[38] W.Pauli; proceedings of the '7^{th} Solvay Congress', Brussels (1933).

[39] E.Fermi; 'Versuch einer Theorie der β Strahlen'; Z. Phys. 88 p161 (1934).

[40] T.Lee, C.Yang; 'Question of Parity Conservation in Weak Interactions'; Phys. Rev. 104 p254 (1956).

[41] C.Wu et al; 'Experimental Test of Parity Conservation in Beta Decay'; Phys. Rev. 105 p1413 (1957).

[42] G.'t Hooft; 'Renormalisable Lagrangians for Massive Yang-Mills Fields'; Nucl. Phys. 35B p519 (1971).

[43] C.Itzykson, J.Zuber; 'Quantum Field Theory'; McGraw Hill.

[44] F.Halzen, A.Martin; 'Quarks and Leptons'; Wiley.

[45] J.Goldstone; 'Field Theories with Superconductor Solutions'; Nuovo Cimento 19 p154 (1961).

[46] P.Higgs; 'Spontaneous Symmetry Breakdown without Massless Bosons'; Phys. Rev. 145 p1156 (1966).

[47] F.Hasert et al; 'Search for Elastic Muon-Neutrino Electron Scattering'; Phys. Lett. 46B p138 (1973).

[48] P.Collins, A.Martin; 'Hadron Interactions'; Adam Hilger.

[49] S.Ellis, R.Kleiss, W.Stirling; 'W's, Z's and Jets'; Phys. Lett. 154B p435 (1985).

[50] E.Tscheslog; 'Studies of the Muonic Decays of the Charged Intermediate Vector Boson in the UA1 Experiment'; thesis RWTH Aachen (1987).

[51] S.Haywood, E.Tscheslog, S.Wimpenny; 'W→$\mu\nu$ Selection and Cross-Sections'; UA1 TN/87-21 (1987).

[52] R.Edgecock; 'J/ψ Production in Proton-Antiproton Collisions at $\sqrt{s}$ = 630 GeV'; thesis Birmingham University.

[53] S.Haywood; 'Some Comments on the Simulation of High Momentum Tracks in the CD, and the Calibration of the W and Z (Muon) Masses'; UA1 TN/86-122 (1986).

[54] S.Haywood, E.Tscheslog, S.Wimpenny; 'The 1984-85 W (Muon) Mass'; UA1 TN/86-120 (1986).

[55] UA1 Collaboration; paper in preparation. See for example: E.Locci; 'W and Z Physics and the Standard Model'; CERN-EP/87-154 (1987).

[56] UA2 Collaboration; 'Measurement of the Standard Model Parameters from a Study of W and Z Bosons'; Phys. Lett. 186B p440 (1987).

[57] R.Leuchs; 'Produktion und Myonischer Zerfall des Intermediaeren Vektorbosons Z^0'; thesis University of Kiel.

[58] R.Leuchs, E.Tscheslog, S.Wimpenny; 'The Z→$\mu^+\mu^-$ Cross-Section from the 1983, 1984 and 1985 Runs'; UA1 TN/87-22 (1987).

[59] S.Haywood, R.Leuchs, E.Tscheslog, S.Wimpenny; 'The 1983-84-85 Z (muon) Mass'; UA1 TN/86-119.

[60] G.Altarelli; 'Phenomenology of the Electroweak Gauge Bosons'; CERN-TH 3983/84 (1984).

[61] G.Altarelli et al; 'Precision Tests of the Electroweak Theory at the Z^0'; 'Physics at LEP', CERN 86-02.

[62] G.Altarelli; 'Status of the Electroweak Theory'; proceedings of the '23rd International Conference on High Energy Physics' (Berkeley) p119 (1986).

[63] W.Marciano, A.Sirlin; 'Testing the Standard Model by Precise Determination of W and Z Masses'; Phys. Rev. 29D p29 (1984).

[64] M.Consoli, A.Sirlin; 'The Role of the One-Loop Electroweak Effects in $e^+e^- \rightarrow \mu^+\mu^-$'; 'Physics at LEP', CERN 86-02.

[65] S.Haywood, S.Wimpenny; 'The Determination of Standard Model Parameters using W/Z (Muon) Data'; UA1 TN/86-121 (1986).

[66] U.Amaldi et al; 'A Comprehensive Analysis of Data Pertaining to the Weak Neutral Current and the Intermediate Vector Boson Masses'; Phys. Rev. 36D p1385 (1987).

[67] V.Gates, E.Kangaroo, M.Roachcock, W.Gall; 'Stuperspace'; Physica 15D p289 (1985).

[68] J.Iliopoulos; 'Unification and Supersymmetry'; proceedings of the '1984 CERN School of Physics', CERN 85-11.

[69] C.Llewellyn-Smith; proceedings of the 'Supersymmetry versus Experiment Workshop', CERN-TH 3311/82 (1982).

[70] S.Hawking, D.Page, C.Pope; 'Quantum Gravitational Bubbles'; Nucl. Phys. B170 (FS1) p283 (1980).

[71] J.Ellis; Lectures presented at the SLAC Institute on Particle Physics, CERN-TH 3747/83 (1983).

[72] H. Haber, G. Kane; 'The Search for Supersymmetry: Probing Physics beyond the Standard Model'; Phys. Rep. 117 p77 (1985).

[73] S.Coleman, J.Mandula; 'All Possible Symmetries of the S Matrix'; Phys. Rev. 159 p1251 (1967).

[74] D. Nanopoulos; 'Applied Supersymmetry and Supergravity'; Rep. Prog. Phys. 49 p61 (1986).

[75] H.Baer, J.Ellis, D.Nanopoulos, X.Tata; 'Supersymmetry at Bay?'; Phys. Lett. 153B p265 (1985).

[76] C.Kounnas et al; 'Super-Gravity Induced Radiative SU(2)×SU(1) Breaking with Light Top Quark and Stable Minimum'; Phys. Lett. 132B p95 (1983).

[77] P.Fayet; 'Scattering Cross-Sections of the Photino and the Goldstino on Matter'; Phys. Lett. 86B p272 (1979).

[78] D.Froidevaux; private communication.

[79] B.Naroska; 'e^+e^- Physics with the Jade Detector at Petra'; Phys. Rep. 148 p68 (1987).

[80] X.Tata, D.Dicus; Wisconsin preprint MAD/PH/281 (1986).

[81] UA1 Collaboration; 'Experimental Observation of Events with Large Missing Transverse Energy Accompanied by a Jet or a Photon in $p\bar{p}$ Collisions at $\sqrt{s}$ = 540 GeV'; Phys. Lett. 139B p115 (1984).

[82] UA1 Collaboration; 'Events with Large Missing Transverse Energy at the CERN Collider: $W \rightarrow \tau\nu$ Decay and Test of τ-μ-e Universality at $Q^2 = M_W{}^2$'; Phys. Lett. 185B p233 (1987).

[83] A.Honma; 'Results from an Analysis of Missing Transverse Energy Events in the UA1 Experiment at the CERN $p\bar{p}$ Collider'; CERN-EP/86-153 (1986).

[84] UA1 Collaboration; 'Events with Large Missing Transverse Energy at the CERN Collider: Search for the Decays of $W^{\pm}$ onto Heavy Leptons and of Z^0 into Non-Interacting Particles'; Phys. Lett. 185B p241 (1987).

[85] UA1 Collaboration; 'Events with Large Missing Transverse Energy at the CERN Collider: Mass Limits on Supersymmetric Particles'; submitted to Phys. Lett., CERN-EP/87-148 (1987).

[86] UA1 Collaboration; 'Intermediate Vector Boson Properties at the CERN Super Proton Synchrotron Collider'; Europhys. Lett. 1 p327 (1986).

[87] UA2 Collaboration; 'Search for Exotic Processes at the CERN $p\bar{p}$ Collider'; Phys. Lett. 195B p613 (1987).

[88] CELLO Collaboration; DESY report 86-050 (1986).

[89] T.Lavine (MAC); 'Search for Single Photons from Radiative Production of Supersymmetric Particles or Neutrinos'; University of Wisconsin thesis.

[90] S.Whittaker (ASP); 'Single Photon Production in e^+e^- Annihilation'; proceedings of the '23rd International Conference on High Energy Physics' (Berkeley) p602 (1986).

[91] G.Altarelli et al; 'Vector Boson Production at Present and Future Colliders'; Z. Phys. 27C p617 (1985).

[92] E.Commins, P.Bucksbaum; 'Weak Interactions of Leptons and Quarks'; CUP.

[93] N.Cabibbo, L.Maiani, S.Petrarca; 'Signature for Scalar Electrons from Z Production in $p\bar{p}$ Collisions'; Phys. Lett. 132B p195 (1983).

[94] UA1 Collaboration; 'Hadronic Jet Production at the CERN Proton-Antiproton Collider'; Phys. Lett. 132B p214 (1983).

[95] K.Wacker; 'Inclusive Muon Tight Selection from 1984 Data'; UA1 TN/86-26 (1986).

[96] G.Altarelli, G.Parisi; 'Asymptotic Freedom in Parton Language'; Nucl. Phys. 126B p298 (1977).

[97] D.Perkins; 'Introduction to High Energy Physics'; Addison Wesley.

[98] UA1 Collaboration; 'Search for New Heavy Quarks at the CERN Proton-Antiproton Collider'; submitted to Z. Phys., CERN-EP/87-190 (1987).

[99] Argus Collaboration; 'Observation of B^0-$\bar{B}^0$ Mixing'; Phys. Lett. 192B p245 (1987).

[100] B.van Eijk; 'Heavy Flavour Production and Heavy Flavour Mixing at the CERN Proton-Antiproton Collider'; thesis NIKHEF.

[101] J.Jackson; 'Classical Electromagnetism'; Wiley.

[102] H.Eichinger, M.Regler; 'Review of Track Fitting Methods in Counter Experiments'; CERN 81-06 (1981).

[103] D.Charlton et al; 'Monte-Carlo Production using ISAJET 5.23'; UA1 TN/86-97 (1986).

[104] UA1 Collaboration; 'Study of Heavy Flavour Production in Events with a Muon Accompanied by Jet(s) at the CERN Proton-Antiproton Collider'; submitted to Z. Phys., CERN-EP/87-189 (1987).

[105] J.Revol; 'Summary of Theoretical Cross-Sections for Top Quark Production at the CERN Collider'; UA1 TN/86-61 (1986).

[106] D.Charlton, M.Della Negra; 'Generation of Muon and Electron Events from Lepton-Pair Sources with ISAJET 5.25'; UA1 TN/87-64 (1987).